The Pennsylvania State University
The Graduate School
The Eberly College of Science

THEORETICAL STUDY ON TRANSPORT PROPERTIES OF TOPOLOGICAL STATES OF MATTER

A Dissertation in
Physics
by
Hsiu-Chuan Hsu

Submitted in Partial Fulfillment
of the Requirements
for the Degree of

Doctor of Philosophy

December 2015

The dissertation of Hsiu-Chuan Hsu was reviewed and approved* by the following:

Chaoxing Liu
Assistant Professor of Physics
Dissertation Advisor
Chair of Committee

Jainendra Jain
Professor of Physics
Evan Pugh and Erwin Mueller Professor of Physics

Venkatraman Gopalan
Professor of Materials Science and Engineering

Nitin Samarth
Professor of Physics
George A. and Margaret M. Downsbrough Department Head of Physics

*Signatures are on file in the Graduate School.

Abstract

In condensed matter physics, states of matter are usually classified by symmetry. Topological states of matter describe new quantum states of matter that cannot adiabatically connect to conventional states of matter even though they share the same symmetry. Thus, the discovery of topological states of matter has opened a new research era and attracted intensive research interests in recent years. This dissertation is devoted to the theoretical and numerical study of transport properties of topological states of matter, mainly focusing on two topological systems, time reversal invariant topological insulator nano-structures and the quantum anomalous Hall insulators.

The first system studied in this dissertation is time reversal invariant topological insulator, which is an insulating material behaving as an insulator in its interior but with conducting channels on its surface. The conducting surface states of a topological insulator are known as "helical states" due to the spin texture in the momentum space and protected by time reversal symmetry. Helical surface states have been observed in surface sensitive experiments, such as angular-resolved photon emission spectroscopy and scanning tunneling microscopy. However, signatures of topological surface states in transport measurements are complicated by the dominating conduction from bulk channels and strong disorder effect. Therefore, in this dissertation, we numerically study transport in disordered topological insulator nano-structures, e.g. nanowires and nanotubes, which possess a larger surface-to-volume ratio compared to bulk systems. For a topological insulator nanowire, it is found that a gapless mode with linear dispersion, which is refered to as a topological state in the main text, arises when a half-integer magnetic flux quantum is inserted along the nanowire. We find that topological states possess a longer localization length than other non-topological states. Thus, for a long nanowire or nanotube, a larger conductance appears for half-integer magnetic flux, leading to magnetoconductance oscillations with a period equivalent to one magnetic flux quantum. Our numerical simulation of the magnetoconductance oscillations is supported by experimental observations in resistive Bi_2Te_3 nanotubes.

Another system that we study is the quantum anomalous Hall insulator. Similar to the quantum Hall effect, the Hall conductance is quantized and the longitudinal resistance drops to zero in the quantum anomalous Hall effect. However, the quantum anomalous Hall effect is realized in a magnetic system in absence of external magnetic fields and the associated Landau levels. The quantum anomalous Hall effect was first proposed in magnetically doped HgTe quantum wells. However, one obstacle is that this system is paramagnetic, and thus external magnetic fields are required to polarize magnetization and inevitably leads to Landau levels. In this study, we focus on the role of in-plane magnetic fields and find that the quantum anomalous Hall effect can be realized by a purely in-plane magnetic field when there is strain in the system. Symmetry analysis is adopted to provide more theoretical insight of the underlying physics. Without any strain, we explore how to extract the role of magnetization in the standard transport measurement of Hall resistance by rotating magnetic fields. Our results provide a guidance to the recent experiments in Mn doped HgTe quatnum wells with rotating magnetic fields. Besides these studies, we also investigate anisotropic magneto-conductance in magnetically doped $(Bi,Sb)_2Te_3$ films.

The studies in the dissertation are in a close collaboration with transport measurements of experimental groups, including magneto-conductance oscillation observed by Qi's group at Penn State and the study of the Hall conductance in Mn doped HgTe quantum wells with rotating magnetic fields by Molenkamp's group at Wuerzburg University.

Table of Contents

List of Figures viii

List of Symbols xiv

Acknowledgments xvi

Chapter 1
Introduction : fundamentals of topological insulators 1
1.1 History of topological states of matter 1
1.2 Hall conductance 6
1.3 Two-band model and the quantum anomalous Hall effect 7
1.4 Time-reversal symmetry and quantum spin Hall effect 11
1.5 Three-dimensional topological insulator 14
1.6 Magnetic topological insulators 17
1.7 Overview and organization of this dissertation 20

Chapter 2
Theoretical fundamentals for transport in topological insulator nanostructures 21
2.1 Landauer-Büttiker formalism 21
2.2 Recursive Green's function method 25
2.2.1 Derivation of the recursive equations 25
2.2.2 Connection to leads 28
2.3 Analytic solution for an one-dimensional example 32
2.4 Summary of the calculation 34

Chapter 3
Transport in disordered topological insulator nano-structures 35
3.1 Theoretical study of surface states of TI nanowires in the clean limit 36
3.1.1 Dispersion and wave function distribution 38

3.1.2 Magneto-oscillation of conductance 40
3.2 Magneto-oscillation of TI nanotube in the clean limit 42
3.3 Numerical simulation of conductance oscillation in disordered TI nanowire 46
3.3.1 Experimental observation of magnetoconductance in Bi_2Te_3 nanotubes and theoretical interpretation 50
3.4 Conclusions 55

Chapter 4
Quantum anomalous Hall effect in Mn doped HgTe quantum wells **57**
4.1 Model Hamiltonian for $Hg_xMn_{1-x}Te$ quantum wells 58
4.2 The effect of exchange coupling 60
4.3 The interplay between exchange coupling and Zeeman coupling: the reentrant QAH effect 63
4.4 $Hg_xMn_{1-x}Te$ quantum wells with shear strains 68
4.5 Experimental relevance and conclusions 71

Chapter 5
Disordered Quantum anomalous Hall insulators **73**
5.1 Model Hamiltonian 73
5.2 Anisotropic magneto-conductance 75
5.3 conclusion 79

Chapter 6
Summary and outlook **82**

Appendix A
Effective Hamiltonian of the TI surface states **84**
A.1 Derivation of the Effective Hamiltonian of topological surface states 84
A.2 Eigen-solution of the effective Hamiltonian 86
A.3 Time-reversal invariance of the effective Hamiltonian 87

Appendix B
Landau level calculation **88**

Appendix C
Effective Hamiltonian for HgMnTe quantum well **91**

Appendix D
Quantized Hall conductance and extended states **95**

Bibliography **98**

List of Figures

1.1 Schematic view of the geometry for the Hall effect. A specimen is under a perpendicular magnetic field B and a current I is going through along y-direction. The deflection of electron is in x-direction. The accumulation of the charges creates an electric field E_H that cancels the Lorentz force F_+. 2

1.2 The FBZ is separated to two regions S_I and S_{II}. The boundary for S_I is C_I in red, for S_{II} is C_{II} in blue. The inner boundary of S_I is a clockwise circle by definition. The periodic boundary condition requires that $\overline{AB} = \overline{DC}$ and $\overline{BC} = \overline{AD}$. 9

1.3 (a)The d-vector configuration in the FBZ(b) and the corresponding Hall conductance as a function of m_o. $d_{x,y}$ are zero at these particular points. $\odot$ mean d_z is positive, whereas $\otimes$ means d_z is negative. (c)Chiral edge mode of the QAH insulator. 12

1.4 (a)A six-terminal Hall bar of the QSH insulator. There are two counter propagating edge currents with opposite spin polarization. Green denotes the spin-up current, pink denotes the spin-down current. The figure was taken from Bernevig et al. [7]. (b)The longitudinal four-terminal resistance of normal(I) and inverted(II,III,IV) HgTe quantum wells. From Konig el al. [9](c) The image of edge current of a π bar QSH insulator. The figure was taken from Spanton et al. [10] 14

1.5 (a)The schematic figure of a single Dirac cone on the surface of 3D TI. (b)Spin-resolved ARPES shows the helicity at a cross section of the single Dirac cone on the surface of BiSe. The image is taken from Xia et al. [58] 16

1.6 The first Hall measurement of the QAH system in $Cr_{0.15}(Bi_{0.1}Sb_{0.9})_{1.85}Te_3$ film. (a) The Hall resistivity(blue) and the longitudinal resistivity(red). (b)The conductance is obtained from the resistivity through the relation $\sigma_{xy} = \rho_{yx}/(\rho_{yx}^2 + \rho_{xx}^2)$ and $\sigma_{xx} = \rho_{xx}/(\rho_{yx}^2 + \rho_{xx}^2)$ .The figures is taken from Ref [59]. 19

2.1 A schematic plot showing the transmission between leads. 22
2.2 (a) is the conductor connecting to semi-infinite leads. (b) is the conductor adding the lead self-energy. The two are conceptually equivalent. 23
2.3 The schematic slicing scheme of a free-end system. 26
2.4 The schematic slicing scheme with two-terminal leads. The leftmost and rightmost slices are dressed with the self-energy of the lead. . . 32

3.1 The cross section of a nanowire (a) and a nanotube (b) used in the numerical calculation. 36
3.2 Dispersion when (a) there is no magnetic flux (b) a magnetic flux of $\phi_0/2$ is at the center plaquette. 40
3.3 (a)Schematic plot of the hopping when the half magnetic flux quantum is at the center plaquette. (b) and (c)The wave function of the linear modes for flux $\phi_0/2$ at the center plaquette at $k = 0.02, E_f = 0.04$. The linear modes are doubly degenerate, but the wave function distributions behave very differently. One of which is localized on the surface of the nanowire(b), the other is localized at the center(c). 41
3.4 (a) dispersion when flux $= \phi_0/2$ is homogeneously distributed on the cross section. The degeneracy has been lifted due to TR breaking. (b)The wave function distribution at the flux value as (a). k=0.04 and E=0.079. 41
3.5 (a)The oscillations of the surface gaps. (b)Conductance oscillation when E_f lies in the middle of the gap ($E_f = 0$) in the clean limit. . 42
3.6 The magneto-conductance for $E_f = 0.6$ in the clean limit. 42
3.7 The dispersions of a TI nanotube with $N = 17, N_{in} = 6$ at $\phi = 0$(a), $\phi_0/2$(b), $2.255\phi_0$ corresponding to a half flux quantum enclosed by the inner surface state(c), $3\phi_0$(d) 43
3.8 (a)The wave function distribution of the outer edge state with eigenenergy= 0. (b)The wave function distribution of the inner edge state with eigenenergy$\approx$ 0.1. N_{in}^{eff} is depicted in the figure. $N = 20, N_{in} = 12, \phi = \phi_0/2$. 44

3.9 The energy gap of the surface state closes at ϕ/ϕ_0 or ϕ_{in}^{eff}/ϕ_0 is a half-integer a TI nanotube with $N = 50$, $N_{in} = 42$. The top x-axis is the effective flux enclosed by the inner surface state of the nanotube. The blue(green) dashed lines indicate the positions where ${\phi_{in}}^{eff}/\phi_0(\phi/\phi_0)$ are half-integers. 45
3.10 The two-terminal conductance for a TI nanotube with $N = 50$, $N_{in} = 42$ and $L = 40$. (a) The magneto-conductance. (b) The fast Fourier transform of the magneto-conductance. 45
3.11 (a) and (b) Band dispersions for a disorder-free system are shown for $\phi = 0$ and $\phi = \phi_0/2$, respectively. The solid blue line marks the Fermi energy at $E_f = 0.6$, which is used for the calculations in (c) and Fig.3.17. The cross section is taken to be $9a \times 9a$ for all calculations in this section. (c) Length dependence of the conductance is shown for $\phi = 0$ and $\phi = \phi_0/2$ with $W = 2.8$ and $E_f = 0.6$. The solid lines are linear fits, from which we can extract the localization lengths to be $\lambda_{non} = 150a$ for $\phi = 0$ and $\lambda_{top} = 4800a$ for $\phi = \phi_0/2$. 48
3.12 The localization length (in nature log scale) for non-topological states($\phi = 0$) and topological states ($\phi_0/2$ and $7\phi_0/2$). The disorder configuration is 100. L=800a. $E_f = 0.6$ 49
3.13 (a) The phase diagram. The length of the nanowire is 100a. The oscillation and its FFT at the representative points are shown in the lower panels with color coding. (b) AB oscillations and its higher harmonics at $W = 0.2, Ef = 0.8$ (c) AB oscillation at W=0.8, Ef =1.3 (d) AAS oscillation at $W = 2.4, Ef = 0.8$ (e) no oscillation at $W = 3.6, Ef = 1.3$. 51
3.14 The oscillation and the corresponding FFT at various nanowire length: L=100(a), 400(b), 2000(c) with disorder strength $W = 2.8$ and $E_f = 0.6$. 52
3.15 Magneto-conductance oscillations of Device A (background subtracted). Magnetic field is applied parallel to the nanotube axis (current flow direction). The observed period is 3.53 ± 0.20 kOe. This period is consistent with h/e oscillations associated with the outer surface of the nanotube which has diameter of 125 ± 6 nm. . . 53
3.16 Magneto-conductance oscillations on Device B (background subtracted). (a) Conductance oscillations for Device B. The oscillations show an h/e period associated with the outer surface of the nanotube. (b) Conductance oscillations for different field directions, plotted as a function of parallel component of applied field. Evidently, the period depends solely on the parallel component of applied field. . . 53

3.17 (a) The magneto-conductance oscillations as a function of magnetic flux ϕ in the regime II for $W = 2.8, L = 800a$ and $E_f = 0.6$. (b) The magneto-conductance oscillations for a system with variations in the cross sectional area along the length of the nanotube with $\Gamma = 0.4$. The cross section is taken to be $9a \times 9a$ for all calculations. 54
3.18 Comparison between numerical and experimental magnetoconductance without subtracting the background. For numerical calculation, the parameters are $W = 2.8, E_f = 0.6, \Gamma = 0.8$. 56

4.1 The phase diagram obtained from analytical calculation where $g_{ex} = \pm g_{hx}$. 60
4.2 θ is defined as the angle between magnetic field and z-axis. 61
4.3 The phase diagram at 1K for the Hamiltonian without Zeeman coupling. (a) Phase diagram in terms of the magnetic field. (b) Phase diagram in terms of the strength of spin splitting. The y-axis is only g_{2z} because only this term contributes to gap closing. (c)Magnetization of the Mn atoms under the same range of magnetic fields in (a). It saturates at 2.5. (d) The critical angle of magnetic field for metallic lines. The parameters used for are $\tilde{g}_{ex} = -1meV, g_{hx} = 0, \tilde{g}_{ez} = -3meV, \tilde{g}_{hz} = 9meV, A = 0.38eV/nm, B = 0.85eV/nm^2, D = 0.67eV/nm^2, m = 3meV$. 62
4.4 (a)The phase boundary for different values of $\tilde{g}_{ex}$ at T=4.2K. From top to bottom, the values are $-1, -2, -2.5, -3$meV. (b) Critical angle of magnetic field of the phase boundary for different values of $\tilde{g}_{ex}$ at T=4.2K. The values are given in the legend with the unit of meV . The right vertical axis gives the critical angle in degrees. For both (a) and (b), the parameters are $g_{hx} = 0, \tilde{g}_{ez} = -3meV, \tilde{g}_{hz} = 3meV, A = 0.38eV/nm, B = 0.85eV/nm^2, D = 0.67eV/nm^2, m = 4.5meV$. 63
4.5 (a)The effective spin splitting as a function of B_x at a fixed $\mathcal{B}_z$=0.6T. (b) The schematic plot of the Hall conductance in the unit of e^2/h as a function of the $\mathcal{B}_x$ for the indicated $\mathcal{B}_z$=0.6T . (c)The phase diagram at 1K. The diagram is on a logarithmic scale to enhance the contrast. The black lines indicate the phase boundaries of different topologies. (d)The schematic plot of the Hall conductance in the unit of e^2/h as a function of the $\mathcal{B}_x$ for the indicated $\mathcal{B}_z$=0.2T. The parameters used for Fig. (a) and (c) are $\tilde{g}_{ex} = -0.84meV, g_{ex}^{zm} = -0.8meV/T, g_{hx} = 0, \tilde{g}_{ez} = -2.13meV, g_{ez}^{zm} = 1.5meV/T, \tilde{g}_{hz} = 9meV, g_{hz}^{zm} = -0.08meV/T, A = 0.38eV/nm, B = 0.85eV/nm^2, D = 0.67eV/nm^2, m = 3meV$. 65

4.6 The phase diagram at 1K for the Hamiltonian without the exchange coupling. The diagram is on a logarithmic scale to enhance the contrast. The black lines indicate the phase boundaries of different topologies. The parameters used are $\tilde{g}_{ex} = 0meV, g_{ex}^{zm} = -0.8meV/T, g_{hx} = 0, \tilde{g}_{ez} = 0meV, g_{ez}^{zm} = 1.5meV/T, \tilde{g}_{hz} = 0meV, g_{hz}^{zm} = -0.08meV/T, A = 0.38eV/nm, B = 0.85eV/nm^2, D = 0.67eV/nm^2, m = 3meV$. 66

4.7 Landau Level fan chart. The parameters are the same as in Fig.4.5. The blue line indicate the Fermi level at 0.3meV. (a)Landau level fan chart without in-plane magnetization. (b)Landau level at $B_z = 0.2T$ in terms of in-plane magnetic field. (c)Landau level at $B_z = 0.6T$ in terms of in-plane magnetic field. The inset zooms in near Fermi level and shows the reentrant behavior. 68

4.8 In-plane magnetization induced QAH effect in HgMnTe quantum wells. **(a)** The band gap as a function of g_{2z} and ϵ_{xz} with a finite $g_{1x} = 8$ meV. **(b)** The band gap as a function of ϵ_{xz} and ϵ_{yz} with $g_{1x} = 4$ meV, $g_{2x} = 3$ meV. **(c)** Schematic plot of the experimental setup. The angle between the strain vector $\boldsymbol{\epsilon}$ (green arrow) and the magnetization vector $\boldsymbol{m}$ (red arrow) is denoted as φ. The green plane denotes the reflection plane preserved by the strain vector $\boldsymbol{\epsilon}$ while the red plane denotes the reflection plane preserved by the magnetization vector $\boldsymbol{m}$. **(d)** The band gap as a function of g_{1x} and ϵ_{xz} with $g_{2z} = 0$. The other parameters are taken as $M = -3$ meV, $B = 0.85$ eV·nm^2, $D = 0.67$ eV·nm^2, $A = 0.38$ eV·nm, $g_{1(2)y} = g_{1z} = 0$, and $\epsilon_{yz} = 0$. 70

5.1 (a)-(c) are for the open boundary condition, (d)-(f) are for the periodic boundary condition. The corresponding angle from the top to the bottom row is $0, \pi/4, \pi/2$. The parameters used in the calculation are $m = 0.27, A = 1, B = 1, g = 1, M = 0.5$. The number of the transverse sites is 60. 77

5.2 (a)The four-terminal device of QAH system for determination of the chirality. The leads are attached at the black parts. The red block between the leads is infinite potential barrier. It prevents unwanted scattering between two neighboring leads. (b)The chiral mode flips direction when the magnetization rotates from above to below the plane. 78

5.3 Two-terminal conductance in clean limit. (a)-(c) are for OBC. (d)-(f) are for PBC. The Fermi energy from the top to bottom row is $0, 0.2, 0.3$. The number of the longitudinal/transverse sites is 100/60. 80

5.4 Two-terminal conductance in the presence of disorder. (a)-(c)are for OBC. (d)-(f) are for PBC. The Fermi energy from the top to bottom row is $0, 0.2, 0.3$. The number of the longitudinal/transverse sites is 100/60. The number of disorder configuration is 100. 81

D.1 Total density of states, extended density of states and Hall conductance for $W = 1$(a) and $W = 2.5$(b). $p/q = 1/3$ for systems of size 9×9. The disorder configuration is 400. The number of grid for boundary condition is 24×24. 97

List of Symbols

QH	Quantum Hall
FQH	Fractional quantum Hall
QAH	Quantum anomalous Hall
QSH	Quantum spin Hall
TR	Time-reversal
TI	Topological insulator
TCI	Topological crystalline insulator
1D	One-dimensions (or one-dimensional)
2D	Two-dimensions (or two-dimensional)
3D	Three-dimensions (or three-dimensional)
ARPES	angle-resolved photoemission spectroscopy
STM	scanning transmission microscopy
$\hbar$	Planck's constant divided by 2π
e	The absolute value of electron charge
σ_{ij}	The conductivity matrix
ϕ_0	Magnetic flux quantum, which equals to h/e. h is Planck's constant.
TB	Tight-binding

AB Aharonov-Bohm

AAS Altshuler-Aronov-Spivak

Acknowledgments

The completion of this dissertation would not happen without the help and support from many people. First, I would like to thank my adviser, Dr. Chaoxing Liu, for his patient guidance leading me to the field of topological insulators. He is responsive to emails and always available for discussions when I have questions. I am also indebted to Dr. Jainendra Jain for his insightful advice and mentorship.

I have benefited from many fruitful conversations with my friends and colleagues at Penn State which I am very grateful for. Ajit Balram has been a source of great help in numerical methods. Alex Archer, Xihao Deng, Sangzi Liang and Yinghai Wu have patiently helped me with programming when I was a beginner. I am thankful to Piali Aditya, Brian Cooper, Christian Cruz, Ashley DaSilva, Krisin Dreyer, Feifei Huang, Aruna Kesavan, Xin Liu, Yu Pan, Sumithra Surendralal, Qingze Wang, Ruixing Zhang for their friendship and advice. Thank you all for making my journey during the Ph.D. years so colorful.

My parents have been supportive and encouraging thoughout the years in graduate school. It is a pity that my father passed away before the completion of this dissertation. How I wish he could share the joy with me at this moment. I am grateful for his support in my decision to pursue a Ph.D and I am sure he would be proud of my achievement. Finally, I would like to thank my fiancee for understanding and loving me. It is exciting to begin a new chapter in our lives together.

Dedication

To my father

Chapter 1
Introduction : fundamentals of topological insulators

1.1 History of topological states of matter

The story begins with a well-known phenomenon discussed widely in textbooks of fundamental physics, the Hall effect. This phenomenon was discovered by and named after Edwin H. Hall in 1879 [1]. It describes the build-up of a transverse voltage when a longitudinal current is driven across a conductor in a perpendicular magnetic field as depicted in Fig.1.1. The transverse voltage, also called Hall voltage, is produced by the cyclotron motion and the subsequent deflection of moving electrons due to the Lorentz force. The Hall effect has an important application in solid-state transport measurements: it is a basic tool to characterize carrier type and carrier concentration of the material by the sign and the magnitude of the Hall voltage, respectively.

Soon after the discovery of the (classical) Hall effect, Hall found a significant enhancement of the Hall voltage in a current-carrying ferromagnetic material, which is dubbed as the anomalous Hall effect [2]. The physical origin of the anomalous Hall effect has been studied extensively in the past 50 years [3]. Although the general mechanism is complicated due to multiple contributions, the key ingredients for the anomalous Hall effect are magnetism, spin-orbit coupling and disorder effects. The recent development comes from the theoretical understanding of topological origin of the Hall conductance , which is related to Berry curvature of electronic bands [4]. Non-zero Berry curvature is found in electronic bands with magnetism

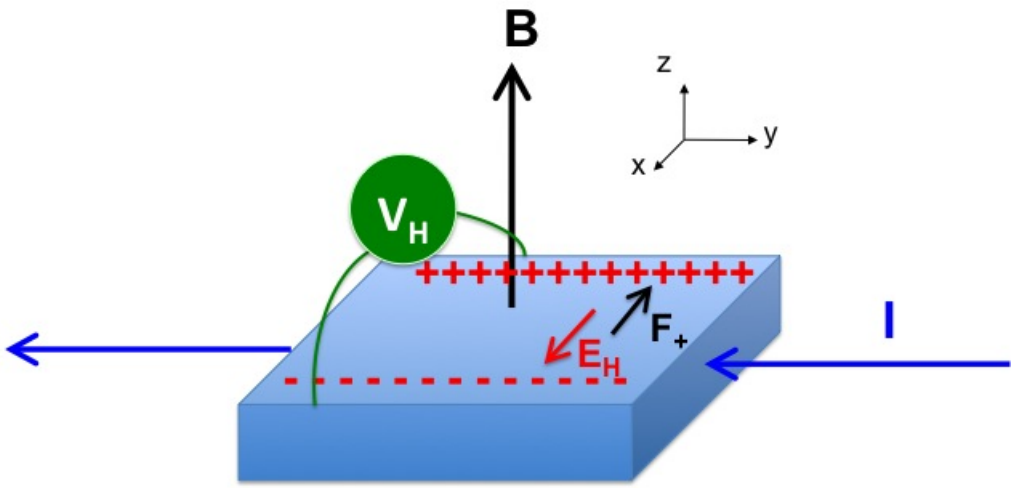

Figure 1.1. Schematic view of the geometry for the Hall effect. A specimen is under a perpendicular magnetic field B and a current I is going through along y-direction. The deflection of electron is in x-direction. The accumulation of the charges creates an electric field E_H that cancels the Lorentz force F_+.

and spin-orbit coupling, contributing to the non-zero anomalous Hall conductance. For this mechanism, the Hall conductance is a consequence of topology of band structures, rather than external scattering mechanism or electromagnetic interaction. Thus, the anomalous Hall effect induced by this mechanism is called the intrinsic anomalous Hall effect.

One hundred years later, von Klitzing et al. [5] discovered that for a two-dimensional electron gas (2DEG) under strong perpendicular magnetic field, the Hall conductance is quantized at $\sigma_H = n\frac{e^2}{h}$, where σ_H is the Hall conductance, e and h are electron charge and Planck constant and n is any integer. This is called the integer quantum Hall (IQH) effect. The underlying reason for the Hall conductance quantization is because 2DEG forms Landau levels under strong perpendicular magnetic field [6]. All bulk states are localized and chiral edge states, which only propagate along one direction, appear at the boundary of the sample, contributing to the quantized Hall conductance [8, 11]. The quantization is robust against disorder and sample geometry as long as the gap between subsequent Landau levels is maintained. The exact quantization originates from topological property of electronic wave functions, as first shown by Thouless, Kohmoto, Nightingale and den Nijs (TKNN) [12]. They derived a formula, known as the TKNN formula,

to show that the integer value of the Hall conductance comes from a topological integral over the whole momentum space and is characterized by a topological invariant, called TKNN number, or mathematically known as the Chern number.

Furthermore, it was discovered that the Hall conductance can not only be a quantized integer in unit of e^2/h, but also be a rational fractions of e^2/h [13]. This phenomenon is called fractional quantum Hall (FQH) effect. Unlike IQH effect, FQH effect occurs when Fermi level lies within a Landau level [6].The key ingredient is the strong interaction that opens up a gap within a Landau level, thus giving rise to a fraction of the Hall conductance when a fraction of the Landau level is occupied. The theoretical description of the FQH states requires many-body origin. Laughlin proposed a many-body wave function that explains the $\nu = 1/3$ state [14]. For higher-order FQHE, which filling factor is $\nu = 2p/(2p \pm 1)$ with $p \in$integer, Jain proposed the picture of composite fermions, which are magnetic flux - attached electrons [15]. The physical picture is clear that the FQH effect of electrons is actually the IQH effect of composite fermions.

The IQH effect and FQH effect provide us the first two examples of topological states of matter. Conventionally, the states of matters are distinguished by the underlying symmetry of the system, as described in the theory of the second order phase transition by Landau [16]. For example, a crystalline solid is different from a gas because it breaks translational symmetry. However, topological states of matter cannot be adiabatically connected to conventional states of matter, even though they share the same symmetry as the corresponding conventional states of matter. Thus, topological states do not fall into the paradigm of Landau theory. Instead, to classify topological states of matters, one needs to use another mathematical tool, namely topology, to study topological property of electronic bands.The discovery of the IQH effect and FQH effect has opened a new era in the research of condensed matter physics. However, for quite a long period, the study of topological states of matter had been only limited to the IQH effect and FQH effect of two-dimensional(2D) electron gases, both of which require external magnetic fields. It was unclear if topological states of matter exist in other systems, in particular without external magnetic fields.

A breakthrough of this field occurred around 2005 and a new topological state, dubbed time reversal (TR) invariant topological insulators (TIs), was theoretically predicted [7, 17]. TR invariant TI is a new class of materials that insulates in the

interior of the bulk and possesses gapless modes at the edge/surface. Unlike IQH and FQH effects, magnetic field is not required for the existence of TR invariant TIs. Instead, the physical origin of TIs is strong spin-orbit coupling, which is TR symmetric, of the system. In contrast to chiral edge modes of the IQH effect, gapless modes of TR invariant TIs reveal helical nature, and thus are dubbed "helical modes". The helical modes are protected by bulk topology and TR symmetry, and thus immune to back-scattering caused by TR symmetric disorder.

The first theoretical predictions of TI were quantum spin Hall(QSH) insulators, also known as two dimensional (2D) TIs, proposed by Bernevig et al in HgTe/CdTe quantum wells [7] and Kane and Mele in graphene [17]. A QSH system can be viewed as two subsystems with opposite Hall conductances. Each copy of the system is for one spin species and thus two subsystems are related to each other by TR symmetry. The total Hall conductance is cancelled between two spin subsystems, but the spin Hall conductance, defined as the difference of the Hall conductance between two spin species, is nonzero. Soon after the theoretical prediction, the QSH effect was observed in HgTe/CdTe quantum wells [18] and later in InAs/GaSb quantum wells [19]. The idea of TIs was also generalized to three dimensions(3D). The surface of a 3D TIs possesses odd number of Dirac cones with a salient feature of spin-momentum locking. 3D TIs were experimentally observed in different classes of materials [20–25, 58].

Another striking development in this field is the experimental realization of the so-called quantum anomalous Hall effect [59], which is the appearance of the quantized Hall conductance without magnetic field, in magnetically doped topological insulators. The essential difference between the QAH effect and the QH effect is that at a zero magnetic field, there are no Landau levels and all electronic properties can be well described by electronic band theory. In 1988, Haldane [26] proposed the first theoretical model to realize non-zero Hall conductance at a zero total magnetic flux in a 2D honeycomb lattice. Although the net magnetic flux is zero in one unit cell, magnetic flux is still required for this model to break TR symmetry. More importantly, it was unclear how to realize this model in realistic materials at that time. Therefore, the Haldane model was overlooked for more than two decades until recent developments in photonic [27] and cold atom systems [28]. The tunability and accessibility of these systems provide a new direction for the realization of the Haldane model.

The next important step towards understanding the QAH effect was the theoretical proposal of two-band model by Qi et al. [29], which also realized the quantized Hall conductance in certain parameter regimes. Compared to the Haldane model, the importance of this model lies in the fact that no magnetic flux is required for this model and all the key ingredients for the QAH effect in this model, such as strong SOC and exchange coupling between magnetization and electrons, exist in realistic materials. Thus, it is more close to experimental realization. The first realistic material system for the QAH effect was predicted by Liu [30] in Mn doped HgTe/CdTe quantum wells. Although the experimental realization of this proposal has still not been achieved, mainly due to the fact that this system is paramagnetic not ferromagnetic, this work reveals the relationship between the QSH effect and the QAH effect and sheds light on the search for other QAH systems in magnetically doped TIs. Later, Cr doped $(BiSb)_2Te_3$ was predicted to be ferromagnetic [31] and shown to possess quantized Hall resistance experimentally [59].

The discovery of TIs and the QAH effect has paved the way to a new research paradigm for the study of different types of topological states of matter in a broader family of materials since no magnetic field is required. In particular, the research on TIs reveals the role of symmetry in the classification of topological states of matter. This idea was soon generalized to other systems. Intensive research activity is focused on the search for new topological systems and new topological phases, including topological superconductors [32–34], topological Mott insulators [35–37], fractional Chern insulator [38–41], topological crystalline insulators(TCIs) [42–45] and topological photonics [46–48]. In the superconducting gap of a topological superconductor, zero-energy states exist at the boundary of a sample, which is similar to the Majorana fermions in high energy physics and thus dubbed "Majorana zero mode" [32–34]. Topological Mott insulators refer to topological insulating phases induced by the electron-electron interactions, which possess edge/surface modes in the mobility gap of Mott insulators [35–37]. Fractional Chern insulator is shown to have fractional values of the Hall conductance without Landau levels, and arises in the presence of strong correlation when topological bands are partially filled, similar to FQH effect [38–41]. Another symmetry-protected states of matter is TCI in which surface states are protected by crystal symmetries [42,43]. TCI were experimentally realized in SnTe and $Pb_{1-x}Sn_xSe$, which are both protected by mirror symmetry of the crystal. Besides topological phases in solid-state systems, nontrivial

topology has been measured in cold atom systems as well [28, 49]. Moreover, TI and QAH effect have their photonic counterpart. For example, at the edge of a topological photonic crystal with non-zero Chern number, light can travel without back-reflection even in the presence of disorder [46–48].

This thesis is devoted to the study of transport behaviors of topological states of matter, focusing on topological insulators and the quantum anomalous Hall insulators. Below, we will first introduce the necessary theoretical background of topological states of matter.

1.2 Hall conductance

In this section, we will first introduce the topological invariant, the Chern number, which characterizes the quantized Hall conductance in the QH and QAH systems. The formula for Hall conductance and topological aspects of wave functions are presented in this section. We consider linear response of the Hall conductivity (Kubo formula) [12]

$$\sigma_{\alpha\beta} = \frac{ie^2}{\hbar}\sum_{n\neq m}\frac{(\partial_\alpha H)_{nm}(\partial_\beta H)_{mn} - (\alpha \leftrightarrow \beta)}{(E_n - E_m)^2}, \tag{1.1}$$

where $(\partial_\alpha H)_{nm} = \langle u_n|\frac{\partial H}{\partial k_\alpha}|u_m\rangle$, $|u_n(m)\rangle$ is Bloch wave function of electronic bands, $E_n(m)$ is the corresponding eigenenergy, m denotes the occupied bands and n denotes the unoccupied bands. Using the identities $(\partial_\alpha H)_{nm} = (E_n - E_m)\langle\partial_\alpha u_n|u_m\rangle$ and $\sum_{n\neq m}(|u_n\rangle\langle u_n| + |u_m\rangle\langle u_m|) = 1$. We can rewrite the Kubo formula into another form

$$\begin{aligned}
\sigma_{\alpha\beta} &= \frac{ie^2}{\hbar}\sum_m(\langle\frac{\partial u_m}{\partial k_\alpha}|\frac{\partial u_m}{\partial k_\beta}\rangle - (\alpha \leftrightarrow \beta)) &(1.2)\\
&= \frac{e^2}{\hbar}\sum_m\int\frac{d^2k}{(2\pi)^2}\mathcal{F}_{\alpha\beta} &(1.3)\\
\text{,where } \mathcal{F}_{\alpha\beta} &= \partial_\alpha A_\beta - \partial_\beta A_\alpha\\
\text{and } \vec{A} &= i\langle u_m|\partial_{\vec{k}}|u_m\rangle.
\end{aligned}$$

$\vec{A}$ is called the Berry connection and $\mathcal{F}_{\alpha\beta}$ is the Berry curvature. Intuitively, $\vec{A}$ and $\mathcal{F}_{\alpha\beta}$ can be viewed as an effective vector potential and effective magnetic field in the momentum space. Thouless, Kohmoto, Nightingale and den Nijs (TKNN) [12]

first derived this formula for electrons of a 2D system under magnetic fields and periodic potentials, which can be applied to any 2D band systems. The significance of this formula becomes more clear in the study of the intrinsic anomalous Hall effect during the 1990s and 2000s. The topological property of this formula is illustrated as below. If the phase of the wave function u_m is well-defined in the first Brillouin zone (FBZ), Stoke's theorem can be applied to change the surface integral $\int d^2k \nabla \times \vec{A}$ into a line integral $\oint d\vec{k} \cdot \vec{A}$. Because of the periodic boundary condition of the FBZ: $\overline{AB} = \overline{DC}$ and $\overline{BC} = \overline{AD}$ in Fig.1.2, the FBZ can be identified as a torus, which does not have a boundary. Therefore, the integral vanishes and gives rise to a zero Hall conductance. This discussion immediately tells us that the non-vanishing Hall conductance appears only when the phase of the wave function can not be uniquely defined for all the momenta in the whole FBZ. To show this more explicitly, we will discuss a two-band model in the next section.

1.3 Two-band model and the quantum anomalous Hall effect

In this section, we will discuss a two-band model first introduced by Qi et al. [29], which gives rise to a quantized Hall conductance without external magnetic fields. Following the discussion by TKNN [12], we will show that the quantized Hall conductance is a consequence of the appearance of singularity of occupied eigenstates in the FBZ, where the phase of the wave function is not well-defined. Moreover, we will also demonstrate geometrical meaning of the Hall conductance using the concept of d-vector and winding number.

The explicit form of H_{QAH} in a square lattice model is

$$H_{QAH} = \begin{pmatrix} m & A(\sin k_x - i \sin k_y) \\ A(\sin k_x + i \sin k_y) & -m \end{pmatrix} \tag{1.4}$$

, where $m = m_o + B(2 - \cos k_x - \cos k_y)$ and lattice constant of square lattice is taken to be 1. The Hamiltonian can be written in a more compact form

$$H_{QAH} = A \sin k_x \sigma_x + A \sin k_y \sigma_y + m\sigma_z \tag{1.5}$$

$$= \vec{d} \cdot \vec{\sigma} \tag{1.6}$$

,where $\vec{d} = (A \sin k_x, A \sin k_y, m)$ and σ are the Pauli matrices. The eigenvalues of the Hamiltonian are $\pm d$, where $d = \sqrt{d_x^2 + d_y^2 + d_z^2}$. The corresponding eigenvectors are

$$|u_{\pm}^I\rangle = \frac{1}{\sqrt{2d(d \mp d_z)}} \begin{pmatrix} d_- \\ \pm d - d_z \end{pmatrix}. \tag{1.7}$$

The phase of the above eigenstate is ill-defined when the energy gap, or equivalently d, vanishes. We find that the gap closes at the momenta that satisfy the following conditions:

$$\begin{aligned} m_o &= 0 : (k_x, k_y) = (0, 0) \\ m_o &= -2B : (k_x, k_y) = (0, \pi), (\pi, 0) \\ m_o &= -4B : (k_x, k_y) = (\pi, \pi) \end{aligned} \tag{1.8}$$

We choose $B > 0, m_o < 0$. Take the first condition as an example, near $\vec{k} = (0, 0)$, $d \approx |m_o| \sqrt{1 + \frac{(A^2 + m_o B^2)k^2}{m_o^2}}$, $2d(d + d_z) \approx A^2 k^2$ and u_- becomes

$$|u_-^I\rangle \approx \begin{pmatrix} e^{-i\theta} \\ 0 \end{pmatrix},$$

where $\theta = \tan^{-1} \frac{k_y}{k_x}$. The phase θ, as well as the corresponding $\vec{A}$ field, are not well-defined at $\vec{k} = (0, 0)$. To get a description for $\vec{A}$ field at $\vec{k} = (0, 0)$, one can do a gauge transformation and obtain the eigenstates

$$|u_{\pm}^{II}\rangle = \frac{1}{\sqrt{2d(d \pm d_z)}} \begin{pmatrix} \pm d + d_z \\ d_+ \end{pmatrix}. \tag{1.9}$$

The relation between u^I and u^{II} is $u^I = -e^{i\theta} u^{II}$. At this gauge choice, u_-^{II} near $(0, 0)$ is $\approx (-1\, 0)^T$ and is well-defined. To calculate the Hall conductance, we will use Eq.(1.3). The FBZ is separated into two regions, in region I(II), the phase of $u_-^{I(II)}$ is well defined everywhere. Thus, one can use the Stokes theorem in the regime $I(II)$ for $u_-^{I(II)}$ and the Berry connection $\vec{A}^I$ and $\vec{A}^{II}$ of the wave functions are related by $\vec{A}^{II} = \vec{A}^I + \frac{\partial \theta}{\partial \vec{k}}$. The line integral includes two parts (Fig.1.2)

$$\sigma_{xy} = \frac{e^2}{\hbar}\int_{FBZ}\frac{d^2k}{(2\pi)^2}\nabla\times\vec{A} \tag{1.10}$$

$$= \frac{e^2}{\hbar}\int_{S_I}\frac{d^2k}{(2\pi)^2}\nabla\times\vec{A}^I + \frac{e^2}{h}\int_{S_{II}}\frac{d^2k}{(2\pi)^2}\nabla\times\vec{A}^{II} \tag{1.11}$$

$$= \frac{e^2}{\hbar}\frac{1}{(2\pi)^2}\left[\left(\oint_{C_I} d\vec{k}\cdot\vec{A}^I - \oint_{C_{II}} d\vec{k}\cdot\vec{A}^I\right) + \oint_{C_{II}} d\vec{k}\cdot\vec{A}^{II}\right] \tag{1.12}$$

Because of the periodic boundary condition $\overline{AB} = \overline{DC}$ and $\overline{BC} = \overline{AD}$ in Fig.1.2, the first line integral vanishes, i.e. $\oint_{C_I} d\vec{k}\cdot\vec{A}^I = 0$

$$\sigma_{xy} = \frac{e^2}{\hbar}\frac{1}{(2\pi)^2}\oint_{C_{II}} dk(\vec{A}^{II} - \vec{A}^I) \tag{1.13}$$

$$= \frac{e^2}{\hbar}\frac{1}{(2\pi)^2}\oint dk\cdot\frac{\partial\theta}{\partial k} \tag{1.14}$$

$$= \frac{e^2}{h} \tag{1.15}$$

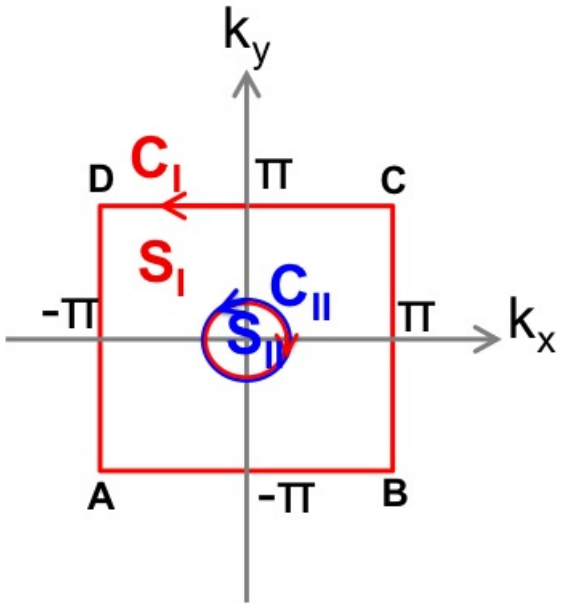

Figure 1.2. The FBZ is separated to two regions S_I and S_{II}. The boundary for S_I is C_I in red, for S_{II} is C_{II} in blue. The inner boundary of S_I is a clockwise circle by definition. The periodic boundary condition requires that $\overline{AB} = \overline{DC}$ and $\overline{BC} = \overline{AD}$.

From this example, one can clearly see how singularity in gauge potential leads to the quantization of Hall conductance.

For a two-band model, there is another simple way to show the geometric meaning of the Hall conductance Eq.(1.3). The Hall conductance for a 2×2 Hamiltonian can be written into a linear combination of Pauli matrices $H_{2\times 2} = \vec{d} \cdot \vec{\sigma}$. The coefficients are called a d-vector. It was shown that the Hall conductance can be written in the forms of the vector $\hat{\mathbf{d}}$ [50]

$$\sigma_{xy} = \frac{e^2}{2\hbar} \int \frac{d^2k}{(2\pi)^2} \hat{\mathbf{d}} \cdot \frac{\partial \hat{\mathbf{d}}}{\partial k_x} \times \frac{\partial \hat{\mathbf{d}}}{\partial k_y} \tag{1.16}$$

, where $\hat{\mathbf{d}} = \vec{d}/d$. It gives geometrical meaning of the Hall conductance for a 2×2 Hamiltonian [29]. Consider the mapping for $\hat{\mathbf{d}}$ from FBZ to a unit sphere: $T^2 \to S^2$, the integration $\int d^2k \hat{\mathbf{d}} \cdot \frac{\partial \hat{\mathbf{d}}}{\partial k_x} \times \frac{\partial \hat{\mathbf{d}}}{\partial k_y}$ gives the total area of S^2 that $\hat{\mathbf{d}}$ covers. The integral equals to $4\pi n$, where n is an integer. n is also called winding number interpreted as the number of times the d-vecor wraps around the unit sphere. Therefore, for a 2×2 Hamiltonian, the Hall conductance can be determined by the configuration of the d-vector in FBZ.

The parameter m_o changes the d-vector configuration in FBZ as well as changes the Hall conductance. When $m_o \to \pm\infty$, the d-vector does not wrap in the FBZ and $\sigma_{xy} = 0$ according to Eq.(1.16). Numerical methods can be applied to the direct calculation of the Hall conductance in the full FBZ. Here we adopt an alternative way to determine Hall conductance using analytic solution and the geometric meaning of d-vector. The idea is to calculate the change of Hall conductance across the transition point analytically based on low-energy effective Hamiltonian. We take the transition at $m_o \approx 0$ as an example. The change in Hall conductance is independent of the large-momentum contribution because in that regime m_o is negligible and $\hat{d}$ configuration does not change [51]. The integral in Eq.(1.2) is cut off at a finite momentum. When $m_o \approx 0$, the expansion near $(0, 0)$ gives $H(0, 0) = Ak_x\sigma_x + Ak_y\sigma_y + m_o\sigma_z$ and the change of Hall conductance is

$$\begin{aligned} \Delta\sigma_{xy} &= \frac{-e^2}{\hbar} \int_0^\Lambda \frac{kdk}{4\pi} \frac{A^2 m_o}{2(A^2k^2 + m_o^2)^{3/2}} \\ &= \frac{-e^2}{2h} \frac{m_o}{|m_o|} \end{aligned} \tag{1.17}$$

This equation only gives the change in Hall conductance near the points where d_z flips signs, i.e. $\sigma_{xy}(m_o > 0) - \sigma_{xy}(m_o < 0) = -\frac{e^2}{h}$. The Hamiltonian for $m_o > 0$ adiabatically connects to the Hamiltonian for $m_o \to \infty$, thus $\sigma_{xy}(m_o > 0) = 0$. From the change in the Hall conductance, we obtain $\sigma_{xy}(m_o < 0) = \frac{e^2}{h}$. Similarly, when $m_o \approx -2B$, d_z flips sign at $(0, \pm\pi)$, $(\pm\pi, 0)$. Take $m_o + 2B = \delta \to 0$. The expansion near these points are $H(0, \pm\pi) = Ak_x\sigma_x - Ak_y\sigma_y + \delta\sigma_z$ and $H(\pm\pi, 0) = -Ak_x\sigma_x + Ak_y\sigma_y + \delta\sigma_z$. The change in Hall conductance is $\sigma_{xy}(\delta \to 0^+) - \sigma_{xy}(\delta \to 0^-) = 2\frac{e^2}{h}$, in which $\sigma_{xy}(\delta \to 0^+) = \frac{e^2}{h}$ because it is adiabatically connected to the regime $-2B < m_o < 0$. Therefore, we obtain $\sigma_{xy}(\delta \to 0^-) = \frac{-e^2}{h}$. When $m_o < -4B$, the d-vector does not change sign in FBZ, the Hall conductance is zero. The d-vector configuration and the corresponding Hall conductance as a function of m_o are summarized in Fig.1.3.

Similar to the QH effect, non-zero bulk Hall conductance also suggests the existence of chiral edge modes for a finite sample with a boundary. This type of chiral edge modes can also be directly shown by solving the above two-band model in a slab geometry with an edge. It is shown that the edge state is spin polarized and exponentially localized at the edge [34]. A schematic plot of chiral edge modes is depicted in Fig.1.3(c). From this two-band model, one can see that the quantized Hall conductance can indeed be realized in a band model without any Landau level.

1.4 Time-reversal symmetry and quantum spin Hall effect

In the above, we have shown how topological properties of electronic bands can lead to the QAH effect with quantized Hall conductance. In this section, we will illustrate the role of symmetry in the classification of topological phases. This was first unveiled by theoretical prediction and experimental realization of the QSH effect [7, 17, 18, 52, 53](also known as 2D TR invariant TIs), for which topologically non-trivial electronic band structures are protected by TR symmetry. To see this, we consider a simple four-band model, which is two copies of the two-band QAH model Eq.(1.4). A variation of this model was first discussed in the context of HgTe/CdTe quantum wells by Bernevig, Hughes and Zhang, and thus also dubbed the BHZ model [7]. The Hamiltonian is given by

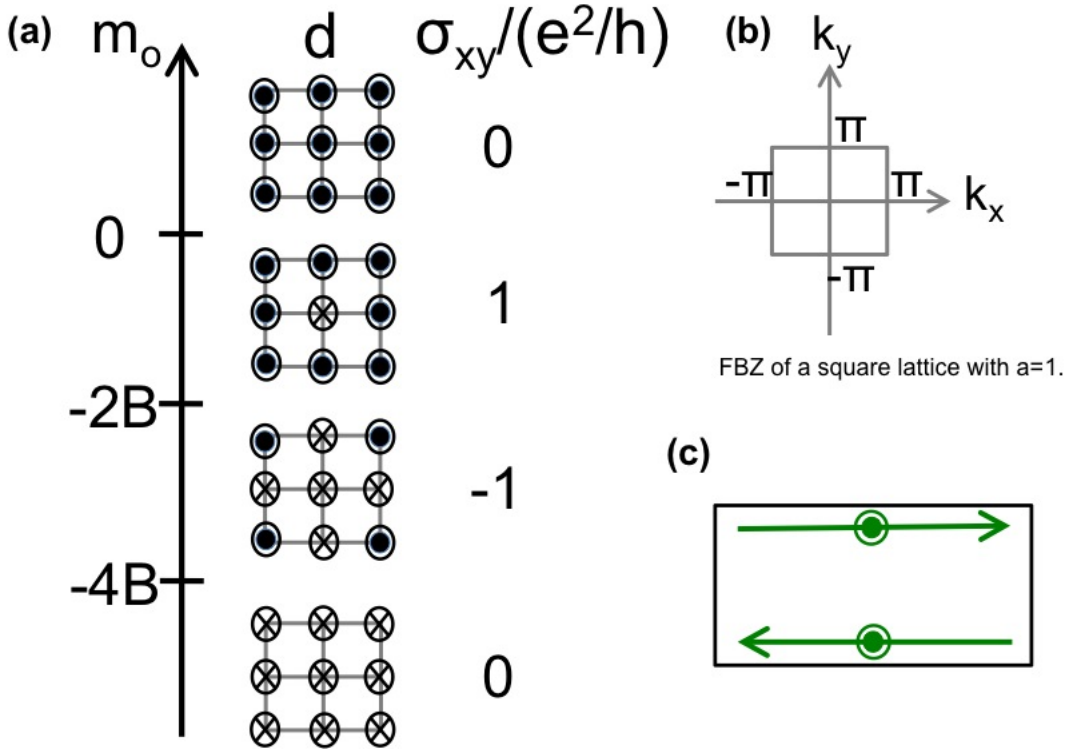

Figure 1.3. (a)The d-vector configuration in the FBZ(b) and the corresponding Hall conductance as a function of m_o. $d_{x,y}$ are zero at these particular points. $\odot$ mean d_z is positive, whereas $\otimes$ means d_z is negative. (c)Chiral edge mode of the QAH insulator.

$$H_{QSH} = \begin{pmatrix} H_{QAH}(k) & 0 \\ 0 & H^*_{QAH}(-k) \end{pmatrix}. \tag{1.18}$$

The Hamiltonian contains two QAH Hamiltonians, which are related by TR symmetry. Each block Hamiltonian carries Hall conductance of $\pm e^2/h$, respectively. Consequently, the overall Hall conductance is zero, while the spin Hall conductance, which is the difference between two conductances for opposite spins, is quantized. This system gives us a simple model for a QSH insulator. To see the existence of the edge states, the Hamiltonian is solved for a slab geometry. Each block Hamiltonian gives rise to one chiral edge state with opposite propagating directions and spin polarizations as depicted in Fig.1.4(a). This type of edge states are dubbed "helical edge states" [34]. Remarkably, there is no backscattering between the two counter

propagating edge states. In other words, the edge states are ballistic. This property is protected by TR symmetry of the Hamiltonian. Any disorder type which obeys TR symmetry does not ruin ballistic transmission.

The experimental realizations of the QSH states are in HgTe quantum wells [18], and later in InAs/GaSb quantum wells [19]. Both materials have inverted band sequence. In most semiconductors, the valence band is composed of p-orbitals and the conduction band is s-orbitals. When there is strong spin-orbit coupling, like in bulk HgTe, the band inversion happens at low energy, namely, the p-orbital bands are pushed above the s-orbital band. This unusual sequence of energy bands is called inverted band structure. For the HgTe/CdTe quantum wells, band gap and energy dispersion depend on the well thickness. When the thickness is large, the band remains in the inverted regime. In contrast, when the HgTe layer becomes thinner, energy bands are shifted and the band sequence becomes normal. The QSH effect is predicted to exist in the HgTe/CdTe quantum wells when the well thickness is above some critical value and the corresponding band structure is in the inverted regime. This theoretical prediction was soon confirmed by the transport measurement by König et al [18]. A similar situation also occurs in the InAs/GaSb quantum wells, in which the valence band top of the GaSb is higher than the conduction band bottom of the InAs due to large band off-set between these two materials. The existence of helical edge modes in this system was demonstrated by Knez et al [19].

The confirmation of helical edge modes was mainly through transport experiments. In ballistic regime, each one-dimensional channel contributes a conductance of e^2/h. For helical modes in a QSH insulator, conductance of $2e^2/h$ is expected. In the measurement on a Hall bar of HgTe quantum wells, the longitudinal four-terminal conductance was shown to be quantized at $2e^2/h$ in the inverted regime, while vanishing in the normal regime [18]. In addition, nonlocal measurements help to confirm transport current flowing through the edge in QSH insulators [53]. The result agrees with the Landauer-büttiker formula for two counter-propagating edge channels. In addition to its transport signature, the edge current is 'seen' with an imaging technique by measuring magnetic flux produced by edge currents [54] as shown in Fig.1.4(b). The current image directly confirms spatial distribution of conducing channels in QSH insulators.

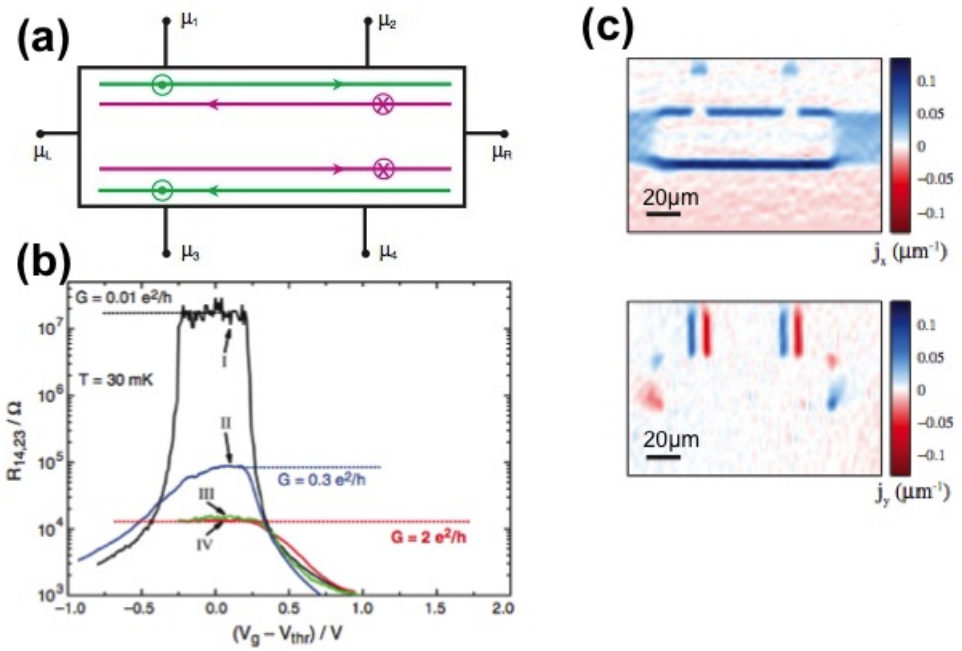

Figure 1.4. (a)A six-terminal Hall bar of the QSH insulator. There are two counter propagating edge currents with opposite spin polarization. Green denotes the spin-up current, pink denotes the spin-down current. The figure was taken from Bernevig et al. [7]. (b)The longitudinal four-terminal resistance of normal(I) and inverted(II,III,IV) HgTe quantum wells. From Konig el al. [9](c) The image of edge current of a π bar QSH insulator. The figure was taken from Spanton et al. [10]

1.5 Three-dimensional topological insulator

Different from the QH or QAH effect, which does not have three-dimensional (3D) counterpart, the 2D QSH effect can be generalized to 3D, which is called the 3D TIs [55, 56]. For 3D TIs, nontrivial topology of the bulk Hamiltonian ensures helical surface states on the 2D surface. In this section, the model Hamiltonian, properties of surface states and experimental realization of 3D TIs are presented. The model Hamiltonian for a 3D TI can be regarded as a generalization of 2D QSH

Hamiltonian(E.q.(1.18)) to the third dimension and is given by [57]

$$H = \epsilon_o I + \begin{pmatrix} M(k) & A_1(k_z) & 0 & A_2 k_- \\ A_1 k_z & -M(k) & A_2 k_- & 0 \\ 0 & A_2 k_+ & M(k) & -A_1 k_z \\ A_2 k_+ & 0 & -A_1 k_z & -M(k) \end{pmatrix}, \tag{1.19}$$

where $\epsilon_o = C + D_1 k_z^2 + D_2(k_x^2 + k_y^2)$, $M(k) = m_o - B_1 k_z^2 - B_2(k_x^2 + k_y^2)$, $C, D, A_1, A_2, B_1, B_2, m_o$ are material-dependent parameters.

This Hamiltonian, Eq.(1.19), is an effective Hamiltonian for the Bi_2Se_3 family, which are the most studied materials because the bulk insulating gap is larger than thermal energy at room temperature [57, 58]. For Bi_2Se_3, the basis for the effective Hamiltonian is $|P1_z^+ \uparrow\rangle, |P2_z^- \uparrow\rangle, |P1_z^+ \downarrow\rangle, |P2_z^- \downarrow\rangle$, where $\uparrow, \downarrow$ denotes spin eigenstates and $\pm$ are for opposite parities. By comparing this model to the Hamiltonian (E.q.(1.18)) for the 2D QSH effect, we can see that the two Hamiltonians share two similar features: TR symmetry and band inversion. The Hamiltonian satisfies $TH(k)T^{-1} = H(-k)$ where the TR operator is given by $T = i\sigma_y K$, where σ_y is a Pauli matrix and K is the complex conjugation operator. Similar to the Hamiltonian (E.q.(1.18)), the band inversion occurs in a certain parameter regime for this Hamiltonian where m_o and $B_{1,2}$ possess the same sign. Band ordering is inverted at $k = 0$, where m_o term is dominant, compared with that at large k, where $B_{1,2}$ terms dominate. The band inversion in the momentum space characterizes the topology of this effective Hamiltonian.

In order to study surface states, one needs to solve the Hamiltonian (Eq.(1.19)) with open boundary condition, similar to the case of 2D systems. For a surface perpendicular to the z-axis, k_x, k_y are still good quantum numbers, but k_z is replaced with $-i\partial_z$. There are two surface state solutions with opposite spin at $k_x, k_y = 0$. By projecting the Hamailtonian onto the subspace of surface states, a effective surface Hamiltonian [57]

$$H_{sf} = -i\hbar v_f(\sigma_x \partial_x + \sigma_y \partial_y) \tag{1.20}$$

is obtained, where $\vec{\sigma}$ denotes spin. H_{sf} gives rise to a Dirac cone that the charge carrier behaves like a relativistic massless particle, schematically depicted in Fig.1.5(a). Moreover, the spin is locked to the momentum, forming the helical nature of surface

states. . The helical nature and the relativistic dispersion have been proved by spin-resolved angle-resolved photoemission spectroscopy (ARPES) measurement in Bi_2Se_3 and $Bi_{1-x}Sb_x$ [20, 58], Fig.1.5(b). ARPES measurement on the Bi_2Te_3

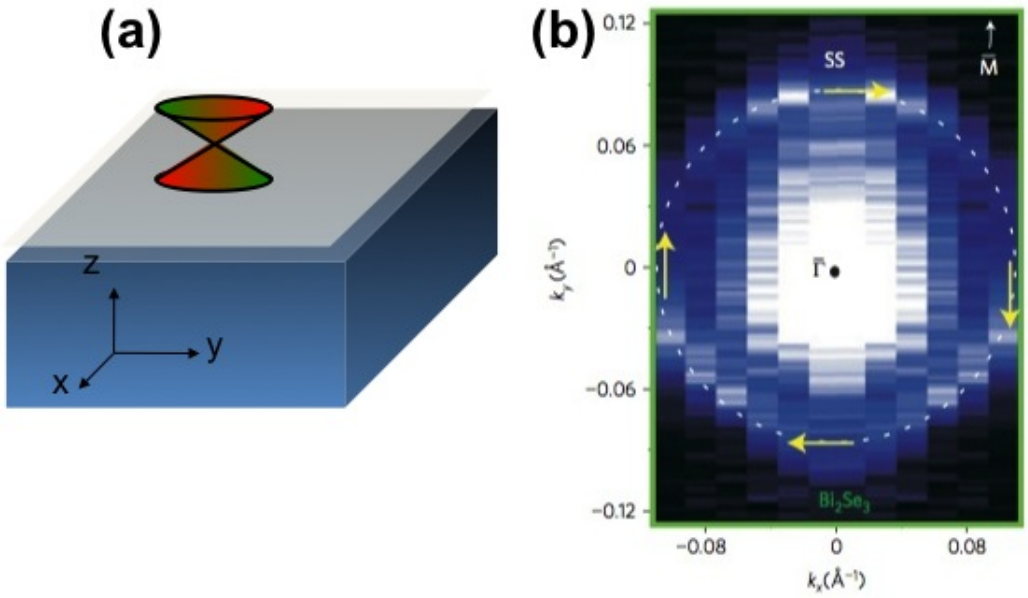

Figure 1.5. (a)The schematic figure of a single Dirac cone on the surface of 3D TI. (b)Spin-resolved ARPES shows the helicity at a cross section of the single Dirac cone on the surface of BiSe. The image is taken from Xia et al. [58]

surface has shown a hexagonal surface state, rather than a circular one [21].

In contrast to the QSH systems, the transport of surface states is not ballistic in 3D TI. Even though backscattering is forbidden by TR symmetry, scattering to other directions is allowed. Thus, the transport of surface Dirac cones will not reveal quantized conductance. Several proposals to transport signatures of surface states have been made, including measurement of weak localization effect [60], in-plane anisotropic magnetoresistance [61], integer quantum Hall effect [22, 24], etc. One of the unambiguous transport evidence of topological surface state is the anomalous Ahronov-Bohm effect of a TI nanowire [23, 25], where the topological surface states only appear when a half-integer of flux quantum threads through the nanowire.

Unlike the 2D QSH effect, the experimental study of which is still only limited in one or two materials, 3D TIs have been theoretically proposed in tens of

materials [62]. The HgTe-related TI material has a similar band structure to HgTe: inverted band structure and zero energy gap. Materials of this type include strained HgTe [24, 63], $\alpha-$Sn [64], $\beta-$HgS [65], $\alpha-$ and $\beta-Ag_2Te$ [66], Heusler compounds such as LnPtBi [67] and LaPtBi [68], HgSe [69], chalcopyrite semiconductors such as $AuTlS_2$ [70], Cu_2 $HgPbSe_4$, $Cu_2CdPbSe_4$, Ag_2 $HgPbSe_4$, $Ag_2CdPbSe_4$ [71,72], filled skutterudites such as $CeOs_4As_{12}$ and $CeOs_4Sb_{12}$ [73]. Another large family of TI materials is the variation of Bi_2Se_3 family which are composed of elements with the strongest atomic spin-orbit coupling. This group includes $TlBiSe_2$ family [74–79], $LaBiTe_3$ family [80], $PbBi_2Se_4$ family [81, 82], Bi_2Te_2Se [83] and $(Bi_{1-x}Sb_x)_2Te_3$ [84, 85], $Cu_xBi_2Se_3$ [86, 87], $Pd_xBi_2Te_3$ [88], and strained Bi_2Te_3 [89]. 3D TIs also exist in other systems and for more details, one can refer to the Ref. [62]

1.6 Magnetic topological insulators

In the section 1.3, we have shown that two-band model can possess non-zero Hall conductance. However, it is still unclear how to realize the two-band model in realistic materials. Instead, we have shown that the Hamiltonian for the QSH effect, which can be viewed as two copies of the two-band Hamiltonian for the QAH effect, has been realized in HgTe/CdTe and InAs/GaSb quantum wells. If one of the block Hamiltonian in Eq.(1.18) becomes a normal insulator, while the other is still in the QAH phase, the overall Hall conductance is nonzero. This can be achieved by introducing magnetic doping, which breaks TR symmetry, into the QSH insulators. Magnetic moments can induce the so-called exchange coupling of electron spin and lead to spin splitting of both conduction and valence bands. This spin splitting can drive a QSH insulator into a QAH phase. Therefore, magnetic doping in TIs provides a practical approach to achieve the QAH state in realistic materials. For different TIs, the forms of exchange coupling are different. Below we will introduce the model Hamiltonian for magnetically doped HgTe/CdTe quantum wells and magnetically doped $(Bi,Sb)_2Te_3$ films.

The HgTe quantum well can be described by the BHZ Hamiltonian (Eq.1.18). With magnetic doping, the exchange coupling between electron spin and magneti-

zation is given by the Hamiltonian [90]

$$H_{m,BHZ} = \begin{pmatrix} g_e & 0 & 0 & 0 \\ 0 & g_h & 0 & 0 \\ 0 & 0 & -g_e & 0 \\ 0 & 0 & 0 & -g_h \end{pmatrix}, \tag{1.21}$$

in the basis of $|E\uparrow\rangle, |H\uparrow\rangle, |E\downarrow\rangle, |H\downarrow\rangle$. Recall that in the previous section, we have shown that tuning the parameter m_o can effectively vary the Hall conductance (Fig.1.3). The above exchange coupling Hamiltonian is equivalent to tuning m_o but with different amplitudes and signs for opposite spin block in the BHZ Hamiltonian. As a consequence, it was found that the QAH phase can be realized when $g_e g_h < 0$ [30]. Indeed, early studies have shown that g_e and g_h possess opposite signs in Mn-doped HgTe [91, 92].

However, HgMnTe is paramagnetic and needs an external magnetic field to polarize magnetization. The out-of-plane magnetic field can cause Landau levels and also leads to quantized Hall conductance (conventional QH effect). This prevents to conclusively distinguish the QAH effect from the conventional QH effect in Mn doped HgTe quantum wells. To distinguish these two effects, other mechanisms, such as in-plane magnetization and strain, need to be introduced. These topics are further discussed in chapter 4.

Another widely studied magnetic topological insulator is thin film of the BiSe/Te family with magnetic doping. The essential difference between HgMnTe quantum wells and magnetically doped $(Bi,Sb)_2Te_3$ lies in different mechanisms of magnetism. In HgMnTe quantum wells, the super-exchange mechanism dominates, leading to antiferromagnetic coupling between different magnetic moments, while for magnetically doped $(Bi,Sb)_2Te_3$ films, the so-called Van Vleck magnetism dominates. Van Vleck magnetism refers to the nonzero matrix element of the spin operator between conduction and valence band, which can be enhanced by band inversion. It is shown that in Fe,Cr doped $(Bi,Sb)_2Te_3$, this mechanism leads to ferromagnetism [31]. Thus, the advantage of this system is that no magnetic field needed and the QH effect can be excluded. For $(Bi,Sb)_2Te_3$ thin films, when the thickness decreases, the top and bottom surface states become hybridized. The effective Hamiltonian can be written in the hybridized basis $|+\uparrow\rangle, |-\downarrow\rangle, |+\downarrow\rangle, |-\uparrow\rangle$, where $\pm$ denotes the bonding/anti-bonding of the top and bottom surface states

$|\pm\uparrow\rangle = (|t\uparrow\rangle \pm |b\uparrow\rangle)/\sqrt{2}; |\pm\downarrow\rangle = (|t\downarrow\rangle \pm |b\downarrow\rangle)/\sqrt{2}$. In this basis, the Hamiltonian has the same form as for BHZ model. However, exchange Hamiltonian in this system is slightly different under the above basis $|+\uparrow\rangle, |-,\downarrow\rangle, |+,\downarrow\rangle, |-,\uparrow\rangle$ and is given by

$$H_{m,BiSe} = \begin{pmatrix} g_+ & 0 & 0 & 0 \\ 0 & -g_- & 0 & 0 \\ 0 & 0 & -g_+ & 0 \\ 0 & 0 & 0 & g_- \end{pmatrix}, \tag{1.22}$$

The above exchange Hamiltonian can naturally drive the system into the QAH phase and the first-principle calculation by Yu et al [31] has indeed shown that (Cr,Fe) doped Bi_2Se_3, Bi_2Te_3, Sb_2Te_3 are magnetically-ordered and exhibit quantized Hall conductance. This theoretical prediction was first confirmed by Chang et al's experiments [59], in which a quantized Hall conductance and a negligible longitudinal resistance were observed by transport measurements, as shown in Fig.1.6. The experimental observation of the exact quantization of Hall conductance and negligible longitudinal resistance confirm dissipationless nature of transport for the QAH effect [93–96].

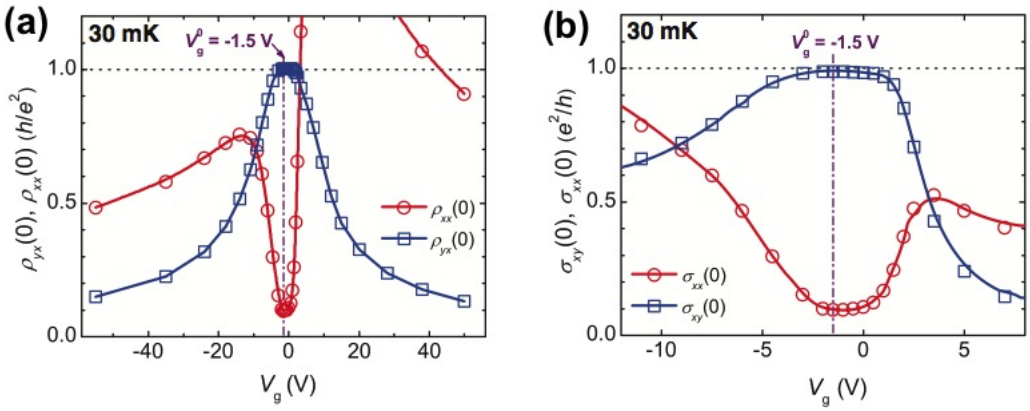

Figure 1.6. The first Hall measurement of the QAH system in $Cr_{0.15}(Bi_{0.1}Sb_{0.9})_{1.85}Te_3$ film. (a) The Hall resistivity(blue) and the longitudinal resistivity(red). (b)The conductance is obtained from the resistivity through the relation $\sigma_{xy} = \rho_{yx}/(\rho_{yx}^2 + \rho_{xx}^2)$ and $\sigma_{xx} = \rho_{xx}/(\rho_{yx}^2 + \rho_{xx}^2)$ .The figures is taken from Ref [59].

1.7 Overview and organization of this dissertation

The research of TIs and the QAH states, as well as other new topological states, provide a new research era of the interplay between symmetry and topological phases. It also inspires potential applications in nano-electronics with low energy consumption. Experimentally, the existence of boundary modes in topological phases can be explored by different experimental techniques, including ARPES [20, 21, 58], scanning transmission microscopy(STM) [97–99] and transport measurements [60, 61, 100]. ARPES and STM measurements directly probe energy dispersions of surface states of a TI, which agree well with theories. However, transport measurements are complicated by disorder and additional bulk carriers. The objective of this work is to understand transport properties of topological insulators theoretically.

In view of the broad objective stated above, our specific studies include predictions of the QAH effect in magnetic TI without orbital effect and to understand transport signatures of 3D TI nano-structures. The organization of this dissertation is as the following: Chapter 2 introduces the methods used for numerical calculation of transport properties in the remaining of the thesis. Chapter 3 discusses the origin of the magnetoconductance oscillation in TI nanowires and the localization physics of topological surface states. The topological sates appear at half-integer flux quanta threading through the nanowire and show a much longer localization length than non-topological states. Our results are supported by magneto-transport measurements in TI nanotubes. Chapter 4 and 5 discuss the realization of the QAH effect in magnetic TI without orbital effects. The effect of in-plane magnetization on the Hall conductance in Mn doped HgTe quantum wells is discussed in Chapter 4. The inclusion of Zeeman coupling causes a reentrant QAH conductance as the in-plane magnetic field increases. Moreover, we present an argument about the relationship between in-plane reflection symmetry and the QAH states. Using symmetry analysis, we show that the QAH effect can be realized in strained HgMnTe quantum wells without any orbital effect. In chapter 5, the resistance of disordered QAH system is studied when rotating magnetization. The quantization of the Hall conductance is robust against disorder. In the end, conclusions and open problems are given in Chapter 6.

Chapter 2
Theoretical fundamentals for transport in topological insulator nanostructures

2.1 Landauer-Büttiker formalism

In this chapter, we will first briefly introduce the Landauer-Büttiker formalism, which has been widely used for the calculation of transport properties of mesoscopic systems [101]. This formalism simulates experimental condition of electronic transport by connecting the device with macroscopic contacts(electron reservoirs) via leads. Leads are ballistic conductors with M transverse modes and are assumed to be in equilibrium with contacts. For a mesoscopic system, in which the phase coherence is maintained and the interference effect can be neglected in the sample, the conductance is independent of the width and the length of the sample. Landauer found that for a mesoscopic system in a two-terminal structure, the conductance is given by $G = \frac{e^2}{h}MT$, where T is the average probability of an electron transmit between the two leads. The conductance only depends the number of transverse modes and transmission probability in the conductor. For multi-terminal structures, Büttiker noted that there is no qualitative difference between the current and voltage probes. He generalized Landauer's formula to multi-probe problems by treating the current and voltage probes on an equal footing. As shown in Fig.2.1, we consider N leads with the current and voltage in each lead denoted as I_p and V_p, respectively, where p denotes the $p-th$ lead. From the Landauer-Büttiker formula,

the current is related to voltage by $I_p = \sum_q G_{pq}(V_p - V_q)$. G_{qp} is the conductance coefficient related to the transmissions functions by

$$G_{qp} = \frac{e^2}{h} T_{qp}, \tag{2.1}$$

where T_{qp} is the transmission matrix that describes the transmission probability from lead p to lead q, as depicted in Fig.2.1.

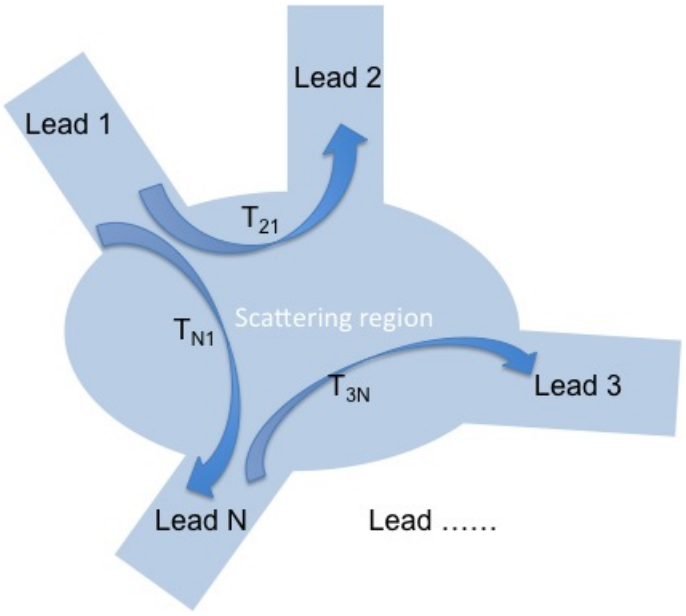

Figure 2.1. A schematic plot showing the transmission between leads.

This formula has been used to explain the transport of edge modes in the QH, QSH and QAH systems. Here we will take a QH system with one chiral edge mode in a four-terminal geometry (Fig.2.2) as an example. Let us assume the chiral edge mode is counter-clockwise. The transmissions are given by $T_{41} = T_{24} = T_{32} = T_{13} = 1$ and other transmissions are 0. Landauer-Büttiker formula gives the matrix equation

$$\begin{pmatrix} I_1 \\ I_2 \\ I_3 \\ I_4 \end{pmatrix} = \frac{e^2}{h} \begin{pmatrix} 1 & 0 & -1 & 0 \\ 0 & 1 & 0 & -1 \\ 0 & -1 & 1 & 0 \\ -1 & 0 & 0 & 1 \end{pmatrix} \begin{pmatrix} V_1 \\ V_2 \\ V_3 \\ V_4 \end{pmatrix}. \tag{2.2}$$

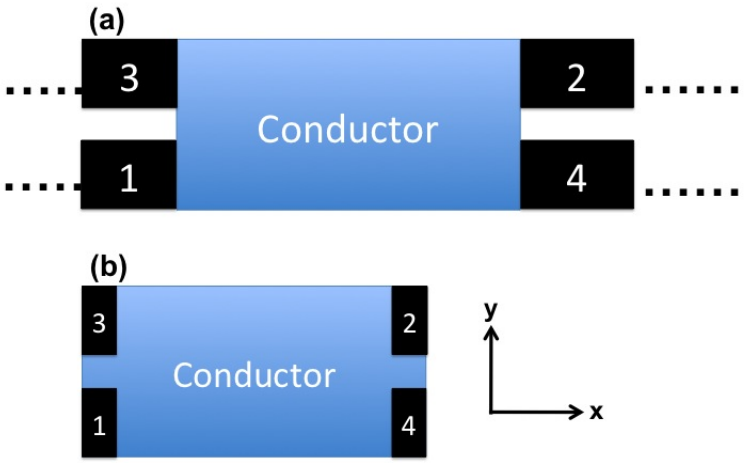

Figure 2.2. (a) is the conductor connecting to semi-infinite leads. (b) is the conductor adding the lead self-energy. The two are conceptually equivalent.

The matrix equation can be simplified by current conservation $I_1 + I_2 + I_3 + I_4 = 0$. Moreover, because the current depends on voltage differences, we can set any probe voltage to 0. Here, we set $V_4 = 0$ and the matrix equation is simplified as

$$\begin{pmatrix} I_1 \\ I_2 \\ I_3 \end{pmatrix} = \frac{e^2}{h} \begin{pmatrix} 1 & 0 & -1 \\ 0 & 1 & 0 \\ 0 & -1 & 1 \end{pmatrix} \begin{pmatrix} V_1 \\ V_2 \\ V_3 \end{pmatrix}. \tag{2.3}$$

The resistance matrix is defined as the inversion of conductance matrix

$$R = \begin{pmatrix} R_{11} & R_{12} & R_{13} \\ R_{21} & R_{22} & R_{23} \\ R31 & R_{32} & R_{33} \end{pmatrix} = \frac{h}{e^2} \begin{pmatrix} 1 & 1 & 1 \\ 0 & 1 & 0 \\ 0 & 1 & 1 \end{pmatrix}. \tag{2.4}$$

To calculate the Hall resistance, we set voltage probes at terminal 3, 4 and current probes at terminal 1,2. The Hall resistance is given by $R_H = \frac{V_3 - V_4}{I_1}$ with $V_4 = 0, I_2 = -I_1$ and $V_3 = R_{31}I_1 + R_{32}I_2$. Thus, $R_H = R_{31} - R_{32} = \frac{h}{e^2}$. To calculate the longitudinal resistance, we set voltage probes at terminal 1, 4 and current probes at terminal 2, 3. The longitudinal resistance is given by $R_L = \frac{V_1 - V_4}{I_3}$ with $V_4 = 0, I_3 = -I_2$ and $V_1 = R_{12}I_2 + R_{13}I_3$. Thus, $R_L = R_{12} - R_{13} = 0$. Landauer-Büttiker formula gives the expected values of the resistances for a system

with chiral edge modes which are experimentally confirmed in QH systems [93–96].

The central task of transport calculations is to evaluate the transmission functions T_{qp}, which can be obtained from the S-matrix. The S-matrix connects the incoming and outgoing wave amplitudes at the different leads. Consider the propagation between two leads, the S-matrix is

$$S = \begin{pmatrix} r & t' \\ t & r' \end{pmatrix}, \tag{2.5}$$

where r is the reflection matrix in one lead and its size is determined by the number of modes in the lead. t is the transmission matrix across the conductor from one lead to the other. r' and t' describe the transport along the reversed direction of r and t. Different methods can be applied to evaluate the S-matrix, depending on the type of the problem. One useful technique is to express the S-matrix in terms of Green's function by the Fisher-Lee relation [101],

$$s_{nm,qp} = -\delta_{nm}\delta_{qp} + \frac{i\hbar}{a}\sqrt{v_{nq}v_{mp}} \sum_{q_i,p_j} \chi_n^*(q_i) G_{qp}^R(q_i,p_j), \chi_m(p_j), \tag{2.6}$$

where $n(m)$ denotes the conducting channel in lead $q(p)$, q_i denotes the transverse lattice site in lead q, v_{nq} is the longitudinal velocity in the lead, χ_n is the transverse wave function in the lead, a is the lattice constant, $G_{qp}^R(q_i,p_j)$ is the retarded Green's function that gives the propagation amplitude from transverse site i in lead q to transverse site j in lead p. It is a submatrix of Green's function of the full system.The Green's function is defined as

$$G^{R/A} = \frac{1}{E - H \pm i\eta}, \tag{2.7}$$

where H is the full Hamiltonian, η is the imaginary energy, R/A refers to the retarded/advanced solutions. They are related by $G^{R*}(q_i,p_j) = G^A(p_j,q_i)$.

The transmission function can be written in a more compact form $T_{q\neq p} = \sum_{n,m} |s_{nm,qp}|^2 = Tr[\Gamma_q G^R \Gamma_p G^A]$, where $\Gamma_q(q_i,q_i') = \chi_n(q_i)\frac{\hbar v_{nq}}{a}\chi_n^*(q_i')$ describes the coupling between the conductor and the lead. In the clean limit, an electron injected from one terminal transport smoothly to another without any scattering. The electron preserves its eigenstate, and thus $T_{nm} = \delta_{nm}$. For the system with disorder, we need to evaluate the Green's functions explicitly. The diagrammatic perturbation

method is an analytical approach with $(k_f l)^{-1}$ as an expansion parameter [102], where k_f is the Fermi wave vector and l is the mean free path. However, in an extremely disordered regime or when Fermi level is low such that $k_f l \ll 1$, this method is no longer valid and numerical methods are required [102]. In this thesis, we adopt the recursive Green's function method which will be introduced in this chapter.

In this study, the Hamiltonian is written in the tight-binding (TB) representation, which is suitable for describing a lattice of a finite system. It is also easier to introduce disorder and magnetic field in the TB representation. Numerically, to invert the matrix to obtain the Green's function is not computationally efficient since the time cost for computation scales as $(NW)^3$, where W is the number of transverse sites of the sample and N is the length of the sample. Here we adopt a method called the recursive Green's function method, for which the computational time scales as NW^3. The time reduction is because of the slicing treatment of the full Hamiltonian in this method. The sample is cut into several slices and connected by the hopping matrices. The Hamiltonian inversion is done slice by slice. Thus, the matrix size involved in the inversion is W by W. The recursive Green's function method is efficient to compute the S-matrix for a disordered system in TB representation.

In order to understand transport properties in TI nanostructures, we combine the Landauer-Büttiker formalism together with the recursive Green's function method. This chapter is dedicated to describe the methods as the theoretical and numerical background for the following chapter.

2.2 Recursive Green's function method

2.2.1 Derivation of the recursive equations

This section aims in introducing recursive Green's function method and show that it provides a more efficient route for the calculation of the Green's function. This method is used to calculate scattering amplitudes of a noninteracting system described in the TB representation. We will show the slicing scheme (Fig.2.3) of the Hamiltonian and how to use the Dyson's equation to obtain the left-sweep recursive equations that give the scattering amplitude between the first and the

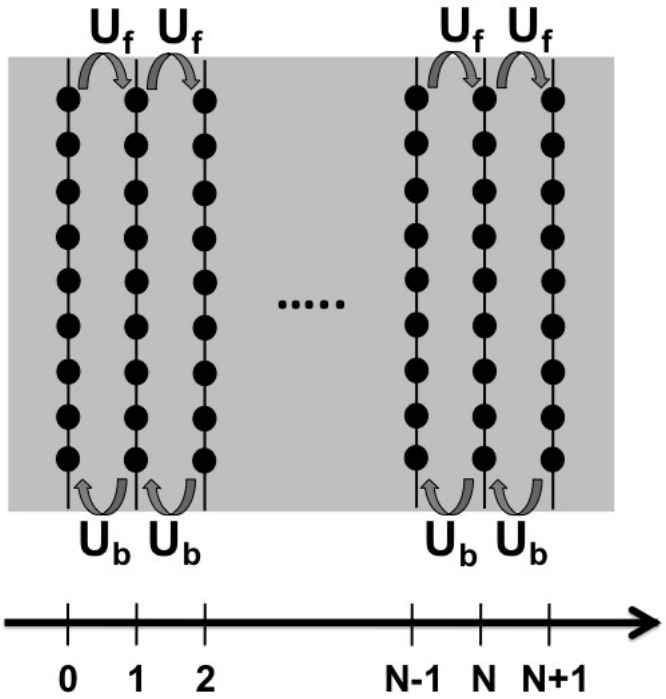

Figure 2.3. The schematic slicing scheme of a free-end system.

last slice. The full Hamiltonian is written in the form

$$\mathcal{H} = \begin{pmatrix} h_0 & U_f & 0 & \cdots & \cdots & 0 \\ U_b & h_1 & U_f & 0 & \cdots & \vdots \\ 0 & U_b & h_2 & U_f & 0 & \vdots \\ \vdots & \vdots & \ddots & \ddots & \ddots & \vdots \\ \vdots & \vdots & \ddots & \ddots & \ddots & U_f \\ 0 & 0 & 0 & \cdots & U_b & h_{N+1} \end{pmatrix}, \tag{2.8}$$

where h_n, $n = 0 \cdots, N+1$, is the Hamiltonian of each slice, U_f is the forward hopping from nth slice to $n+1$th slice and U_b is the backward hopping from nth slice to $n-1$th slice.

For clarity, we use bras and kets to express the full Hamiltonian:

$$\mathcal{H} = \mathcal{H}_{\mathcal{N}} + |N+1\rangle h_{N+1} \langle N+1| + \mathcal{H}' \tag{2.9}$$

, where the kets $|i\rangle$ represent the state at the $i-$th slice and $\mathcal{H}_{\mathcal{N}} = \sum_i^N \{|i\rangle h_i \langle i| + |i\rangle U_b \langle i+1| + |i+1\rangle U_f \langle i|\}$ is the Hamiltonian for the first N slices. $\mathcal{H}'$ is the hopping between the N-th and the N+1-th slice and is treated as the perturbing term

$$\mathcal{H}' = |N\rangle U_b \langle N+1| + |N+1\rangle U_f \langle N|, \tag{2.10}$$

where $U_{f/b}$ denotes the forward/backward hopping matrix.

The underlying concept in recursive Green's function method is to assume that the Green's function of $\mathcal{H}_{\mathcal{N}}$ is known and treat the hopping between the N-th and the N+1-th slice as a perturbation. The exact Green's function can be obtained by Dyson equation

$$G^{N+1} = G_o + G_o \mathcal{H}' G^{N+1}, \tag{2.11}$$

$$\text{where } G_o = G^N + \frac{|N+1\rangle\langle N+1|}{E - h_{N+1}}. \tag{2.12}$$

By plugging Eq. 2.10 and 2.12 into Eq. 2.11, we get

$$\begin{aligned} G^{N+1} &= \left(G^N + \frac{|N+1\rangle\langle N+1|}{E - h_{N+1}}\right) \\ &\quad \left(1 + \left(|N\rangle U_b \langle N+1| + |N+1\rangle U_f \langle N|\right) G^{N+1}\right). \end{aligned} \tag{2.13}$$

The submatrix that gives the propagation from the slice 0 to $N+1$ is

$$\langle 0|G^{N+1}|N+1\rangle = \langle 0|G^N|N\rangle U_b \langle N+1|G^{N+1}|N+1\rangle, \tag{2.14}$$

where

$$\begin{aligned} \langle N+1|G^{N+1}|N+1\rangle &= \frac{1}{E - h_{N+1}}(1 + U_f \langle N|G^{N+1}|N+1\rangle) \\ &= \frac{1}{E - h_{N+1}} \\ &\quad (1 + U_f \langle N|G^N|N\rangle U_b \langle N+1|G^{N+1}|N+1\rangle) \\ &= \frac{1}{E - h_{N+1} - U_f \langle N|G^N|N\rangle U_b} \end{aligned} \tag{2.15}$$

In the above equation, the sub-matrix $\langle N|G^{N+1}|N+1\rangle$ is obtained by calculating

the sub-matrix of Eq. (2.13). Eq.(2.14) and (2.15) are the two main equations used to obtain the Green's function. The first two steps of the iteration are presented in the following with the initial condition of free Green's function

$$\langle 0|G^0|0\rangle = \frac{1}{E-h_0}. \tag{2.16}$$

At the first step of the iteration, Eqs.(2.14) and (2.15) give

$$\langle 0|G^1|1\rangle = \langle 0|G^0|0\rangle U_b \langle 1|G^1|1\rangle \tag{2.17}$$

$$\langle 1|G^1|1\rangle = \frac{1}{E-h_1-U_f\langle 0|G^0|0\rangle U_b}. \tag{2.18}$$

At the second step of the iteration , Eqs.(2.14) and (2.15) give

$$\langle 0|G^2|2\rangle = \langle 0|G^1|1\rangle U_b \langle 2|G^2|2\rangle \tag{2.19}$$

$$\langle 2|G^2|2\rangle = \frac{1}{E-h_2-U_f\langle 1|G^1|1\rangle U_b}. \tag{2.20}$$

We can follow this iteration to get the Green's function at the slice N. So far, we have introduced the left-to-right sweep Green's function. It can be generalized easily to the right-to-left sweep only by changing slice indices. For two-terminal transmission functions, one sweep is enough for determination of transmission. In some cases, for example, density of states, multi-terminal transmission, both sweeps are needed. However, for the above calculation, the influence from the lead has not been taken into account, which will be included as a boundary condition, as described in the next subsection.

2.2.2 Connection to leads

In this section, we will discuss how to take into account the influence of leads. Leads are ballistic conductors with a semi-infinite length, and consequently, the matrix of the full Hamiltonian that includes the leads and a central conductor has infinite dimensions. It is not possible to obtain the Green's function by inverting the full Hamiltonian. A method of truncating the matrix for computing the Green's function will be described. In this method, the effect of the semi-infinite lead enters the Hamiltonian of the conductor through the form of self-energy. The

self-energy is obtained from the Green's function of a semi-infinite lead which can be evaluated numerically by calculating $\langle N|G^N|N\rangle$ using Eq.(2.15). A convergence test is required to ensure that N is large enough to simulate a semi-infinite lead. Nevertheless, for the case of parabolic band dispersion in the leads, analytical expressions for the Green's functions of leads can be obtained. This analytical solution will be given later in this section.

First, we consider how to truncate the matrix when there is one lead. The retarded Green's function of the whole system is $G^R = (E - H + i\eta)^{-1}$ (the superscript R will be dropped for simplicity below). The overall Green's function is partitioned into submatrices and defined as follows:

$$\begin{pmatrix} G_L & G_{LC} \\ G_{CL} & G_C \end{pmatrix} \equiv \begin{pmatrix} E - H_L + i\eta & \tau \\ \tau^\dagger & E - H_C \end{pmatrix}^{-1}, \tag{2.21}$$

where $(E + i\eta - H_L)$ represents the isolated lead, $(E - H_C)$ represents the isolated conductor and τ is the coupling matrix that couples the lead and the conductor.

For one-dimensional case, τ is a $N_L \times N_C$ matrix, of which N_L is the length of the lead and N_C is the length of the conductor. When only the nearest neighbor hopping is taken into account, the matrix τ takes the following form

$$\tau = \begin{pmatrix} 0 & \dots & 0 \\ \vdots & \vdots & 0 \\ t & 0 \dots & 0 \end{pmatrix}, \tag{2.22}$$

where t describes the hopping between the lead and the conductor. By multiplying by $(E - H + i\eta)$ on both sides of the Eq (2.21), one gets

$$(E - H_L + i\eta)G_{LC} + \tau G_C = 0 \tag{2.23}$$

$$\tau^\dagger G_{LC} + (E - H_C)G_C = I. \tag{2.24}$$

Eq.(2.23) gives

$$G_{LC} = -g^L \tau G_C \tag{2.25}$$

$$\text{,where } g^L = (E - H_L + i\eta)^{-1} \tag{2.26}$$

which is the retarded Green's function of a semi-infinite lead. By substituting Eq.(2.25) into Eq.(2.24), we obtain

$$G_C = (E - H_c - \Sigma^L)^{-1} \tag{2.27}$$

$$\Sigma^L = \tau^\dagger g^L \tau, \tag{2.28}$$

where Σ^L is called the self-energy of the lead and G_C gives the propagation of electrons between two sites inside the conductor taking into account the effect of leads.

By introducing Σ^L, the infinite large matrix of the original Hamiltonian is reduced to a finite-size matrix. The self-energy Σ^L contains the information from the semi-infinite lead. It is added as a boundary condition of the conductor (Fig.2.2). When there are more than one lead, it is assumed that different leads are independent, thus the effective self-energy is the sum $\Sigma^L = \sum_p \Sigma_p^L$.

Next, we will show the analytic solutions for the self-energy and the Green's function of the lead. If the lead is a simple normal metal with a parabolic dispersion, the Green's function can be computed analytically. In TB representation, the Hamiltonian for the 1D chain is $-t\sum_j (C_{j+1}^\dagger C_j + C_{j-1}^\dagger C_j)$ and the eigenenergy is $E = -2t\cos(ka)$, where $t = \frac{\hbar^2}{2ma}$ when compared to the continuum limit $a \to 0$. For a 1D semi-infinite lead lying along the x-direction with the open boundary at $x = 0$, the wave function in TB representation is $\Psi(x) = \sqrt{\frac{2}{N_L}}\sin(kx)$ which satisfies the boundary condition $\Psi(0) = 0$. We start with the eigenfunction expansion of the Green's function

$$g^L(E, x, x') = \sum_k \frac{\Psi^*(x')\Psi(x)}{E - \epsilon_k + i\eta}. \tag{2.29}$$

To compute the self-energy of the lead, we only need to evaluate the Green's function on the interface. Thus, we will set $x' = x$ in Eq.(2.29). Substitute the wave functions into the expansion and replace the summation by the integral $\sum_k \to \frac{L}{\pi}\int dk$, where $L = N_L a$ and $L \to \infty$, we obtain

$$\begin{aligned} g^L(E, x, x) &= \frac{a}{2\pi}\int_0^\infty dk \frac{2 - e^{2ikx} - e^{-2ikx}}{E - \epsilon_k + i\eta} \\ &= \frac{-ma}{\pi\hbar^2}\int_{-\infty}^\infty dk \frac{1 - e^{2ikx}}{(k + \sqrt{E'} + i\eta)(k - \sqrt{E'} - i\eta)} \end{aligned}$$

$$
\begin{aligned}
&= \frac{ima}{\hbar^2 k}(e^{2ikx}-1) \\
&= \frac{-2ma}{\hbar^2 k}e^{ikx}\sin(kx),
\end{aligned} \tag{2.30}
$$

where $\sqrt{E'} = \sqrt{2mE}/\hbar = k$ in the continuum limit. Take the continuum limit $a \to 0$, then we have $\sin(ka) \to ka$. E.q.(2.30) gives $g^L = -e^{ikx}/t$. To obtain the surface Green's function, we set $x = a$, which is the first lattice site in the conductor. Thus, the surface Green's function is $g^L(E, x = a) = -e^{ika}/t$ and the self-energy from the lead is $\Sigma^L = -te^{ika}$ given by E.q.(2.28) [101].

For a quasi-1D semi-infinite lead, the retarded surface Green's function can also be obtained by eigenfunction expansion. We assume the lead lies along the x-direction and the transverse side is along the y-direction. The wave function is

$$
\Psi(x,y) = \sqrt{\frac{2}{N_L}}\sin(kx)\chi_m(y), \tag{2.31}
$$

where $\chi_m(y)$ is the transverse wave function. Substituting the wave functions into the wave function expansion of the Green's function $g^L(E,x,y,x',y') = \sum_{k,m}\frac{\Psi^*(x',y')\Psi(x,y)}{E-\epsilon_k+i\eta}$ and follow the same procedure as the 1D case, we obtain

$$
g^L(E,x,y',x,y) = \frac{-e^{ika}}{t}\sum_m \chi_m^*(y')\chi_m(y). \tag{2.32}
$$

In this dissertation, we assume hard-wall boundary condition for the transverse direction with the edges at $y = 0$ and $y = (N_y+1)a$. Thus, the transverse wave functions are $\chi_m(y) = \sqrt{\frac{2}{N_y+1}}\sin(k_y y)$ with $k_y = \frac{m\pi}{(N_y+1)a}$ and $m = 1 \ldots N_y$. The longitudinal wave vector k is given by the dispersion relation $k = \frac{1}{a}\cos^{-1}\left(\frac{E+2t\cos(k_y a)}{-2t}\right)$.

The generalization to 3D systems is straightforward from Eq.(2.32). The transverse modes include the modes along the third dimension. Thus, $\chi_m(y)$ is replaced by $\chi_{m,n}(y,z) = \sqrt{\frac{4}{(N_y+1)(N_z+1)}}\sin(k_y y)\sin(k_z z)$. The longitudinal wave vector is $k = \frac{1}{a}\cos^{-1}\left(\frac{E+2t\cos(k_y a)+2t\cos(k_z a)}{-2t}\right)$.

With the surface Green's function at hand, we can turn back to the boundary conditions for the recursive equations Eq.(2.14) and Eq.(2.15).

For a two-terminal device (Fig.2.4), the initial condition E.q.(2.16) is replaced with $\langle 0|G^0|0\rangle = g^L$. At the rightmost slice (say, the N-th slice), the conductor is

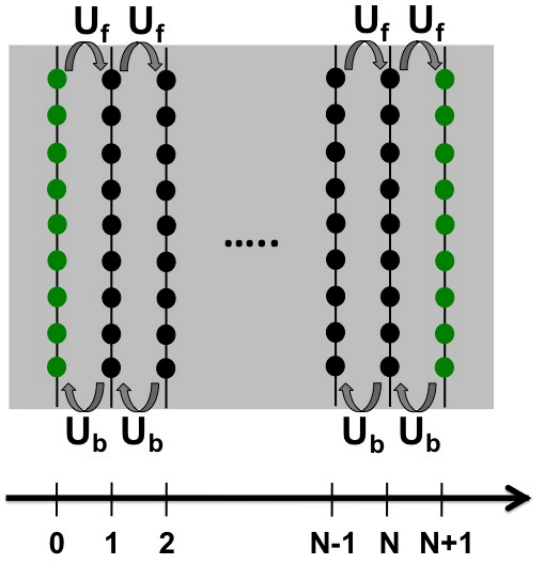

Figure 2.4. The schematic slicing scheme with two-terminal leads. The leftmost and rightmost slices are dressed with the self-energy of the lead.

connected to the right lead. $(E - h_{N+1})$ in Eq.(2.15) is replaced with $g^{L^{-1}}$. The Green's function $\langle 0|G^{N+1}|N+1\rangle$ is the final result that we need for the calculation of transmission. It gives the transmission probability from slice 0 to $N+1$ taking into account the influence of the leads. We will show an example of the calculation of the transmission function for a two-terminal device in the next section.

2.3 Analytic solution for an one-dimensional example

To get a better understanding of the Landauer-Büttiker formula for transport calculation, we study a simple example of the transport in a 1D chain, which can be solved analytically. Without adding any disorder or potential barrier, the Green's function given by Eq.(2.28) is the same as the Green's function of an infinite long conductor. The 1D conductor is separated into 3 pieces, a left lead, the conductor and a right lead. For simplicity, we consider a conductor with two lattice sites $(N = 2)$, in which the analytic solutions can be easily achieved. The Hamiltonian

of the conductor with two sites is

$$H_C = \begin{pmatrix} 0 & -t \\ -t & 0 \end{pmatrix}. \tag{2.33}$$

In TB representation, the energy dispersion and the velocity of the incident particles are

$$E = -2t\cos(ka) \tag{2.34}$$

$$v = \frac{1}{\hbar}\frac{\partial H}{\partial k} = \frac{2at}{\hbar}\sin(ka). \tag{2.35}$$

The influence of the leads to transmission can be dealt with in the form of self-energy added to the Hamiltonian H_C

$$\Sigma^L = -t \begin{pmatrix} e^{ika} & 0 \\ 0 & e^{ika} \end{pmatrix}. \tag{2.36}$$

The Green's function of the whole system (including the conductor and leads) is obtained by inversion

$$G(E) = \frac{1}{E - H_C - \Sigma^R} \tag{2.37}$$

$$= \begin{pmatrix} E + te^{ika} & -t \\ -t & E + te^{ika} \end{pmatrix} / [(E + te^{ika})^2 - t^2]. \tag{2.38}$$

Now we can calculate transmission probability $T = |S_{1N}|^2$. According to Fisher-Lee relation, the scattering amplitude is $S_{1N} = i\frac{\hbar v}{a}G^R_{1N}$ for transmission and $S_{11} = -1 + i\frac{\hbar v}{a}G^R_{11}$ for reflection, so we have

$$S_{1N} = \frac{-i2t^2\sin(ka)}{[(E + te^{ika})^2 - t^2]} = e^{ika}, \tag{2.39}$$

$$S_{11} = 0, \tag{2.40}$$

where we have substituted $E = -2t\cos(ka)$ and made the use of $-2t\cos(ka) + te^{ika} = -te^{-ika}$. Therefore, the transmission probability is $T_{1N} = 1$ and $T_{11} = |S_{11}|^2 = 0$. This is reasonable because there is no disorder nor potential barrier in

the wire, an electron should have perfect transmission.

2.4 Summary of the calculation

In this chapter, the Landauer-Büttiker formula and the recursive Green's function method for calculating the conductance in mesoscopic systems are introduced. The important steps in the calculation for the transmission are summarized in this section. The main parts of the calculation include input of the Hamiltonian, iteration and the calculation of transmission.

I. **Input of the Hamiltonian:**

The Hamiltonian is written in the form given in E.q.(2.8) , where in clean limit, $h_1 = h_2 = \cdots = h_N$. For a two-terminal structure, h_0 and h_{N+1} are the slices that connect to leads. $h_0 = h_1 + \Sigma^L$, where Σ^L is the self-energy of the lead. In this study, all leads are taken to be the same. Thus, $h_{N+1} = h_0$. The self-energy of the lead is $\Sigma^L(E, y, y') = t^2 g^L(E, y, y')$, where $g^L(E, y, y')$ is given by E.q.(2.32).

II. **Iteration:** After the input of the sliced Hamiltonian and the self-energy, there is enough information to calculate the Green's function by iteration equations E.q.(2.14) and E.q.(2.15) with the boundary conditions taking into account the effect of lead.

III. **Calculation of transmission:** The transmission function is calculated with the compact form $T_{qp} = Tr[\Gamma_q G^R \Gamma_p G^A]$, in which the Green's functions and the Gamma matrices are written in the site indices along the transverse directions. The trace is over the site indices:

$$T_{qp} = \sum_{q_i, p_j, q_i', p_j'} \left\{ \Gamma_q(q_i, q_i') G^R_{0,N+1}(q_i', p_j') \Gamma_p(p_j', p_j) G^A_{0,N+1}(p_j, q_i) \right\}, \quad (2.41)$$

where $\Gamma_q = (q_i, q_i') = \sum_n \frac{\hbar v_{nq}}{a} \chi_n(q_i) \chi_n^*(q_i')$ and $\Gamma_p(p_j', p_j) = \sum_m \frac{\hbar v_{mp}}{a} \chi_m(p_j') \chi_m^*(p_j)$. $G^R_{0,N+1}(q_i', p_j')$ is obtained from the iteration equations in the previous step. The advanced Green's function is obtained by the complex conjugate of the retarded Green's function: $G^A_{0,N+1}(p_j, q_i) = G^R_{0,N+1}(q_i, p_j)^*$.

Chapter 3
Transport in disordered topological insulator nano-structures

TIs are bulk insulators with unusual gapless metallic surface states protected by TR symmetry [52, 55, 103]. The topological surface states are expected to yield salient phenomena, such as spin-momentum locking and the suppression of non-magnetic backscattering. However, the current experimental observation of gapless surface states mainly comes from the surface sensitive technique, such as ARPES and STM. The signatures of topological surface states in electrical transports are complicated by the fact that the samples often have dominating conduction from bulk channels due to high density of carriers from the impurity states. One of the approaches to enhance the surface contribution is to increase the surface-to-volume ratio by reducing the sample size down to nanometer scale. Pioneering study in this direction has been carried out in Bi_2Se_3 nanoribbons [23, 104, 105] and Bi_2Te_3 nanowires [106]. Another possible strategy is to increase disorder scattering in nanoscale samples. A sufficiently strong disorder should localize bulk conduction but may not significantly affect topological surface states since the surface conduction is predicted to be more robust against disorder compared to that of bulk carriers. In this chapter, we study transport of disordered topological insulator nanostructures based on the numerical methods discussed in the last chapter and demonstrate the robustness of topological states.Moreover, our numerical results agree with the experimental observation that the magneto-conductance oscillates with ϕ_0-periodicity in highly disordered Bi_2Te_3 nanotubes.

3.1 Theoretical study of surface states of TI nanowires in the clean limit

In this section, we will present the energy dispersion, wave function distribution and magneto-conductance of TI nanowire in the clean limit. The analytical solution will be given first for a physical understanding and then followed by numerical results.

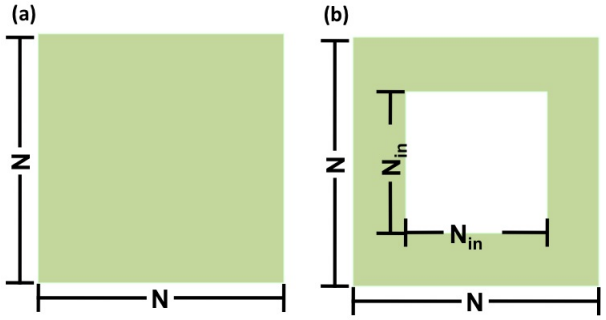

Figure 3.1. The cross section of a nanowire (a) and a nanotube (b) used in the numerical calculation.

We first consider a topological insulator nanowire with only one closed surface, as shown in Fig.3.1(a). The behavior of surface states of a TI nanowire can be understood by the effective Hamiltonian of topological surface states(E.q.(1.20)).

We may start from the four band Dirac type of Hamiltonian of bulk TIs to obtain the effective Hamiltonian of topological surface states that has been obtained in Ref [107], also see Appendix A. The nanowire is modeled by a cylinder with the radius R and an infinite length. When a magnetic field is applied to penetrate into the nanowire, we need to apply Pierels substitution $\vec{p} \to \vec{p} - \frac{e}{\hbar}\vec{A}$ to the momentum. The total magnetic flux enclosed by the surface of the nanowire is $B\pi R^2 = A_\phi 2\pi R = \eta\phi_0$. Thus, we can choose the vector potential as $\vec{A} = A_\phi\hat{\phi} = \frac{\eta\phi_0}{2\pi R}$ and the corresponding Hamiltonian is

$$H^{\mathbf{n}}_{eff} = \frac{\hbar v_f}{2R} + \hbar v_f \begin{pmatrix} -\frac{1}{R}(i\partial_\phi + \eta) & ike^{-i\phi} \\ -ike^{i\phi} & \frac{1}{R}(i\partial_\phi + \eta). \end{pmatrix} \tag{3.1}$$

The eigenenergy for this Hatmiltonian is

$$E_{kl} = \pm\hbar v_f \sqrt{k^2 + (\frac{l + 1/2 - \eta}{R})^2}, \tag{3.2}$$

where v_f is the Fermi velocity, k is the wave vector along the wire direction and $l+1/2$ is the angular momentum of surface electrons with l to be an integer number and equals to $0, \pm 1 \pm 2 \ldots$.

The energy dispersion depends on the value of the magnetic flux. TR symmetry exists in this system when η takes the integer or half-integer values in units of flux quantum and will lead to double degeneracy. When η is an integer, the bands are parabolic and doubly degenerate($l + 1/2 = \pm 1/2, \pm 3/2 \ldots$). There is a gap of $2\hbar v_f \frac{l+1/2}{R}$. In contrast, when η equals to half- integers, a pair of linear mode with $l + 1/2 = \eta$ appears and the gap closes.

This result can be understood by Berry's phase. When a surface electron moves along a closed trajectory around the curved surface of a nanowire, the electron spin equivalently rotates by 2π due to spin-momentum locking, leading to a Berry phase π. It means that the wave function satisfies antiperiodic boundary condition along the perimeter direction. Thus, the allowed angular momentum takes half-integer value $l + 1/2$, which leads to a gap for all surface sub-bands. However, when there is magnetic flux threading through the nanowire, the surface electron gains an additional phase from magnetic flux. When magnetic flux takes half-integer value of flux quanta ($(n + 1/2)\phi_0$), which gives rise to an additional phase of π and cancels out the Berry phase, the gap of a pair of surface sub-bands closes again.

We applied the bulk Hamiltonian to a cuboid, for which the cross sectional surface is a $N \times N$ square as in Fig.3.1(a). We consider the wire lying along the x-direction, so as the magnetic field. The cross section of the nanowire is on the yz plane. We employed the tight-binding Hamiltonian on a simple cubic lattice in which only the nearest neighbor hopping is considered [108]. The Hamiltonian is written as

$$H = H_0 + H_{soc} + H_\gamma \tag{3.3}$$

$$H_0 = (\epsilon - t \sum_{i,\delta} (C^\dagger_{i+\delta} C_i + C^\dagger_{i-\delta} C_i))\Gamma_0 \tag{3.4}$$

$$H_{soc} = iA\sum_{i,\delta}(C^{\dagger}_{i+\delta}C_i - C^{\dagger}_{i-\delta}C_i)\Gamma_i \tag{3.5}$$

$$H_{\gamma} = \gamma\sum_{i,\delta}(2 - C^{\dagger}_{i+\delta}C_i - C^{\dagger}_{i-\delta}C_i)I, \tag{3.6}$$

where i denotes the x, y, z direction. $\Gamma_x = s_z \otimes \sigma_x$, $\Gamma_y = -I \otimes \sigma_y$, $\Gamma_z = s_x \otimes \sigma_x$, $\Gamma_0 = I \otimes \sigma_z$, where σ_i acts on the orbital space and s_i acts on the spin degree of freedom. a is the lattice constant, which we set to unity in the calculation. t is the hopping term between the two nearest neighbor atoms and $\epsilon - 6t$ corresponds to the mass term. A is the strength of spin-orbit coupling and taken to be 1. γ term breaks particle-hole symmetry. In our calculation, the parameters were chosen such that $\epsilon = 4t$, $t = 1$. The choice of the parameter is in the regime $2t < |\epsilon| < 6t$ to realize the strong topological insulator phase [107] and gives a maximum bulk band gap of $4t$. Since γ does not affect the topology, we set it to be zero in our calculations for simplicity. Below, all energies are in units of t and length in units of a. The magnetic field is included through the standard Peierls substitution. To simulate the magnetic field B applied along the wire (the x-direction), we choose the Landau gauge for the vector potential $\vec{A} = (0, -Bz, 0)$, corresponding to an additional phase factor in the hopping term along the y-direction ($tC^{\dagger}_{i,y+1}C_{i,y} \to te^{(i2\pi z\phi/\phi_0)}C^{\dagger}_{i,y+1}C_{i,y}$).

3.1.1 Dispersion and wave function distribution

We first calculate energy dispersion and wave functions in three different magnetic flux distributions. In the calculation, the x-direction is taken to be infinite. Due to the translation symmetry along the x direction, we can apply the Fourier transform to the x position in the Hamiltonian, leading to

$$H_0 = (\epsilon - t\sum_{y,z,\delta}(C^{\dagger}_{i+\delta}C_i + C^{\dagger}_{i-\delta}C_i) - 2t\sum_{k_x}\cos k_x)\Gamma_0 \tag{3.7}$$

$$H_{soc} = i\sum_{y,z,\delta}(C^{\dagger}_{i+\delta}C_i - C^{\dagger}_{i-\delta}C_i)\Gamma_i - 2\sum_{k_x}\sin k_x\Gamma_i \tag{3.8}$$

$$H_{\gamma} = \gamma\sum_{y,z,\delta}(2 - C^{\dagger}_{i+\delta}C_i - C^{\dagger}_{i-\delta}C_i)I - \gamma\sum_{k_x}(2 - 2\cos k_x)I. \tag{3.9}$$

The parameters are chosen as $\epsilon = 4t, \gamma = 0$ and t is set to unity. We diagonalize the Hamiltonian at each k_x numerically and compare three different magnetic flux distributions, (1) no magnetic flux, (2) half magnetic flux quantum at the center

plaquette, (3)half magnetic flux quantum homogeneously distributed over the whole cross section. In the case (1) and (2), the Hamiltonians have TR symmetry, while in the case (3), the TR symmetry is broken. However, in the case (3), since the surface state is mainly localized at the boundary of the nanowire, the enclosed magnetic flux by the surface state is still approximately π. Thus, we expect TR symmetry still approximately exists for surfaces in the case (3). In the following, we will present the results and discussions for these three cases.

(1)*No magnetic flux.* The full Hamiltonian is time-reversal invariant. Fig.3.2(a) shows parabolic dispersion. All the subbands are doubly degenerate due to TR symmetry, and a gap opens up as a result of the Berry phase.

(2)*Magnetic flux of $\phi_0/2$ only at the center plaquette.* For a nanowire with a $\phi_0/2$ flux at the center, the Hamiltonian is still time-reversal invariant. In the TB representation, only the hopping across the plaquettes that are below the center one gains a phase π, see Fig.3.3(a). Under time-reversal operation, the magnetic flux flips sign but the hopping terms are invariant since $te^{i\pi} = te^{-i\pi}$. The gap closes because the surface modes gain an additional phase that cancels out the Berry's phase as discussed at the beginning of this section. Due to the TR symmetry, gapless linear modes are doubly degenerate as shown in Fig.3.2(b). The wave function of each mode is plotted in Fig.3.3(b) and (c), and we can see that one pair of linear mode reside on the surface(Fig.3.3(b)), whereas the other pair is localized at the center plaquette(Fig.3.3(c)).

(3)*Magnetic flux of $\phi_0/2$ is homogeneously distributed on the cross sectional area.* We insert a π flux along the whole cross section of the nanowire, and the flux for each plaquette is π/N^2, and breaks TR symmetry. Thus, there is no Kramers' degeneracy in this system. However, in this case, the system is still gapless with ONE pair of linear mode, see Fig.3.4(a). The wave function plots show that the linear modes are localized at the surface of the nanowire with sharp peaks at the corners of the cross section (see Fig.3.4(b)). For surface wave functions, the enclosed flux is nearly $\phi_0/2$ and thus, time reversal symmetry is preserved approximately. It's important to note that TR is an approximate symmetry only for surface states, but not for bulk states. This approximate TR symmetry protects linear modes from backscattering to some extent and leads to nearly quantized conductance at this flux, which was also pointed out in Ref. [109].

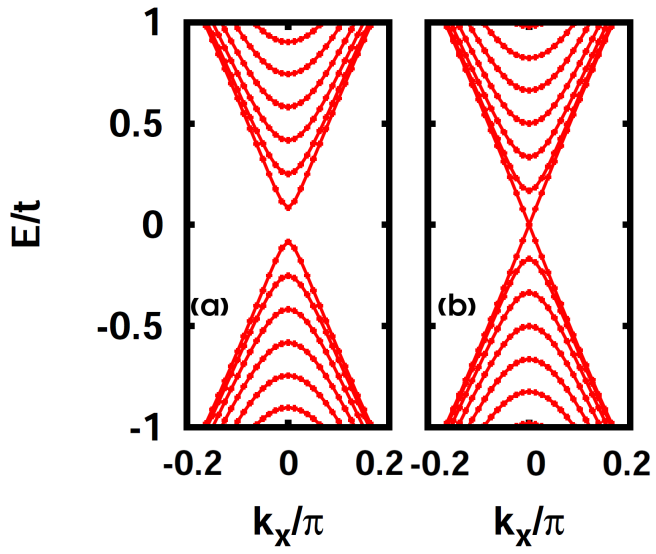

Figure 3.2. Dispersion when (a) there is no magnetic flux (b) a magnetic flux of $\phi_0/2$ is at the center plaquette.

3.1.2 Magneto-oscillation of conductance

Next, we adopt the Landauer-Buttiker formula to study two-terminal conductance of a long cuboid along the x-direction with the $N \times N$ square cross section under magnetic fields. The semi-infinite metallic leads are described by the Hamiltonian H_o (Eq.3.4). The method is described in Chapter 2.

Fig.3.5 (a) shows the surface gap oscillation in terms of magnetic flux. The gap closes at every half-integer of ϕ/ϕ_0. Accordingly, for E_f lies in the middle of the gap, the conductance follows oscillating behavior with a period of ϕ_0 as shown in Fig.3.5 (b). For a large Fermi energy, other non-topological subbands will also contribute to transport, leading to a noisy signal of conductance as given in Fig.3.6. In the section 3.3, we will show how disorder suppresses these non topological subbands.

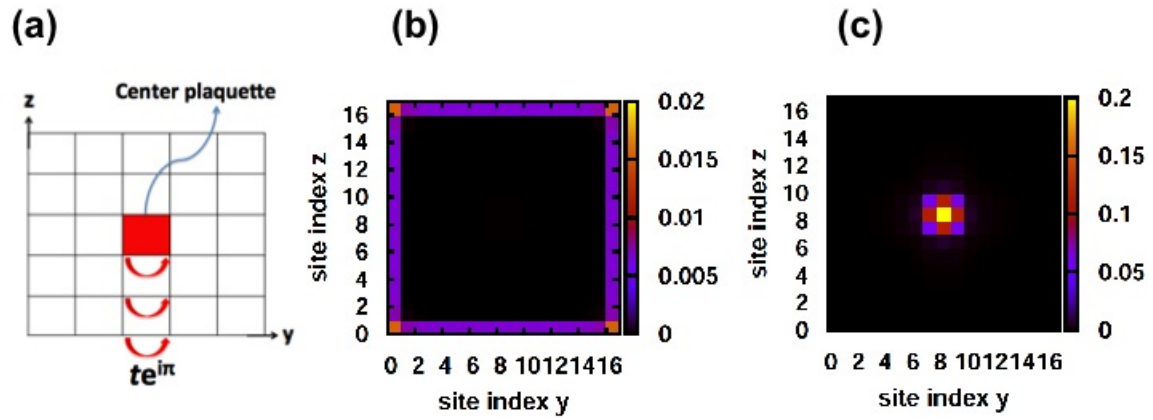

Figure 3.3. (a)Schematic plot of the hopping when the half magnetic flux quantum is at the center plaquette. (b) and (c)The wave function of the linear modes for flux $\phi_0/2$ at the center plaquette at $k = 0.02, E_f = 0.04$. The linear modes are doubly degenerate, but the wave function distributions behave very differently. One of which is localized on the surface of the nanowire(b), the other is localized at the center(c).

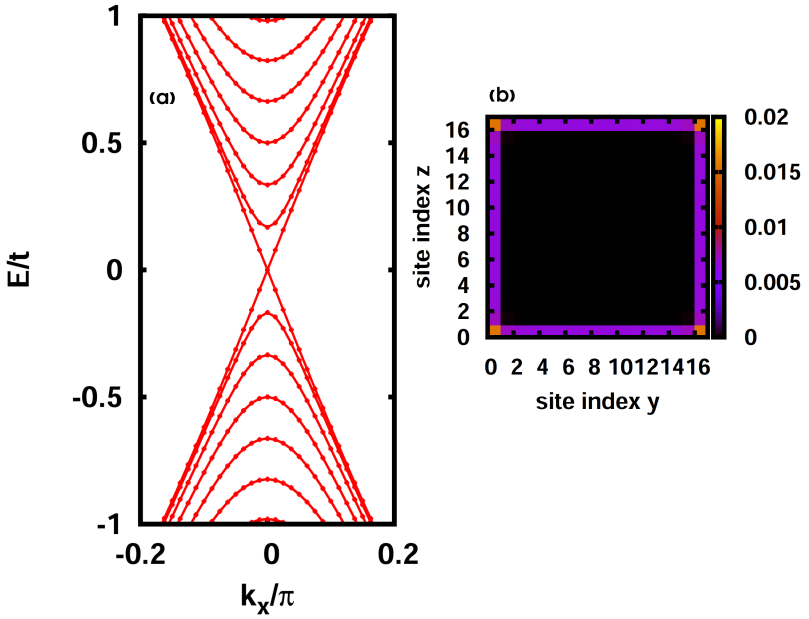

Figure 3.4. (a) dispersion when flux = $\phi_0/2$ is homogeneously distributed on the cross section. The degeneracy has been lifted due to TR breaking. (b)The wave function distribution at the flux value as (a). k=0.04 and E=0.079.

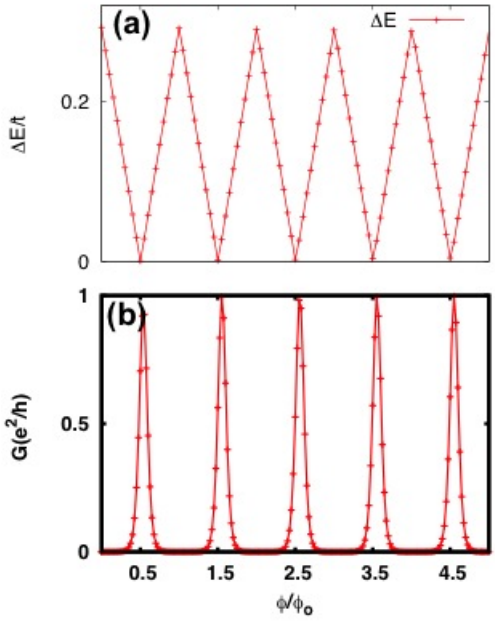

Figure 3.5. (a)The oscillations of the surface gaps. (b)Conductance oscillation when E_f lies in the middle of the gap ($E_f = 0$) in the clean limit.

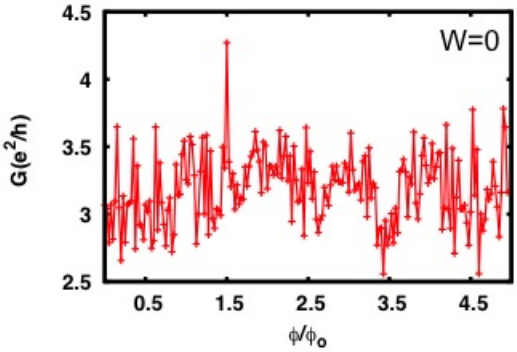

Figure 3.6. The magneto-conductance for $E_f = 0.6$ in the clean limit.

3.2 Magneto-oscillation of TI nanotube in the clean limit

Another nanostruture studied in this thesis is TI nanotube, in which there are two surfaces. Without magnetic flux, its energy dispersion is doubly degenerate

due to TR symmetry and possesses a gap as a result of π Berry phase, Fig.3.7(a). When magnetic flux is applied along the nanotube axis and homogeneously on the cross section of the nanotube, the degeneracy is lifted (see Fig.3.7(d)). When one of the surfaces encloses a half flux quantum, a pair of linear modes shows up, as shown in Fig.3.7(b) and (c). This pair of linear modes is either on the outer surface or the inner surface, depending on the value of the magnetic flux. Based on our understanding of topological states on closed surfaces discussed in the previous section, each surface contributes to a period in the oscillation of magnetoconductance for a TI nanotube. In this section, we present wave function distribution, the oscillation of the gaps, the magnetoconductance of TI nanotube and the corresponding Fourier transform in the clean limit.

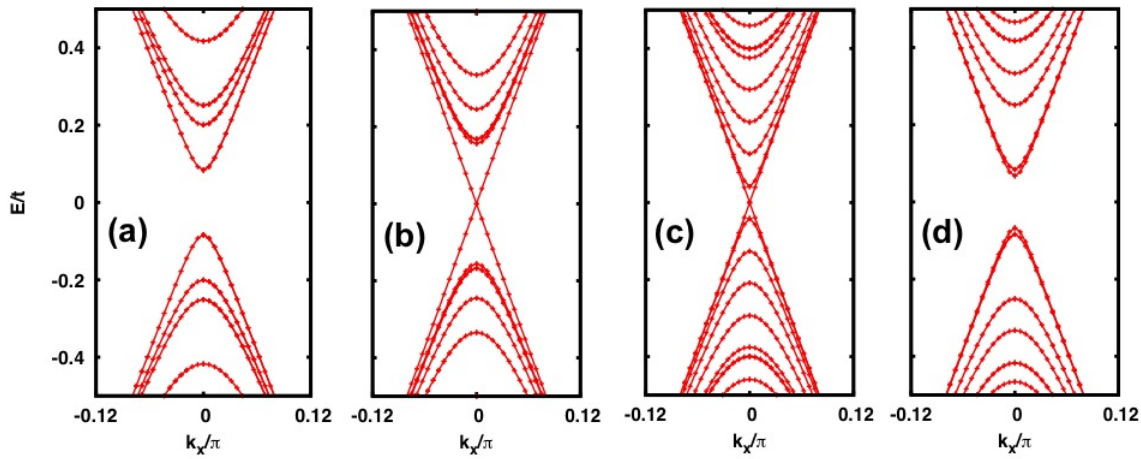

Figure 3.7. The dispersions of a TI nanotube with $N = 17, N_{in} = 6$ at $\phi = 0$(a), $\phi_0/2$(b), $2.255\phi_0$ corresponding to a half flux quantum enclosed by the inner surface state(c), $3\phi_0$(d)

The model Hamiltonian is still described by E.q.(3.3) and the geometry is as in Fig.3.1(b). The outer width is N and the inner width is N_{in}. Thus, the flux enclosed by the inner surface, denoted by ϕ_{in}, is given by $\phi \times N_{in}^2/N^2$, where ϕ is the total applied magnetic flux. However, we found that from the wave function distribution, the inner surface state usually has a thickness, which is assumed to be L_{th}, larger than one lattice constant, see Fig.3.8(b). To correctly estimate the effective magnetic flux enclosed by the inner surface state, we replace N_{in} with

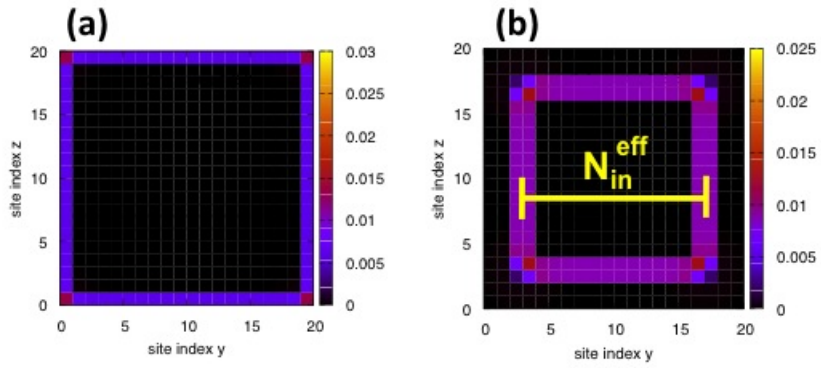

Figure 3.8. (a)The wave function distribution of the outer edge state with eigenenergy= 0. (b)The wave function distribution of the inner edge state with eigenenergy≈ 0.1. N_{in}^{eff} is depicted in the figure. $N = 20, N_{in} = 12, \phi = \phi_0/2$.

$N_{in}^{eff} = N_{in} + L_{th}$, and $\phi_{in}^{eff} = \phi \times {N_{in}^{eff}}^2/N^2$. In contrast, the outer surface state is well-localized at the outermost lattice (Fig.3.8(a)). The enclosed magnetic flux is just ϕ.

Fig.3.9 shows the oscillation of the surface gaps for the nanotube with $N = 50$ and $N_{in} = 42$. The gap closes when either ϕ/ϕ_0 or ϕ_{in}^{eff}/ϕ_0 equals to a half-integer. To calculate the effective magnetic flux for the inner surface, we have accounted for the thickness of the inner surface state, which is about two lattice constants. Thus, we obtain $\phi_{in}^{eff} = \phi * 44^2/N^2 = 0.77\phi$. Fig.3.10(a) gives the conductance for E_f in the middle of the gap in the clean limit. The conductance oscillation is complicated but shows clearly the beating feature. Thus, we perform the Fourier transform of conductance oscillation and find two peaks with the frequency ϕ_0 and $1.28\phi_0$, as shown in Fig. 3.10 (b). This corresponds to the the oscillations coming from the half flux quantum encircled by outer surface state and the inner surface state, respectively.

We have shown in this section, a pair of gapless linear modes appears when one of the surfaces of a TI nanotube encloses magnetic flux of half quantum and cancels

the π Berry phase. The transmission at $E_f = 0$ shows two oscillation periods associated with the inner and the outer surface state. The results demonstrate the potential of magnetic control of topological states in TI nanostructures.

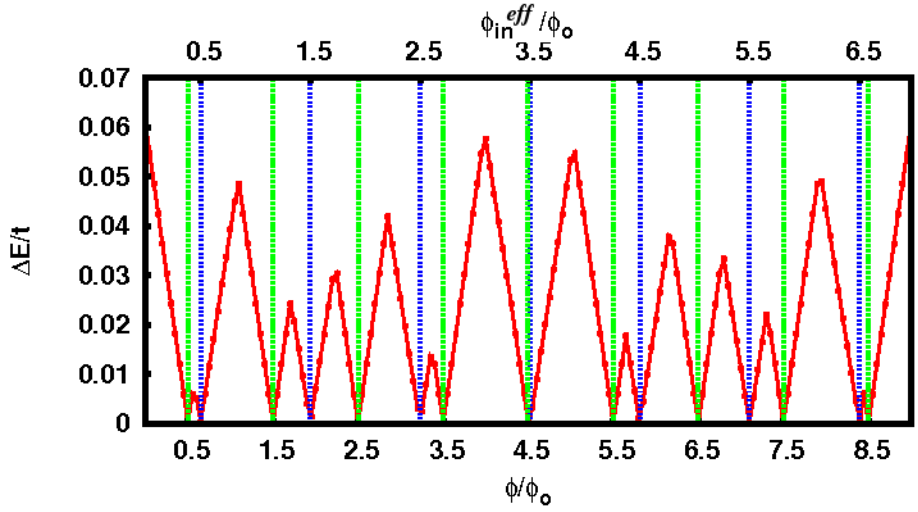

Figure 3.9. The energy gap of the surface state closes at ϕ/ϕ_0 or ϕ_{in}^{eff}/ϕ_0 is a half-integer a TI nanotube with $N = 50$, $N_{in} = 42$. The top x-axis is the effective flux enclosed by the inner surface state of the nanotube. The blue(green) dashed lines indicate the positions where ${\phi_{in}}^{eff}/\phi_0(\phi/\phi_0)$ are half-integers.

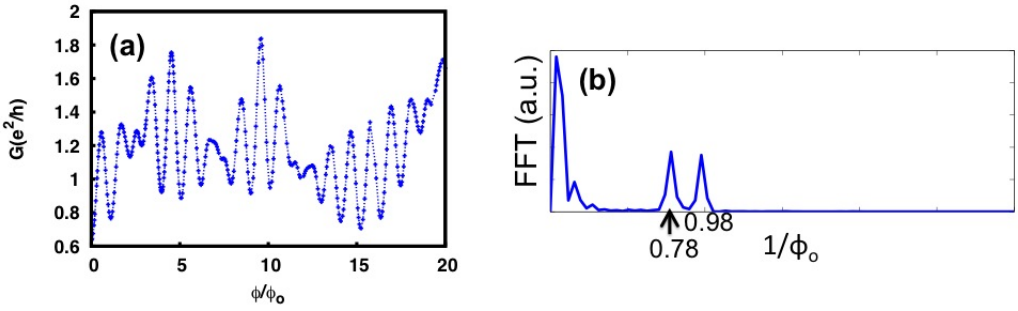

Figure 3.10. The two-terminal conductance for a TI nanotube with $N = 50$, $N_{in} = 42$ and $L = 40$. (a) The magneto-conductance. (b) The fast Fourier transform of the magneto-conductance.

3.3 Numerical simulation of conductance oscillation in disordered TI nanowire

In real experiments, bulk conduction and disorder are inevitable. In fact, our experimental collaborator has found an interesting result of magnetoconductance of nanotubes. They found that despite of low conductance, a very clear feature of oscillations is shown. The resistivity of nanotubes is in the range $6.5 - 100 m\Omega.cm$, which is at least one order of magnitude larger than all the existing experiments [23,25]. This suggests that the conduction oscillation can exist in a highly disordered and resistive topological nanostructures. Moreover, the period in unit of magnetic flux is only related to the outer diameter of nanotube, suggesting that the inner surface states do not contribute to oscillations.

Some quantum conductance oscillations have been studied extensively in normal metal rings and cylinders [110]. In the clean limit, the oscillations are due to the Aharonov-Bohm (AB) effect [111], with the oscillation period of ϕ_0. When a electron wave encircles the ring perimeter in the ballistic regime, it picks up a phase of $2\pi\phi/\phi_0$ and interferes by itself. The enclosed phase is a periodic function of the enclosed magnetic flux, thus gives rise to the period ϕ_0. While in the diffusive limit with disorder, oscillations with a period of $\phi_0/2$ arise from the Altshuler-Aronov-Spivak (AAS) effect [112], resulting from the interference between time-reversed loops of electrons. When the system becomes diffusive, in which a carrier experiences multiple scattering events while preserves its phase coherence length in transport, the interference between two time-reversed paths needs to be taken into account. The phase difference between the clockwise and the counter-clockwise paths is $2 \times 2\pi\phi/\phi_0$. Therefore, the oscillation period is $\phi_0/2$. Both kinds of oscillations require the phase coherence length to be comparable to the ring circumference.

To gain further insight into the conductance oscillation in TI nanotubes observed in experiments, we have performed extensive numerical simulations on transports in TI nanostructures. We consider a four band model on a simple cubic lattice for TIs with the Hamiltonian [108] as used in the previous sections. We also add an on-site potential whose strength is randomly distributed in the range $[-W, W]$ to

simulate disorder Hamiltonian

$$H_{dis} = \sum_i U_i C_i^\dagger C_i I. \tag{3.10}$$

To understand the behavior of surface states in extreme disorder, we consider a nanowire, rather than a nanotube. We study a nanowire with a $N \times N$ square cross section with $N = 9$ and evaluate conductance using the Landauer-Büttiker formalism combined with the iterative Green function method as a function of flux ϕ through the cross section. We find that transport behaviors are qualitatively different for integer and half-integer values of magnetic flux measured in units of flux quantum $\phi_0 = h/e$. In the clean limit, there is an energy gap for integer values of ϕ_0, and a gapless linear mode for half-integer values, as seen, for example, in Fig.3.11(a). When the Fermi level is located at a position where several other bands are occupied, the system is metallic at both integer and half integer fluxes. However, the transport of these two cases behave dramatically different when disorder is introduced. The conductance for $\phi = 0$ is dominated by non-topological carriers, while the conductance for any half-integer flux quantum is dominated by topological carriers. These two types of carriers react differently to disorder in terms of localization length, which is defined by assuming the conductance drop exponentially as $G \sim e^{-L/\lambda_{non/top}}$, where L is the length of the nanowire and $\lambda_{non/top}$ is the localization length of non-topological/topological bands. Fig.3.11(c) shows the dependence of the conductance on the length L of the system for a fixed random disorder. It clearly demonstrates two vastly different localization lengths for these two fluxes.

To further gain the insight of difference between topological and non-topological carriers, we perform a calculation for the dependence of localization length as a function of disorder strength at different magnetic flux ($\phi = 0, \phi_0/2$ and $7\phi_0/2$), as shown in Fig. 3.12/ For $\phi = \phi_0/2$ and $7\phi_0/2$, we find a peak value of localization length near $W = 2$, for which the disorder strength is half of the gap at $\phi = 0$. For $\phi = 0$, localization length monotonically decreases. At weak disorder, λ_{top} and λ_{non} are similar in magnitude, and thus both bands contribute to the transports. On the contrary, for a disorder with an intermediate strength, λ_{top} can be several magnitudes larger than λ_{non}, and thus the topological bands are dominant. When disorder strength is extremely strong, both λ_{non} and λ_{top} reduce significantly and

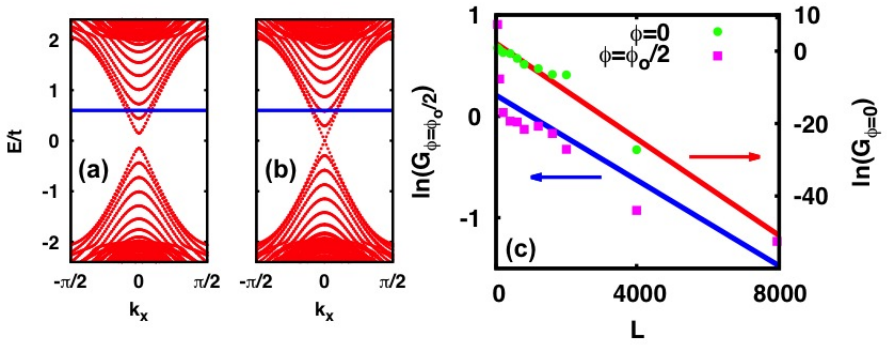

Figure 3.11. (a) and (b) Band dispersions for a disorder-free system are shown for $\phi = 0$ and $\phi = \phi_0/2$, respectively. The solid blue line marks the Fermi energy at $E_f = 0.6$, which is used for the calculations in (c) and Fig.3.17. The cross section is taken to be $9a \times 9a$ for all calculations in this section. (c) Length dependence of the conductance is shown for $\phi = 0$ and $\phi = \phi_0/2$ with $W = 2.8$ and $E_f = 0.6$. The solid lines are linear fits, from which we can extract the localization lengths to be $\lambda_{non} = 150a$ for $\phi = 0$ and $\lambda_{top} = 4800a$ for $\phi = \phi_0/2$.

when both of them are less than the nanotube length L, none of the carrier types contribute to transport. Moreover, comparing the localization length at $\phi_0/2$ and $7\phi_0/2$, the localization length is shorter when magnetic flux increases. It implies that at a higher magnetic field, the conductance maximum decreases. This behavior has been found in the numerical and experimental data which will be shown in the following discussion.

Comparing the localization length at $\phi = 0$ (λ_{non}) and $\phi_0/2$ (λ_{top}) with the length of the nanowire(L), we can find three regimes of which L lies in and the corresponding oscillation patterns. I: $\lambda_{non}, \lambda_{top} > L$ with multiple oscillation, II: $\lambda_{non} < L < \lambda_{top}$ with AB/AAS oscillation and III: $\lambda_{non}, \lambda_{top} < L$ with no oscillations. The localization lengths depends on Fermi energy E_f and disorder strength W, and thus we identify three regimes on the phase diagram explicitly for $L = 100$ (Fig. 3.13(a)) as a function of E_f and W. We will discuss the oscillation pattern in each regime shown in Fig.3.13 in the following:

In regime I, the conductance shows multiple oscillations coming from both topological and non-topological bands. Its Fourier Transform shows ϕ_0-periodicity and its higher harmonics (Fig.3.13(b) and its inset). In the weak disorder limit, surface carriers can encircle the perimeter multiple times before it leaves the

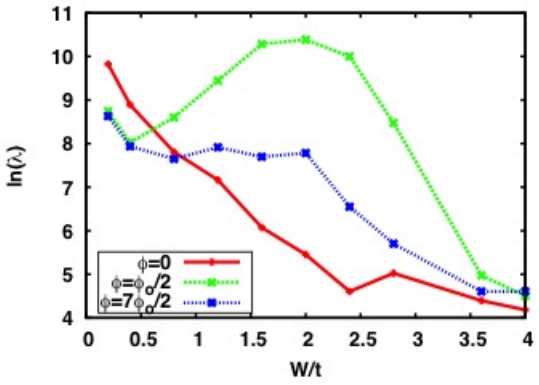

Figure 3.12. The localization length (in nature log scale) for non-topological states($\phi = 0$) and topological states ($\phi_0/2$ and $7\phi_0/2$). The disorder configuration is 100. L=800a. $E_f = 0.6$

nanowire. The phase gained by encircling the perimeter n times is $n \times (2\pi\phi/\phi_0 + \pi)$, and thus addition oscillation with the period ϕ_0/n can exist. In contrast, in the regime II, there are well-defined oscillations as shown in Fig.3.13(c), (d) and the insets. When E_f and W are chosen in the regime II, higher harmonic oscillations are suppressed and only AB-dominant oscillations are observed. This is because the scattering rate increases and consequently the probability of the surface carriers circling the perimeter more than once while maintaining phase coherence decreases. Nonetheless, in the regime II, there is not only AB oscillation, but also AAS oscillation when L is the same order as λ_{non}. Fig.3.13(d) and the inset show evidence for AAS oscillation. However, we found that AAS oscillation is gone and AB oscillation sets in when L becomes much longer than λ_{non}. Fig.3.14 gives the evolution of the oscillation with the nanowire length L. Fig.3.14(a) and its inset show a strong AAS oscillation for $L = 100$, which is the same order as λ_{non}. As L gets larger, AAS oscillation diminishes and AB oscillation becomes prominent as shown in Fig.3.14(b) and (c). It suggests that AAS is mainly from the nontopological surface states. In the regime III, the conductance is exponentially suppressed and does not show any periodic oscillations (Fig.3.13(e) and its inset). This corresponds to the strong disorder limit in which both types of carriers are localized. The phase diagram predicts that for the disorder with intermediate strength, AB oscillation dominates due to the formation of topological states when a half-integer magnetic flux quantum is inserted. Indeed, this prediction has been

observed in disordered Bi_2Te_3 nanotubes. In the following section, the relevant experimental data are presented.

3.3.1 Experimental observation of magnetoconductance in Bi_2Te_3 nanotubes and theoretical interpretation

Our theory was supported by the experiments from Prof. Qi Li's group at Penn State. The experimentalists made Bi_2Te_3 nanotubes and measured the magnetoconductance. Two nanotubes and their oscillation patterns are reported in this chapter. Both of the nanotubes show AB oscillations associated with the outer diameter. Nanotube A has an outer diameter of 125 ± 6 nm and wall thickness of 13 ± 3 nm. Nanotube B has similar wall thickness, but a slightly smaller outer diameter of 95 ± 6 nm. The magnetoconductance of the nanotube (with the smooth background subtracted) is shown in Fig.3.15 and Fig. 3.16(a) for nanotube A and B, respectively, with external magnetic field applied along the nanotube axis. Conductance oscillations are observed with a period of 3.53 ± 0.20 kOe for the nanotube A and 4.69 ± 0.25 kOe for the nanotube B. The amplitude of the oscillations decays when the magnetic field is increased, but more than 7 oscillation periods can be resolved up to 30 kOe for both nanotubes. We emphasize that the oscillations are observed only in these insulating samples but not in other more conducting samples. This is similar to the regime II in the phase diagram in which nontopological surface states are localized and transport is dominated by topological states. The angular dependence of magnetoconductance shows that the oscillation period depends solely on the parallel component of the applied field shown in Fig. 3.16(b). To our knowledge, such magnetoconductance oscillations have not been reported in any other purely insulating systems with a similar magnitude of resistance.

By extracting the area of the inserted flux that is responsible for the oscillation period, we can explore the origin of the observed oscillations. Here we take the nanotube A with a period of 3.53 ± 0.20 kOe as an example. Considering $\Delta B = ((0.5 \text{ or } 1)\phi_0)/(\pi r^2)$ where $\phi_0 = h/e$ is the flux quantum, this period corresponds to a diameter of 122 ± 1.8 nm for h/e oscillations, or a diameter of 86.5 ± 2.5 nm for $h/2e$ oscillations. The images from high-resolution field emission scanning electron microscopy on this Bi_2Te_3 nanotube show the outer diameter to

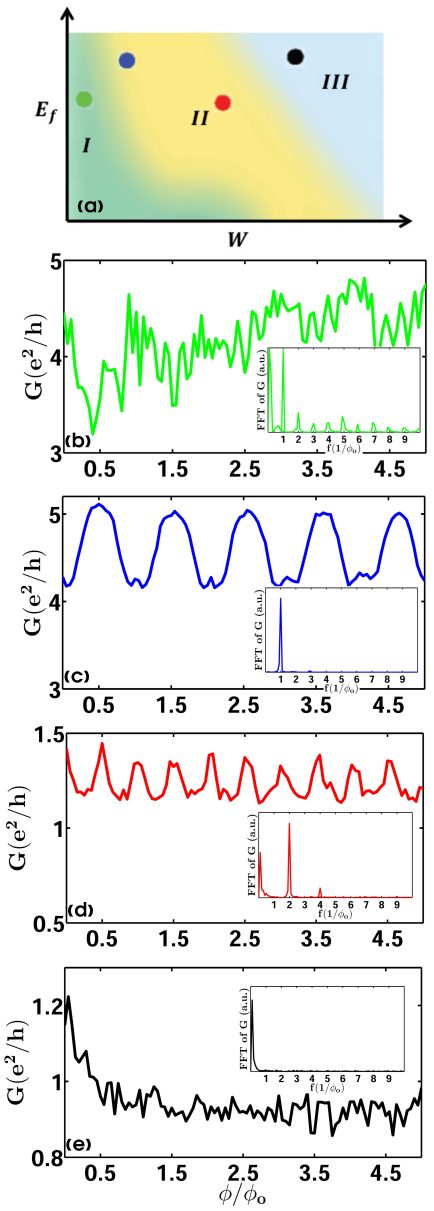

Figure 3.13. (a) The phase diagram. The length of the nanowire is 100a. The oscillation and its FFT at the representative points are shown in the lower panels with color coding. (b) AB oscillations and its higher harmonics at $W = 0.2, Ef = 0.8$ (c) AB oscillation at W=0.8, Ef =1.3 (d) AAS oscillation at $W = 2.4, Ef = 0.8$ (e) no oscillation at $W = 3.6, Ef = 1.3$.

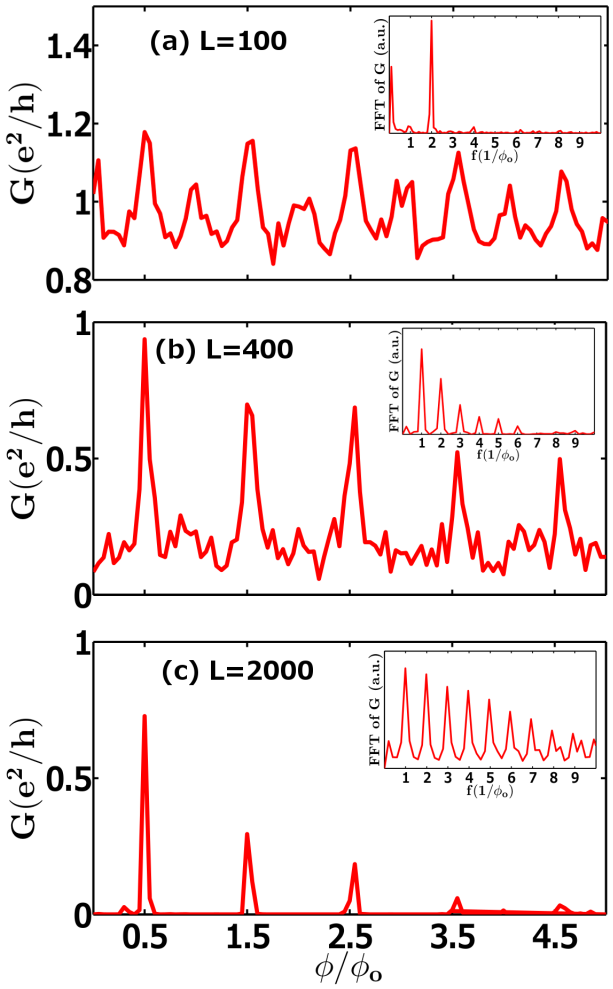

Figure 3.14. The oscillation and the corresponding FFT at various nanowire length: L=100(a), 400(b), 2000(c) with disorder strength $W = 2.8$ and $E_f = 0.6$.

be 125 ± 6 nm, suggesting that the observed oscillations are consistent with the h/e oscillations associated with the outer surface of the nanotube.

An interpretation of the main oscillations in terms of the AAS $h/2e$ oscillations may be ruled out because the corresponding area is much smaller than the cross-sectional areas of either the outer or the inner surface. Besides the main oscillation period, there are also smaller conductance peaks observed in the data. These peaks may come from AAS oscillation of the outer surface. However, because we cannot determine the period of the smaller peaks, we cannot determine whether the AAS oscillation are also presence. Normal AB oscillations from bulk carriers

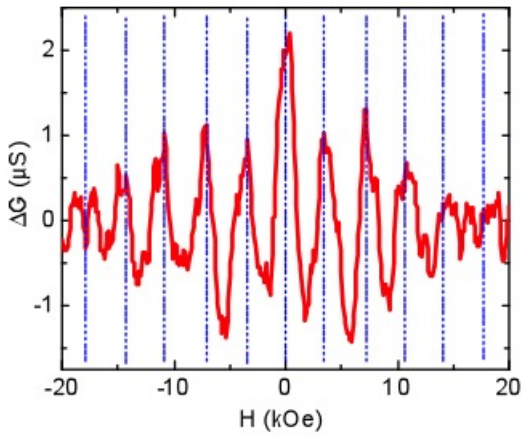

Figure 3.15. Magneto-conductance oscillations of Device A (background subtracted). Magnetic field is applied parallel to the nanotube axis (current flow direction). The observed period is 3.53 ± 0.20 kOe. This period is consistent with h/e oscillations associated with the outer surface of the nanotube which has diameter of 125 ± 6 nm.

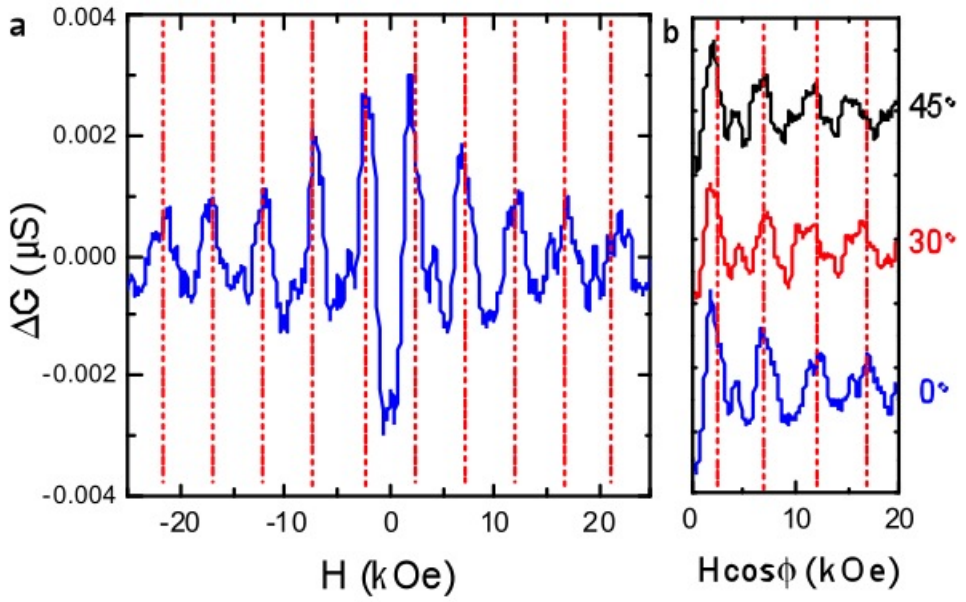

Figure 3.16. Magneto-conductance oscillations on Device B (background subtracted). (a) Conductance oscillations for Device B. The oscillations show an h/e period associated with the outer surface of the nanotube. (b) Conductance oscillations for different field directions, plotted as a function of parallel component of applied field. Evidently, the period depends solely on the parallel component of applied field.

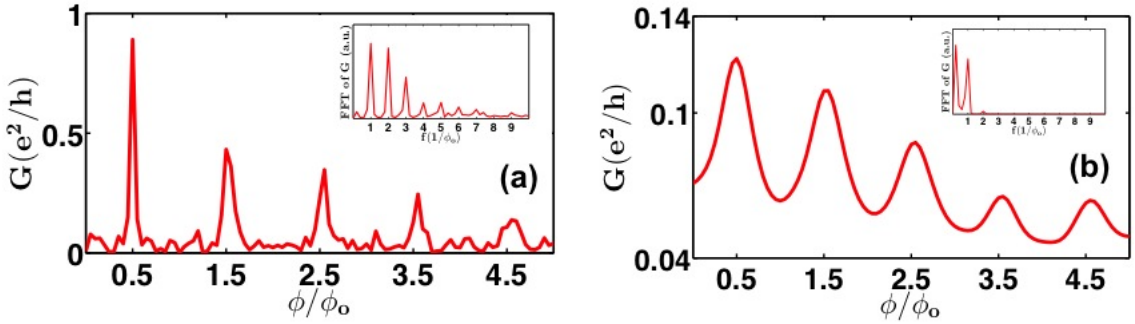

Figure 3.17. (a) The magneto-conductance oscillations as a function of magnetic flux ϕ in the regime II for $W = 2.8, L = 800a$ and $E_f = 0.6$. (b) The magneto-conductance oscillations for a system with variations in the cross sectional area along the length of the nanotube with $\Gamma = 0.4$. The cross section is taken to be $9a \times 9a$ for all calculations.

are also unlikely to be a cause of the observed oscillations, because the bulk is highly resistive with a short bulk localization length $\sim$ 10nm, which is much shorter than the inner and outer perimeters of the nanotube. Finally, the inner diameter is estimated to be 100 ± 6 nm for Nanotube A and the corresponding oscillation period is approximately 5.28 ± 1.26 kOe. From our data, we cannot clearly resolve oscillations with this period. It is tempting to attribute some smaller peaks in the conductance oscillations in Fig. 3.15 and 3.16(a) to the inner surface, but the signal is much weaker than the principal oscillations. This could be due to the relatively larger roughness of the inner surface of the nanotubes, as expected from the outward diffusion growth process. The detailed analysis based on the oscillation period thus supports the origin of main peaks in conductance oscillations from the anomalous AB oscillation from the outer surface of the nanotube.

As shown in Fig. 3.17(a), the sharp peaks for the magnetic flux $\phi = (n + 1/2)\phi_0$ indicate that only gapless topological surface modes contribute to transports in the regime II in Fig.3.13(a). This behavior is consistent with the experimental observation that the conductance oscillations do not appear in metallic samples, but only in insulating samples in which non-topological states are localized and transport is dominated by Dirac surface states. The peaks observed in experiments are not as sharp as those in our calculations. We believe the rounding arises from variation in the experimental sample of the cross-sectional area along the length of the nanotube, which translates into a distribution for the enclosed magnetic

flux. We model the fluctuations in the magnetic flux with a Lorenzian distribution $L_\phi(\xi) = \frac{1}{\pi}\frac{\Gamma}{\Gamma^2+(\xi-\phi)^2}$ where Γ, ϕ is the average magnetic flux and ξ is the variable flux. The average conductance obtained with $\bar{G}(\phi) = \int_0^{5\phi_0} d\xi L_\phi(\xi)G(\xi)d\xi$, with $\phi = 0.5\phi_0$ is shown in Fig. 3.17(b), and qualitatively resembles the experimental behavior. If the variations of the cross section are sufficiently large, they can suppress the oscillations altogether, which we believe to be the case with the oscillations associated with the topological states at the inner surface of the nanotube. In the regime II where the surface state dominates transport, we expect a conductance minimum at $\phi = 0$, which we have confirmed in our simulations. In the regime I, the situation is more complex, and whether the conductance shows a minimum or a maximum at zero field depends on parameters such as Fermi levels and disorder strengths [113]. Experimentally, the nanotube B with a lower conductance indeed shows a conductance minimum at $\phi = 0$(Fig. 3.16a), consistent with our expectation. In contrast, the nanotube A shows a conductance maximum (Fig.3.15), which suggests that it lies close to the boundary between the regime I and II.

Moreover, we compared the decrease of the oscillation amplitude of the numerical and experimental results as shown in Fig.3.18. The experimental result is without subtracting background signal. Both data show qualitatively the same behavior: the overall conductance and the amplitude decrease as magnetic flux increases. It is because the localization length decreases at higher magnetic flux (Fig.3.12), leading to the reduction of maximum conductance at half-integer flux quanta (Fig.3.17(a)) and the reduction of overall conductance of the averaged conductance.

3.4 Conclusions

In summary, the robustness of surface states of TI nanostructures inserted with magnetic flux are studied numerically. Topological surface states arise at magnetic flux of half-integer in unit of magnetic flux quantum. The conductances at these values of magnetic flux prevail over disorder. Nontopological states are shown to have shorter localization length in the regimes of intermediate disorder strength and thus easier to be localized by disorder when the sample size is larger than their localization length. Moreover, our experiment collaborators have studied Bi_2Te_3 nanotubes with sufficiently strong disorder that freezes out bulk conduction. The observed quantum oscillations in magnetoconductances with a period ϕ_0 that can be

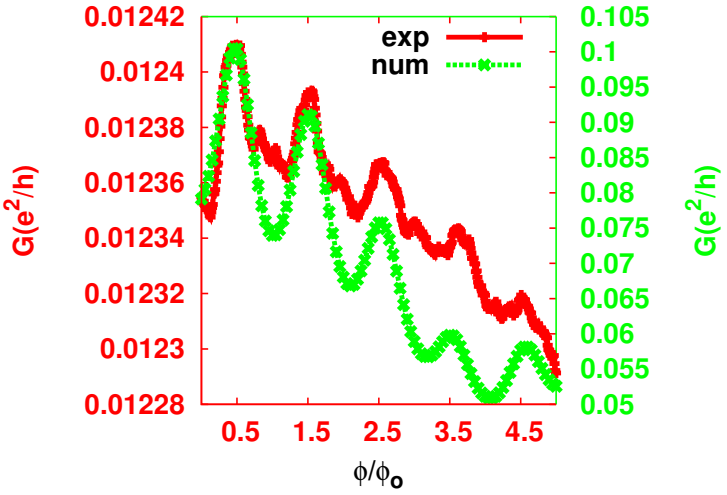

Figure 3.18. Comparison between numerical and experimental magnetoconductance without subtracting the background. For numerical calculation, the parameters are $W = 2.8, E_f = 0.6, \Gamma = 0.8$.

attributed to the outer surface states. The numerical results verify a fundamental aspect of the three-dimensional topological insulators, namely that the surface states are robust against strong disorder, which is supported by magneto-transport measurement in TI nanotubes.

Chapter 4
Quantum anomalous Hall effect in Mn doped HgTe quantum wells

The QAH effect has been the long-sought-after family member of the quantized Hall family, in which QH and QSH effects has been experimentally verified in 1980 [5] and 2007 [18], respectively. Only until recently that the QAH effect has been realized in magnetic doped TIs [59] . The theoretical predictions, which was followed by experimental realization, of the quantized Hall conductance induced by the exchange coupling between magnetic moments and electron spins [50] opened the door to the realization of this effect in magnetic materials. Among several proposals [31, 114–116], Mn doped HgTe quantum wells [30] was one of the earliest proposals for realizing the QAH effect. However, this material is paramagnetic and an out-of-plane magnetic field is needed to induce magnetization. Topologically, the QAH state can be adiabatically connected to the QH state, so it is not easy to distinguish them when the out-of-plane magnetic field coexists with the magnetization. This study aims in proposing experimentally feasible approaches for observation of the QAH effect without the coexistence of QH effect in HgMnTe quantum wells. In this chapter, detailed theoretical studies and proposed experiment setup are reported. The remainder of the chapter follows closely Ref. [117] and [118].

4.1 Model Hamiltonian for $Hg_xMn_{1-x}Te$ quantum wells

In this section, we first introduce our model Hamiltonian for the Mn-doped HgTe quantum wells. The effective Hamiltonian is written in the basis of $|E1+\rangle, |H1+\rangle, |E1-\rangle, |H1-\rangle$, with E1 and H1 denote electron and heavy hole sub-bands and $\pm$ for opposite spin states. The form of the effective Hamiltonian is given by [52]

$$\begin{aligned} H &= \epsilon(\mathbf{k}) + H_{BHZ} + H_m \\ \epsilon(\mathbf{k}) &= C - Dk^2, \end{aligned} \tag{4.1}$$

where H_{BHZ} is given by the continuum limit of E.q. (1.18) and $\epsilon(\mathbf{k})$ is introduced to break the particle-hole symmetry, while preserving the topology of the Hamiltonian. We denote the growth direction as the z-direction and the quantum well plane as xy plane. The parameters m, B, A, C, D in the Hamiltonian depend on the material details and can be found in Ref. [119, 120]. H_m describes the spin splitting of electron and hole sub-bands and its form is given by

$$H_m = \mathbf{g}_1 \cdot \vec{\sigma}\tau_0 + \mathbf{g}_2 \cdot \vec{\sigma}\tau_z, \tag{4.2}$$

, where $\mathbf{g}_1 = \frac{1}{2}(\mathbf{g}_e + \mathbf{g}_h)$ and $\mathbf{g}_2 = \frac{1}{2}(\mathbf{g}_e - \mathbf{g}_h)$. Here the vectors $\mathbf{g}_e$ ($\mathbf{g}_h$) couples to electron (hole) spin and describe spin splitting for the E1 (H1) sub-bands for magnetic fields along different directions. There are two types of contribution for spin splitting, one from Zeeman coupling of magnetic fields and the other from exchange coupling to Mn doping, so the form of spin splitting is given by [30, 91]

$$g_{e(h)i} = g^{zm}_{e(h)i}\mathcal{B}_i + g^{exc}_{e(h)i}, \quad i = x, y, z. \tag{4.3}$$

The first term gives the Zeeman coupling with g-factor $g^{zm}_{e(h)i}$ and magnetic field $\mathcal{B}_i$, while the second term describes exchange coupling to Mn doping, given by

$$g^{exc}_{e(h)i} = \tilde{g}_{e(h)i}\langle S\rangle_i, \quad i = x, y, z \tag{4.4}$$

$$\langle \boldsymbol{S}\rangle = -\hat{\boldsymbol{e}}S_0 B_{5/2}\left(\frac{5g_{Mn}\mu_B B}{2k_B(T+T_0)}\right), \tag{4.5}$$

where $\tilde{g}_{e(h)i}$ is the coupling constant between electron (hole) band and Mn spin S. Eq.(4.5) is the mean field approximation of Mn magnetization and $\hat{\boldsymbol{e}}$ denotes the direction of magnetic field, $S_0 = 5/2$ is the Mn spin, $g_{Mn} = 2$ is the g-factor of Mn , $T_0 \approx 2.6K$ is to rescale the temperature to take into account antiferromagnetic interaction between Mn ions [121] and $B_{5/2}$ is the Brillouin function. In spin splitting (E.q.(4.3)), Zeeman terms depends linearly on magnetic fields while exchange coupling has a complicated non-linear dependence. Due to the quantum wells configuration, the g-factors $g^{zm}_{e(h)i}$ and $\tilde{g}^{exc}_{e(h)i}$ for spin splitting are assumed to be isotropic in the xy plane, but different for the z direction. Without loss of generality, we only consider the x direction for in-plane magnetic fields below. The parameters of the Hamiltonian (E.q.(4.2)) can be found in Ref. [30, 119]. In the realistic systems, in-plane spin splitting for heavy hole sub-bands depends on the cubic order of magnetic field $\mathcal{B}$ and magnetic moments S [118], which is neglected in the following ($\tilde{g}_{hx} = \tilde{g}_{hy} = g^{zm}_{hx} = g^{zm}_{hy} = 0$).

The QAH effect in HgMnTe quantum wells with only z-direction magnetization has been investigated in Ref. [30]. For zero in-plane magnetic field, it has been shown that the QAH phase can be realized in the regime $g_{ez}g_{hz} < 0$ and $|g_{2z}| > |m|$, while it is a normal insulator when $|g_{2z}| < |m|$ (g_{1z} does not change the topology because it only shifts the band edge, but does not cause band inversion). Since the quantized Hall conductance can only be changed when the bulk band gap is closed, two phases will share the same Hall conductance if they can be adiabatically connected without closing band gap. Therefore, one can identify the Hall conductance in a finite in-plane magnetic field by adiabatically connecting to the regime with zero in-plane magnetic field.

To understand the normal-QAH transition in the presence of in-plane magnetization, we first consider the case with either $\mathbf{g_1} = 0$ or $\mathbf{g_2} = 0$, in which the Hamiltonian can be solved analytically. In both cases, the results are qualitatively the same. Here, we show the result of $\mathbf{g_1} = 0$. After diagonalization, the dispersion is

$$E_{s,t} = s\sqrt{A^2k^2 + M^2 + g^2 + t2\sqrt{2A^2k_x^2g_{2x}^2 + M^2g^2}} \tag{4.6}$$

where $s, t = \pm$, $k^2 = k_x^2 + k_y^2$, and $g^2 = g_{2x}^2 + g_{2z}^2$ is the strength of spin splitting. The energy gap is given by $E_{+-} - E_{--} = 2\sqrt{A^2k^2 + M^2 + g^2 - 2\sqrt{2A^2k_x^2g_{2x}^2 + M^2g^2}}$,

which vanishes under the condition

$$[A^2k^2 + M^2 - g^2]^2 + 4A^2g_{2z}^2k^2 + 4A^2g_{2x}^2k_y^2 = 0. \tag{4.7}$$

This equation can be simplified as $g^2 = m^2$ or $g_{2x}^2 = A^2 + (m - Bk^2)^2 > m^2$ at $g_{2z} = 0$. The gap-closing lines in terms of g_{2x} and g_{2z} are shown in Fig.4.1, separating three insulating phases. When $|g| > |m|$ and $g_{2z} \neq 0$, the system always stays in the QAH phase, regardless of the magnetization direction. The Hall conductances for positive and negative $\mathcal{B}_z$ have opposite signs [30], which are separated by the metallic lines along $g_{2z} = 0$ and $|g| > |m|$. In the following sections, we will present the phase diagrams with more realistic parameters in different conditions.

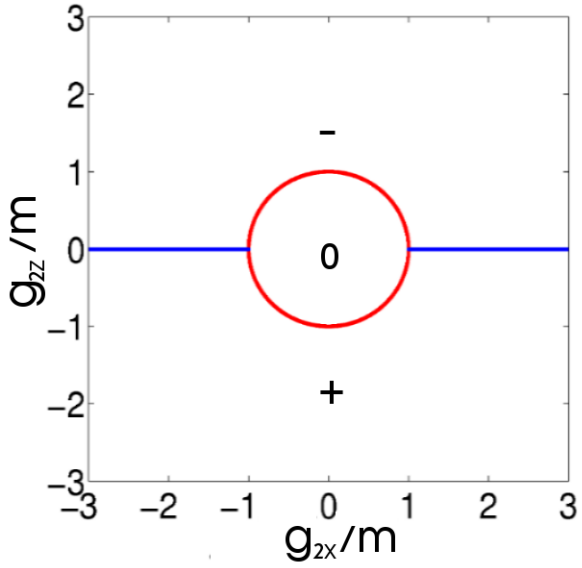

Figure 4.1. The phase diagram obtained from analytical calculation where $g_{ex} = \pm g_{hx}$.

4.2 The effect of exchange coupling

We first neglect the Zeeman coupling and study the behavior of the system when only exchange coupling is taken into account. Without Zeeman coupling, the spin splitting is determined by Mn magnetization, which will saturate after magnetic field achieves a certain value, as shown in Eq.4.5 and Fig.4.3(c). Because spin-

splitting saturates and the coupling constants are anisotropic, there exists a critical angle beyond which the QAH state no longer exists. Following the derivation of the gap-closing condition in the previous section, we first analytically solve for the critical angle with $\mathbf{g}_1 = 0$. The spin-splitting is $g^2 = g_{2x}^2 + g_{2z}^2$ with g_{2x} and g_{2z} given by E.qs.(4.3) - (4.5)

$$\begin{aligned} g_{2i} &= \frac{1}{2}(g_{ei}^{exc} - g_{hi}^{exc}) \\ &= \tilde{g}_{2i}\langle S\rangle_i, \end{aligned} \tag{4.8}$$

where $\tilde{g}_{2i} = \frac{1}{2}(\tilde{g}_{ei} - \tilde{g}_{hi})$. The x(z)- components of Mn magnetization is $\langle S\rangle_{x(z)} = -\langle S\rangle \sin\theta(\cos\theta)$, where θ is defined as between magnetization and z-axis as depicted in Fig.4.2 and $\langle S\rangle$ is given by E.q.(4.5). When magnetization saturates, $\langle S\rangle$ reaches its maximum value, S_0. Thus, the saturated spin-splitting is $g^2 = (\tilde{g}_{2z}S_0\cos\theta_c)^2 + (\tilde{g}_{2x}S_0\sin\theta_c)^2$. From the analytical solution in the previous section, the gap-closing condition is $g^2 = m^2$. Thus, the critical angle is determined by $m^2 = (\tilde{g}_{2z}S_0\cos\theta_c)^2 + (\tilde{g}_{2x}S_0\sin\theta_c)^2$. It suggests that if $|\tilde{g}_{2x}S_0| < |m|$, θ_c never reaches $\pi/2$ and an out-of-plane magnetization is necessary to achieve the transition.

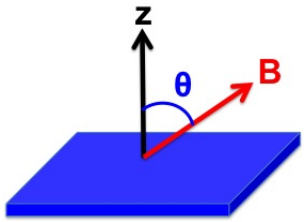

Figure 4.2. θ is defined as the angle between magnetic field and z-axis.

For more realistic parameters, we perform a numerical calculation of energy gap as a function of $\mathcal{B}_x$ and $\mathcal{B}_z$, from which one can determine phase diagram, as shown in Fig. 4.3 (a), by the adiabatic continuity argument. Here the dependence of magnetization on magnetic field is determined by Eq. (4.5). We choose $\tilde{g}_{ex} = 1meV, \tilde{g}_{hx} = 0$ (all the other parameters are given in the caption), such that the maximum in-plane exchange coupling for the electron subband $\tilde{g}_{ex}S_0$ is smaller than $|m|$. We find that with increasing $\mathcal{B}_x$, the critical z-direction magnetic field keeps increasing. Fig. 4.3(b) is the phase diagram in terms of the spin splitting. Along $g_{ex} = 0$, the gap closes at $|g_{2z}| = |m|$ which agrees with the previous study [30].

The maximum in-plane spin splitting for electron is $|\tilde{g}_{ex}S_0| = 0.8m$, which is smaller than m. According to the analytic discussion in the previous paragraph, gap does not close when there is only in-plane spin splitting in this case. The critical angle of the magnetic field is given in Fig.4.3(d), it reaches 0.44π after the magnetization saturates for the current parameters.

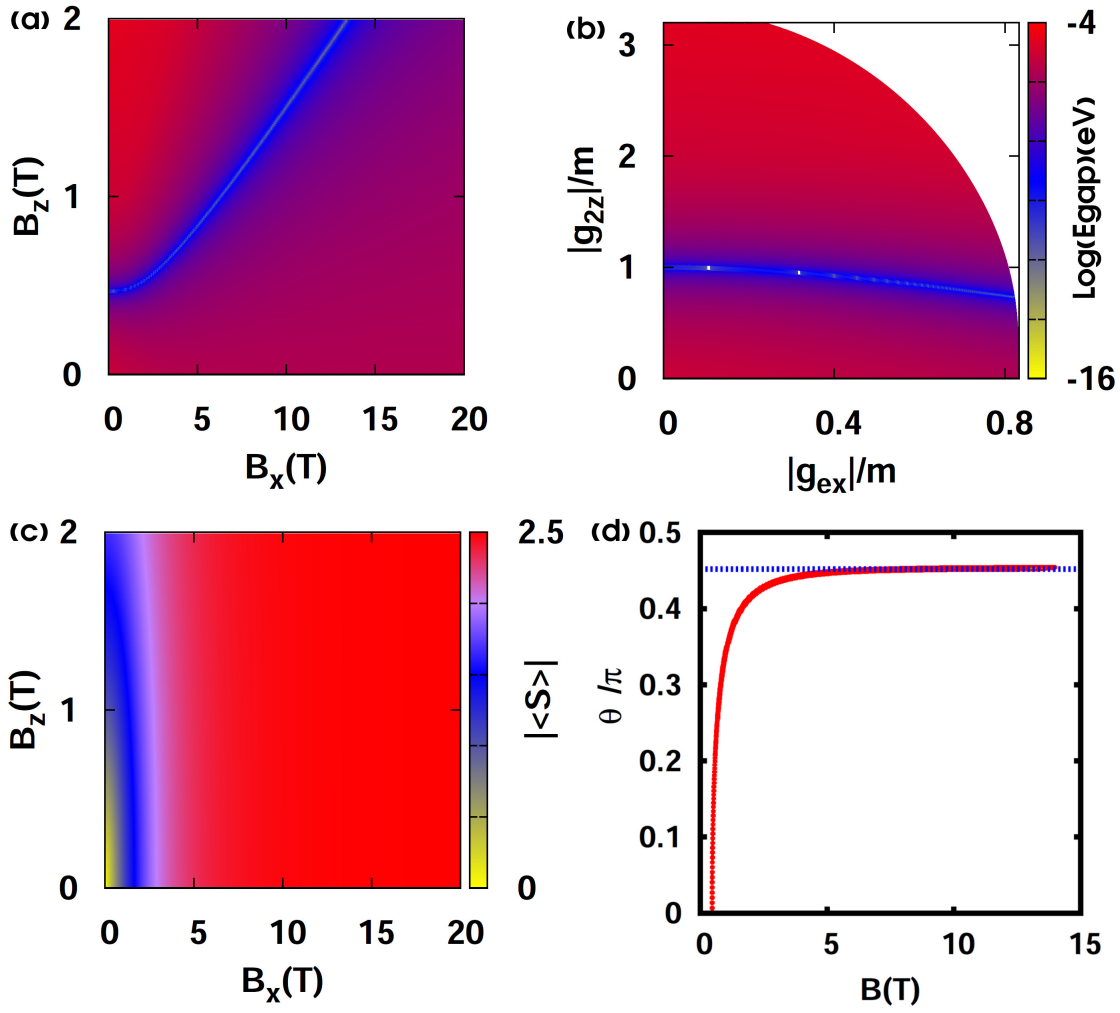

Figure 4.3. The phase diagram at 1K for the Hamiltonian without Zeeman coupling. (a) Phase diagram in terms of the magnetic field. (b) Phase diagram in terms of the strength of spin splitting. The y-axis is only g_{2z} because only this term contributes to gap closing. (c)Magnetization of the Mn atoms under the same range of magnetic fields in (a). It saturates at 2.5. (d) The critical angle of magnetic field for metallic lines. The parameters used for are $\tilde{g}_{ex} = -1meV, g_{hx} = 0, \tilde{g}_{ez} = -3meV, \tilde{g}_{hz} = 9meV, A = 0.38eV/nm, B = 0.85eV/nm^2, D = 0.67eV/nm^2, m = 3meV$.

Next, we compare the phase boundary for different values of $\tilde{g}_{ex}$ as shown in Fig.4.4(a). The spin-splitting for hole band $\tilde{g}_{hx}$ is taken to be zero. The critical $\mathcal{B}_z$ increases faster for smaller $\tilde{g}_{ex}$. The critical angle of the magnetic field for each value of $\tilde{g}_{ex}$ is given in Fig.4.4(b).

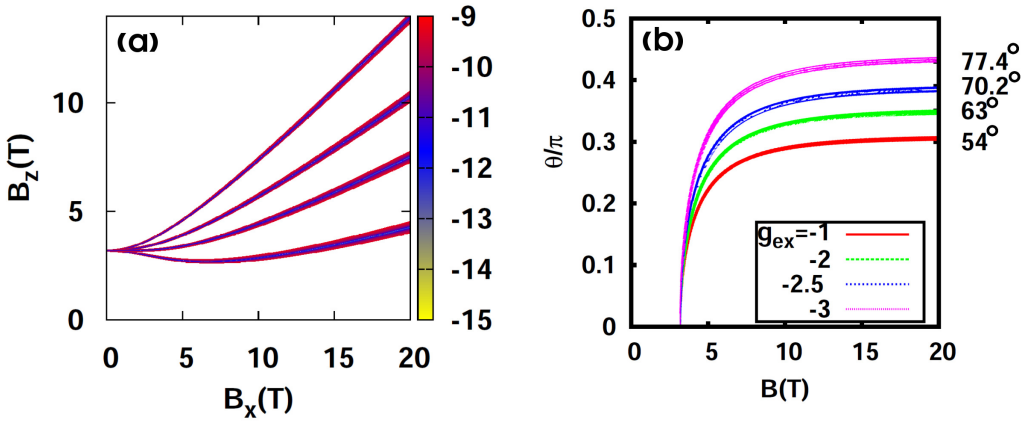

Figure 4.4. (a)The phase boundary for different values of $\tilde{g}_{ex}$ at T=4.2K. From top to bottom, the values are $-1, -2, -2.5, -3$meV. (b) Critical angle of magnetic field of the phase boundary for different values of $\tilde{g}_{ex}$ at T=4.2K. The values are given in the legend with the unit of meV . The right vertical axis gives the critical angle in degrees. For both (a) and (b), the parameters are $g_{hx} = 0, \tilde{g}_{ez} = -3meV, \tilde{g}_{hz} = 3meV, A = 0.38eV/nm, B = 0.85eV/nm^2, D = 0.67eV/nm^2, m = 4.5meV$.

From the phase diagram based on the numerical calculation, we conclude that when the in-plane spin splitting for the hole band and Zeeman coupling are negligible, the magnetic field reaches a critical angle less than $\pi/2$ for gap-closing. The critical angle depends on the in-plane g-factor for electron band and becomes larger when $\tilde{g}_{ex}$ gets larger. All these predictions can be examined experimentally in Mn doped HgTe quantum wells with rotating magnetic fields.

4.3 The interplay between exchange coupling and Zeeman coupling: the reentrant QAH effect

The above section has neglected Zeeman coupling ($g^{zm}_{e(h)} = 0$), and obtained a critical magnetic field beyond which no quantized Hall conductance will be observed. In this section, we will investigate how Zeeman coupling change this picture. In particular,

we predict a reentrant behavior of the QAH effect due to the competition between Zeeman coupling and exchange coupling.

Similar to what we did in the last section, we also plot the energy gap for the Hamiltonian (4.1) in Fig. 4.5(c) for $\mathcal{B}_x$ and $\mathcal{B}_z$ with the realistic parameters taken from Ref. [119] for HgMnTe quantum wells. The phase diagram is separated into three insulating regimes by metallic lines, as depicted by the black lines in Fig. 4.5(c). For $\mathcal{B}_x = 0$, the Hall conductance is known [30] to be $\pm\frac{e^2}{h}$ when $|\mathcal{B}_z|$ is larger than a critical value $|\mathcal{B}_{zc}|$ and zero when $|\mathcal{B}_z| < \mathcal{B}_{zc}$. Therefore, the Hall conductance of each insulating regime can be identified by adiabatic connection, as shown in Fig.4.5(c). We find that with increasing $\mathcal{B}_x$, the critical z-direction magnetic field, as depicted by the metallic lines, first increases and then drops down to zero. For a fixed small $\mathcal{B}_z$ (the line $\mathcal{B}_z = 0.2T$ in Fig.4.5(c)), the system is driven from a normal insulator to a QAH insulator with Hall conductance $-e^2/h$ by increasing $\mathcal{B}_x$. More interestingly, when $\mathcal{B}_z = 0.6T$, the Hall conductance σ_{xy} undergoes the transitions from $-e^2/h$ to 0 to $-e^2/h$, showing a reentrant behavior for the QAH effect. This behavior is merely due to Zeeman coupling and exchange coupling rather than orbital effect since Landau levels are not considered in this calculation. In the following, we will discuss the physical picture of reentrant behavior of the QAH effect due to in-plane magnetic fields.

The analytic model in the section 4.1 suggests that the key factor for the normal insulator-QAH insulator transition is the strength of spin splitting $|g|$, instead of the direction of magnetic fields or magnetization. The magnetization direction does not have to be out-of-plane for the QAH effect to arise. For $\mathcal{B}_z = 0.2T$, the spin splitting induced by z-direction magnetic field is not strong enough to induce the QAH state. With increasing the in-plane magnetic field, the total spin splitting is significantly enhanced, leading to the transition from the normal insulator to the QAH insulator at $\mathcal{B}_x = 9.5T$, which is consistent with the above analytical solution. The reentrant behavior at $\mathcal{B}_z = 0.6T$ results from the competition between the exchange coupling of magnetic moments and the direct Zeeman coupling of magnetic fields. For a small in-plane magnetic field $\mathcal{B}_x$, the exchange coupling is much stronger than the direct Zeeman coupling. So the spin splitting $\mathbf{g}_{e(h)}$ is dominated by the exchang term $\mathbf{g}^{exc}_{e(h)}$ and the direct Zeeman coupling part can be neglected. From the Kane model calculation, it turns out that the coupling constant of exchange coupling is strongly anisotropic [119, 120], and the z-direction

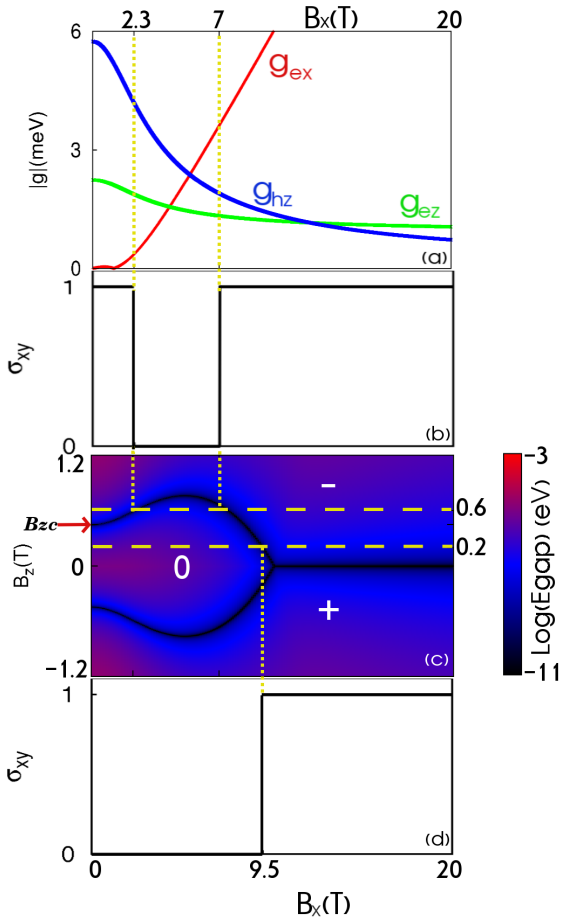

Figure 4.5. (a)The effective spin splitting as a function of B_x at a fixed $\mathcal{B}_z$=0.6T. (b) The schematic plot of the Hall conductance in the unit of e^2/h as a function of the $\mathcal{B}_x$ for the indicated $\mathcal{B}_z$=0.6T . (c)The phase diagram at 1K. The diagram is on a logarithmic scale to enhance the contrast. The black lines indicate the phase boundaries of different topologies. (d)The schematic plot of the Hall conductance in the unit of e^2/h as a function of the $\mathcal{B}_x$ for the indicated $\mathcal{B}_z$=0.2T. The parameters used for Fig. (a) and (c) are $\tilde{g}_{ex} = -0.84meV, g_{ex}^{zm} = -0.8meV/T, g_{hx} = 0, \tilde{g}_{ez} = -2.13meV, g_{ez}^{zm} = 1.5meV/T, \tilde{g}_{hz} = 9meV, g_{hz}^{zm} = -0.08meV/T, A = 0.38eV/nm, B = 0.85eV/nm^2, D = 0.67eV/nm^2, m = 3meV$.

coupling is much stronger than the in-plane coupling. Consequently, when magnetic moments of Mn atoms are tilted into the x-direction due to the increase of $\mathcal{B}_x$, spin splitting is reduced significantly, leading to the transition from the QAH phase to the normal insulating phase. With further increasing in-plane magnetic field, the direct Zeeman term, which grows linearly with $\mathcal{B}_x$, is eventually dominant over the exchange term, which saturates at high magnetic fields. Thus, the system is

driven back to the QAH phase. To verify this physical picture, we plot the spin splitting of E1 and H1 sub-bands as a function of $\mathcal{B}_x$ in Fig.4.5(a). The green and blue curves show the rapid reduction of the z-direction spin splitting of E1 and H1 sub-bands respectively, as $\mathcal{B}_x$ increases. As a result, it leads to the transition from a QAH state to a normal insulating state at $\mathcal{B}_x \approx 2.3T$. The red curve shows the growth of x-direction spin splitting and it eventually leads to the transition from normal insulating to QAH phase at $\mathcal{B}_x = 7T$. We would like to emphasize that the reentrant behavior is unique for the HgTe quantum wells with Mn doping. Without Mn doping, there is no exchange coupling to magnetic moments and consequently, we only find the transition from the normal insulator to the QH insulator regime, which is shown in Fig 4.6.

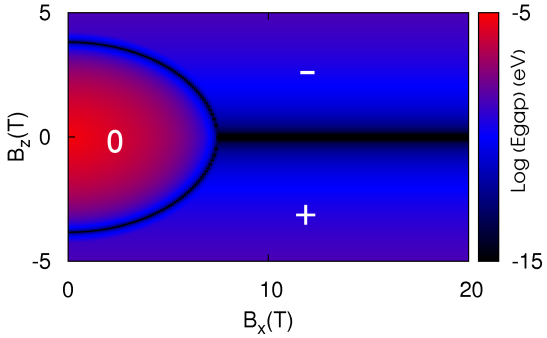

Figure 4.6. The phase diagram at 1K for the Hamiltonian without the exchange coupling. The diagram is on a logarithmic scale to enhance the contrast. The black lines indicate the phase boundaries of different topologies. The parameters used are $\tilde{g}_{ex} = 0meV, g_{ex}^{zm} = -0.8meV/T, g_{hx} = 0, \tilde{g}_{ez} = 0meV, g_{ez}^{zm} = 1.5meV/T, \tilde{g}_{hz} = 0meV, g_{hz}^{zm} = -0.08meV/T, A = 0.38eV/nm, B = 0.85eV/nm^2, D = 0.67eV/nm^2, m = 3meV$.

For all the calculations above, the g-factors were estimated from Kane model calculation, which, to the best of our knowledge, have never been carefully identified in experiments. The anisotropy of the hole g-factor has been shown experimentally in p-type bulk HgMnTe [122], which is consistent with parameters estimated from the Kane model. The qualitative picture of the reentrant behavior is independent of the parameter details.

In the above, we show the phase diagram of the QAH effect with both the in-plane and out-of-plane magnetic fields and find a novel reentrant behavior due to the combination of the exchange coupling and the direct Zeeman coupling. However,

due to the non-zero $\mathcal{B}_z$, the formation of Landau level is inevitable. Therefore, it is natural to examine whether the reentrant behavior still exists after taking into account the orbital effect of Landau levels. Landau levels can be calculated by taking into account the orbital effect of magnetic fields in the model Hamiltonian (4.1) with the standard Peierls substitution [91, 123], which is described in details in the appendix B. The Landau level fan chart is plotted in Fig. 4.7, with the Fermi level set at 0.3 meV (the blue line). Fig. 4.7 (a) shows the Landau levels without $\mathcal{B}_x$, while Fig. 4.7 (b) and (c) show how the Landau level evolves with $\mathcal{B}_x$ at $\mathcal{B}_z = 0.2T$ and $\mathcal{B}_z = 0.6T$, respectively. In Fig. 4.7 (b), the system stays in the normal insulating regime for zero $\mathcal{B}_x$, and is driven to the regime with $-e^2/h$ with increasing $\mathcal{B}_x$, similar to the line $\mathcal{B}_z = 0.2T$ in Fig.4.5(c). For $\mathcal{B}_z = 0.6$T, before turning on $\mathcal{B}_x$, the Hall conductance is $\sigma_{xy} = \frac{-e^2}{h}$. The Fermi level crosses the electron zero mode twice and the Hall conductance undergoes the transitions from $-e^2/h$ to 0 to $-e^2/h$ as increasing $\mathcal{B}_x$. Fig. 4.7 demonstrates the stability of the phase diagram given in Fig. 4.5 in the presence of Landau levels and the underlying reason for the reentrant behavior is the change of spin splitting, rather than the orbital effect.

In conclusion, we have shown that the in-plane magnetic field can induce the QAH effect in HgMnTe quantum wells. A reentrant QAH effect is predicted as a result of the interplay between the exchange coupling and the direct Zeeman coupling. In addition, the reentrant behavior is stable in the presence of Landau levels. Although the reentrant QAH effect has not been observed in the current experiment due to the negligible in-plane g factor for Zeeman coupling, it might be observed for an even larger magnetic field or in other materials such as InAs/GaSb QWs.

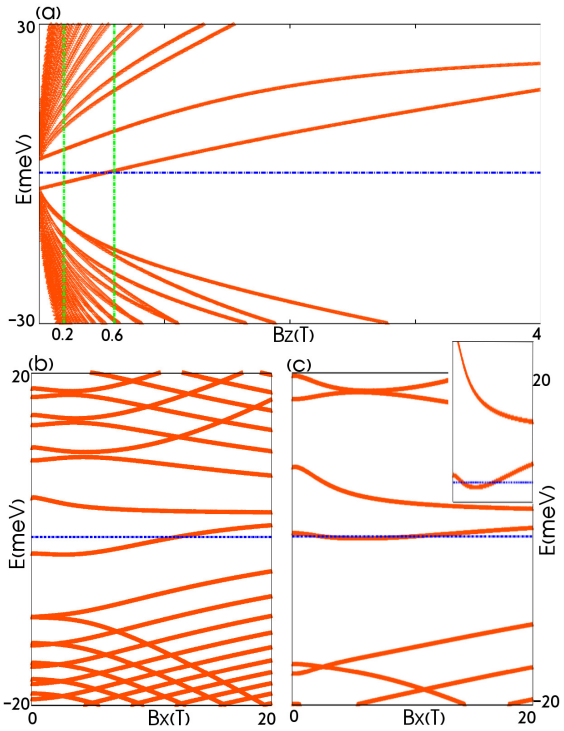

Figure 4.7. Landau Level fan chart. The parameters are the same as in Fig.4.5. The blue line indicate the Fermi level at 0.3meV. (a)Landau level fan chart without in-plane magnetization. (b)Landau level at $B_z = 0.2T$ in terms of in-plane magnetic field. (c)Landau level at $B_z = 0.6T$ in terms of in-plane magnetic field. The inset zooms in near Fermi level and shows the reentrant behavior.

4.4 $Hg_xMn_{1-x}Te$ quantum wells with shear strains

It is shown in the previous section that the conditions for the QAH phase are $|g| > |m|$ and a nonzero g_{2z}. To exclude the orbital effect completely, we would like to further study the conditions for QAH phase without the out-of-plane magnetization. We start from a general symmetry analysis of the necessary conditions for the appearance of non-zero Hall conductance. First, the Hall conductance must be zero in a TR invariant system, so a magnetic field or magnetization is required. Besides TR symmetry, the 2D point group (PG) symmetry gives an additional constraint for the Hall conductance, as first shown by Fang [124]. The 2D PGs consist of two families, the n-fold rotation symmetry C_n and the n-fold dihedral symmetry D_n [125]. The dihedral group D_n in 2D PGs is generated by the rotation

C_n and the reflection M. Here we emphasize that reflection M in 2D PGs always corresponds to the reflection in three dimensional (3D) PGs with the reflection plane perpendicular to the 2D plane. The reflection in 2D PGs plays the role of inversion in 3D and distinguishes the pseudo-scalar (pseudo-vector) from the scalar (vector). The Hall conductance is zero if the 2D system has any reflection symmetry M. For example, let's consider a system with the reflection symmetry M_x ($x \to -x, y \to y$) in the 2D plane, denoted as xy plane. For the Hall response $j_x = \sigma_{xy} E_y$, under M_x the current j_x changes its sign ($j_x \to -j_x$) while the electric field E_y keeps its sign, so the Hall response equation is changed to $j_x = -\sigma_{xy} E_y$. If the system is invariant under M_x, the response equation should also be invariant under M_x, constraining the Hall conductance σ_{xy} to be zero. Similar arguments can be applied to any 2D reflection symmetry. The out-of-plane magnetization is a pseudo-scalar in the 2D PGs, breaking any reflection symmetry M. In contrast, the in-plane magnetization, denoted as $\boldsymbol{m}$, is a pseudo-vector, and there is still a surviving reflection symmetry M_m with the reflection plane perpendicular to $\boldsymbol{m}$, thus the in-plane magnetization by itself can not induce a non-zero Hall conductance and it is necessary to introduce other mechanisms to break the remaining reflection symmetry M_m. The symmetry analysis gives us a guidance to search for the non-zero Hall conductance with in-plane magnetization and in below, we will present in HgMnTe quantum well ,not only the non-zero Hall conductance, but also the QAH effect can be realized with in-plane magnetization.

The effective model for Mn doped HgTe quantum wells is described by the (BHZ) Hamiltonian, Eq.(4.1), with spin-splitting, E.q.(4.2). The BHZ Hamiltonian has the D_∞ symmetry, so any plane perpendicular to the xy plane can serve as the reflection plane. The in-plane magnetization $\boldsymbol{m}$ preserves the reflection symmetry M_m, so the Hall conductance is zero for the BHZ model with the in-plane magnetization.

To obtain a non-zero Hall conductance, we need to break the remaining reflection symmetry, which can be achieved by introducing a new term due to the shear strains ϵ_{xz} and ϵ_{yz}, written as

$$H_{str} = F\left[\epsilon_{xz}(k_x\sigma_x + k_y\sigma_y) + \epsilon_{yz}(k_x\sigma_y - k_y\sigma_x)\right]\tau_x, \tag{4.9}$$

with the parameter F. This form of the Hamiltonian can be derived from the six-band Kane model [126,127], as described in details in the appendix. Experimentally,

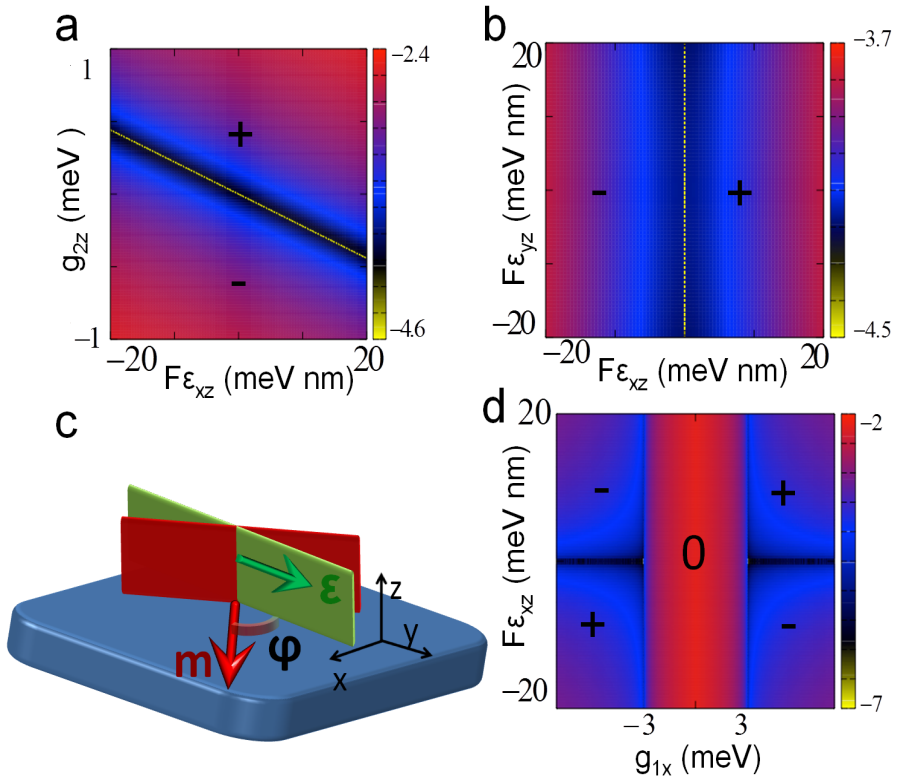

Figure 4.8. In-plane magnetization induced QAH effect in HgMnTe quantum wells. **(a)** The band gap as a function of g_{2z} and ϵ_{xz} with a finite $g_{1x} = 8$ meV. **(b)** The band gap as a function of ϵ_{xz} and ϵ_{yz} with $g_{1x} = 4$ meV, $g_{2x} = 3$ meV. **(c)** Schematic plot of the experimental setup. The angle between the strain vector $\boldsymbol{\epsilon}$ (green arrow) and the magnetization vector $\boldsymbol{m}$ (red arrow) is denoted as φ. The green plane denotes the reflection plane preserved by the strain vector $\boldsymbol{\epsilon}$ while the red plane denotes the reflection plane preserved by the magnetization vector $\boldsymbol{m}$. **(d)** The band gap as a function of g_{1x} and ϵ_{xz} with $g_{2z} = 0$. The other parameters are taken as $M = -3$ meV, $B = 0.85$ eV·nm^2, $D = 0.67$ eV·nm^2, $A = 0.38$ eV·nm, $g_{1(2)y} = g_{1z} = 0$, and $\epsilon_{yz} = 0$.

the shear strain appears in the HgTe-HgCdTe superlattices grown on CdZnTe substrate along an asymmetric direction, such as (112) direction [128–130]. ϵ_{xz} (ϵ_{yz}) term breaks the x-direction reflection $M_x = i\sigma_x\tau_o$ (the y-direction reflection $M_y = i\sigma_y\tau_z$) and preserves M_y (M_x). Fig.4.8 a shows the band gap for the Hamiltonian $H_{BHZ} + H_m + H_{str}$ as a function of ϵ_{xz} and g_{2z} with a finite in-plane magnetization g_{1x}. When $\epsilon_{xz} = 0$, the Hall conductance is $+\frac{e^2}{h}$ ($-\frac{e^2}{h}$) for positive

(negative) g_{2z}, as obtained in Ref. [90]. The system is metallic for $g_{2z} = 0$, separating the two QAH phases with opposite Hall conductances. With a finite ϵ_{xz}, we find the gapless line derives away from the line of $g_{2z} = 0$ and the regime with positive (negative) ϵ_{xz} and $g_{2z} = 0$ is adiabatically connected to the regime with positive (negative) g_{2z}, which indicates that the Hall conductance for a postive (negative) ϵ_{xz} is $+\frac{e^2}{h}$ $(-\frac{e^2}{h})$, as shown in Fig. 3a. In Fig.4.8 b, the band gap is plotted as a function of ϵ_{xz} and ϵ_{yz} with a finite g_{1x}, and a gapless line along $\epsilon_{xz} = 0$ separates two QAH phases with the Hall conductance $\pm\frac{e^2}{h}$. The Hall conductance vanishes along the gapless line, because both the shear strain ϵ_{yz} and the in-plane magentization $g_{1(2)x}$ preserves the reflection M_y. More generally, the Hall cnductance is always zero when two vectors, the shear strain $\boldsymbol{\epsilon} = (\epsilon_{xz}, \epsilon_{yz})$ and the in-plane magnetization $\boldsymbol{m}$, are perpendicular to each other. We emphasize that the shear strain ϵ_{ij} is a tensor in 3D PGs, but we can treat $\boldsymbol{\epsilon}$ as a vector in 2D PGs. According to Fig.4.8 b, we can consider the experimental configuration for the magnetization and shear strain for the HgMnTe quantum wells, as shown in Fig.4.8 c. When the angle φ between the strain vector $\boldsymbol{\epsilon}$ and the magnetization vector $\boldsymbol{m}$ is rotated across $\frac{\pi}{2}$ or $\frac{3\pi}{2}$, the Hall conductance switches between $\pm\frac{e^2}{h}$ of the two insulating phases. In Fig.4.8 d, we verify the stability of the QAH phases for different values of $\boldsymbol{g}_1$ and the QAH phase always exists when the in-plane magnetization is large enough.

Finally, we would like to emphasize the breaking of reflection symmetry is essential for the in-plane magnetization induced QAH effect. Generally, the pseudo-scalar, such as the out-of-plane magnetization, can break all the reflection symmetries in 2D PGs. Therefore, one should also construct a pseudo-scalar with the in-plane magnetization. For example, a pseudo-scalar, the dot product of a vector and a pseudo-vector $\boldsymbol{\epsilon} \cdot \boldsymbol{m}$, can be defined to characterize the Hall conductance in the HgMnTe quantum wells with shear strains. As shown in Fig. 4.8d, the sign of the Hall conductance is determined by the sign of the product of ϵ_{xz} and g_{1x}. We expect this strategy can also be applied to search for the QAH phase in other systems.

4.5 Experimental relevance and conclusions

Recently, experiments done by Molenkamp's group on the QAH effect in $Hg_xMn_{1-x}Te$ quantum wells found that the QAH-normal phase boundary never falls on the $\mathcal{B}_z = 0$ line irrespective of the magnitude of $\mathcal{B}_x$. The magnetic field reaches a

critical angle at the phase boundary. This result suggests that the in-plane spin splitting is insignificant such that the in-plane splitting never overcomes the insulating gap. Moreover, the result also implies that Zeeman coupling is negligible because the value of spin splitting is limited. From the discussion in the section 4.2, we numerically determined the QAH-normal phase transition by the adiabatic continuity argument and found a critical angle, which is similar to these experiments. Without Zeeman coupling, the phase boundary lies at a critical angle of magnetic field after the exchange coupling saturates. The critical angle is less than $\pi/2$ because the in-plane exchange coupling is much weaker than the out-of-plane exchange coupling. Our predictions provide the possibility to extract the strength of in-plane and out-of-plane exchange coupling strength by quantitatively fitting to the experiments. The relevant collaboration with Prof. Molenkamp's group about this experiment is still on progress. With Zeeman coupling, we found a reentrant QAH effect as a result of the interplay between the exchange coupling and Zeeman coupling. The reentrant behavior is unique to Mn-doped HgTe quantum well, not pure HgTe quantum well. In addition, the reentrant behavior is stable in the presence of Landau levels, so it is feasible under the present experimental condition to verify this effect in magnetic QSH insulators.

With shear strain, we propose the experiments with rotating in-plane magnetic fields, as shown in Fig.4.8(c), to confirm the predicted effect. Since no out-of-plane magnetization is required, the orbital effect from Landau levels of magnetic fields can be excluded completely. Therefore, the proposed setups can provide a clear experimental signal to distinguish the orbital effect of magnetic fields from the exchange effect of magnetic ions.

Chapter 5
Disordered Quantum anomalous Hall insulators

We have discussed how to realize the QAH effect and distinguish it from the conventional QH effect in Mn doped HgTe quantum wells. The Hall conductance is determined by adiabatic connection in the clean limit in the previous discussion. In this chapter, we present direct calculations of the conductance for a disordered QAH system within the Landauer-Büttiker formalism. Recently, the QAH effect has been observed in Cr or V doped $(Bi,Sb)_2Te_3$ films by [59, 93–96]. Therefore, in this chapter we focus on the disorder effect in this system due to its experimental relevance. An effective model taking into account two surface states is adopted to describe this system. We calculate the two-terminal conductance for this system in the periodic or open boundary condition, as well as anisotropy in magneto-resistance in the presence of a rotating magnetization. The robustness of chiral edge modes against disorder is examined in our numerical calculations.

5.1 Model Hamiltonian

Bi or Sb based chalcogenides have been demonstrated to be a 3D TI with a single Dirac cone on each surface. For thin film geometry, the low energy physics is dominated by two surface states from the top and bottom surfaces. Two surface states become hybridized and lead to a gap opening when the thickness reduces. Once the ferromagnetic order is introduced into the thin film and breaks TR symmetry, the QAH effect can be realized in a certain parameter regime, as shown

by Yu. et al [31]. The effective model Hamiltonian for this system reads [31]

$$H_o = \begin{pmatrix} 0 & ivk_- & m_k & 0 \\ -ivk_+ & 0 & 0 & m_k \\ m_k & 0 & 0 & -ivk_- \\ 0 & m_k & ivk_+ & 0 \end{pmatrix} \tag{5.1}$$

$$= m_k\tilde{\tau}_x\tilde{\sigma}_o - vk_x\tilde{\tau}_z\tilde{\sigma}_y + vk_y\tilde{\tau}_z\tilde{\sigma}_x \tag{5.2}$$

with the basis of $|t\uparrow\rangle, |t\downarrow\rangle, |b\uparrow\rangle, |b\downarrow\rangle$, where t, b denote the top and bottom surfaces, and $\uparrow, \downarrow$ refer to spin up and down states. m_k describes the tunneling between the top and bottom layers and can be expanded to the second order as $m_k = m - B(k_x^2 + k_y^2)$. m_k vanishes when the film is thick enough to prevent hybridization between the two layers. In the second line, $\tilde{\tau}$ acts on the orbital space and $\tilde{\sigma}$ acts on the spin space.

H_o can be rewritten into a block-diagonal form by the unitary transformation U

$$U = \frac{1}{\sqrt{2}} \begin{pmatrix} 1 & 0 & 1 & 0 \\ 0 & 1 & 0 & -1 \\ 0 & 1 & 0 & 1 \\ 1 & 0 & -1 & 0 \end{pmatrix}. \tag{5.3}$$

The new basis are the hybridized bonding and anti-bonding states of the top and bottom surfaces: $|+\uparrow\rangle, |-\downarrow\rangle, |+\downarrow\rangle, |-\uparrow\rangle$, where $|\pm\uparrow\rangle = (|t\uparrow\rangle \pm |b\uparrow\rangle)\sqrt{2}; |\pm\downarrow\rangle = (|t\downarrow\rangle \pm |b\downarrow\rangle)\sqrt{2}$ and the Hamiltonian H_o in the new basis is

$$H_o' = UH_oU^\dagger$$

$$= \begin{pmatrix} m_k & ivk_- & 0 & 0 \\ -ivk_+ & -m_k & 0 & 0 \\ 0 & 0 & m_k & -ivk_+ \\ 0 & 0 & ivk_- & -m_k \end{pmatrix} \tag{5.4}$$

$$= m_k\tau_o\sigma_z - vk_x\tau_z\sigma_y + vk_y\tau_o\sigma_x, \tag{5.5}$$

where τ acts on the orbital space and σ acts on the spin space. This Hamiltonian takes the same form as the BHZ Hamiltonian for HgTe/CdTe quantum wells [7], although the basis are different. In the numerical calculation of conductance, we use

the model Hamiltonian (5.5). The parameters are measured in unit of B, which is set to be unity. The other parameters are $m = 0.27$ and $A = 1$ for the calculations below.

After the ferromagnetic order is achieved, the effective Zeeman energy in the old basis is given by $h_{ex} = g\tilde{\tau}_o \vec{M} \cdot \vec{\tilde{\sigma}}$, where $\tilde{\tau}_o$ is identity, $\vec{M}$ is the exchange field. The exchange energy, h_{ex} has three components $h_{exj} = g\tilde{\tau}_o M_j \tilde{\sigma}_j, j = x, y, z$. For simplicity, we assume that the effective g-factor is isotropic.

The exchange energy in the new basis is given by $h'_{ex} = U h_{ex} U^\dagger$. The explicit forms of the exchange energy are

$$\begin{aligned}
h'_{exz} &= gM_z\tau_z\sigma_z \\
&= gM_z \begin{pmatrix} 1 & 0 & 0 & 0 \\ 0 & -1 & 0 & 0 \\ 0 & 0 & -1 & 0 \\ 0 & 0 & 0 & 1 \end{pmatrix} \\
h'_{exx} &= gM_x\tau_x\sigma_o \\
&= gM_x \begin{pmatrix} 0 & 0 & 1 & 0 \\ 0 & 0 & 0 & 1 \\ 1 & 0 & 0 & 0 \\ 0 & 1 & 0 & 0 \end{pmatrix} \\
h'_{exy} &= gM_y\tau_y\sigma_z \\
&= gM_y \begin{pmatrix} 0 & 0 & -i & 0 \\ 0 & 0 & 0 & i \\ i & 0 & 0 & 0 \\ 0 & -i & 0 & 0 \end{pmatrix}.
\end{aligned} \tag{5.6}$$

Because of rotational symmetry around the z-axis, we take the in-plane magnetization to be along the x-direction without the loss of generality. For the angle θ between M and the z-axis, we define $M_x = M\sin\theta, M_z = M\cos\theta$.

5.2 Anisotropic magneto-conductance

The anisotropic magneto-conductance in thin films of ferromagnetic TIs is presented in this section. In the calculation, magnetization strength is fixed and the exchange

energy $|gM|$ is kept larger than |m| to drive the system into the QAH phase, whereas the magnetization direction is varied.

We define transport direction along the x-axis. In order to compare transport properties with and without edge modes, we consider two boundary conditions for the y-axis: open boundary condition (OBC) and periodic boundary condition (PBC). OBC gives rise to edge states, while only bulk states appear in the PBC. The structure of the device is shown in Fig.2.4. The leads are assumed to be semi-infinite normal metal as described in Chapter 2.

The dispersions at several angles θ are given in Fig.5.1. (a)-(c) are for Hamiltonian with the OBC at $\theta = 0, \pi/4, \pi/2$, respectively. (d)-(f) are for bulk Hamiltonian with the PBC at $\theta = 0, \pi/4, \pi/2$, respectively. The edge states are intact as long as the bulk gap remains finite. The bulk gap closes when the magnetization is rotated to the in-plane direction, as seen Fig.5.1(f). For OBC, there is a gap of ≈ 0.045 (Fig.5.1(c)). It is a consequence of the finite size effect, rather than the property of the bulk Hamiltonian.

Next, we will verify the chirality of edge modes for $gM_z > 0$ and $gM_z < 0$ by computing the four-terminal transmission in the clean limit. The four-terminal device is depicted in Fig.5.2(a). According to the analysis based on the adiabatic connection in the Chapter 4, in the regime $|gM| > m$, the Hall conductances for $gM_z > 0$ and $gM_z < 0$ are opposite in sign, suggesting opposite chiralities. The phase transition occurs when the magnetization is rotated into the in-plane direction and the bulk energy gap closes. For the gapped phases, because of the perfect transmission of chiral edge states, the transmission $T_{p \leftarrow q}$ equals to 1 only when p and q are neighboring leads and $p \leftarrow q$ is along the propagating direction of the chiral edge mode [101]. The other transmission coefficients are zero. The numerical calculation indeed shows that the transmission from the lead q to p denoted by $T_{p \leftarrow q}$ equals to 1 only if $(p \leftarrow q)$ is equal to (4←1), (2←4), (3←2), (1←3) for $\theta > \pi/2$ and (1←4), (4←2), (2←3), (3←1) for $\theta < \pi/2$. The other transmission coefficients are zero. The schematic plot of the edge current flow is shown in Fig.5.2.

The two-terminal conductances for both OBC and PBC in the clean limit are shown in Fig.5.3. When Fermi level lies at the Dirac point, for OBC, the conductance equals to e^2/h(the QAH phase) at $\theta = 0$ then drops to 0.1(the insulating phase) at $\theta = \pi/2$, see Fig.5.3(a). Only one chiral edge mode contributes to the conductance

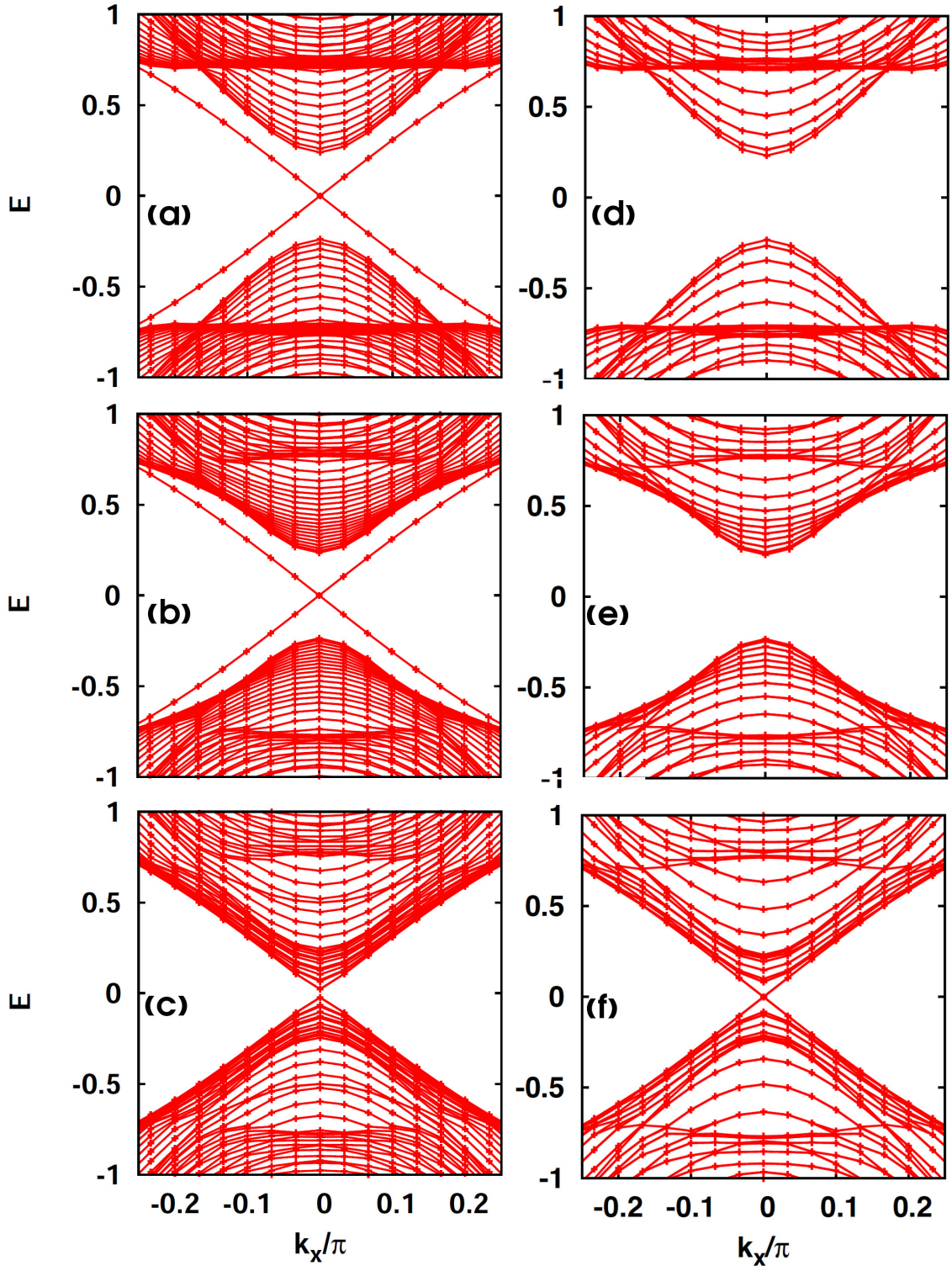

Figure 5.1. (a)-(c) are for the open boundary condition, (d)-(f) are for the periodic boundary condition. The corresponding angle from the top to the bottom row is $0, \pi/4, \pi/2$. The parameters used in the calculation are $m = 0.27, A = 1, B = 1, g = 1, M = 0.5$. The number of the transverse sites is 60.

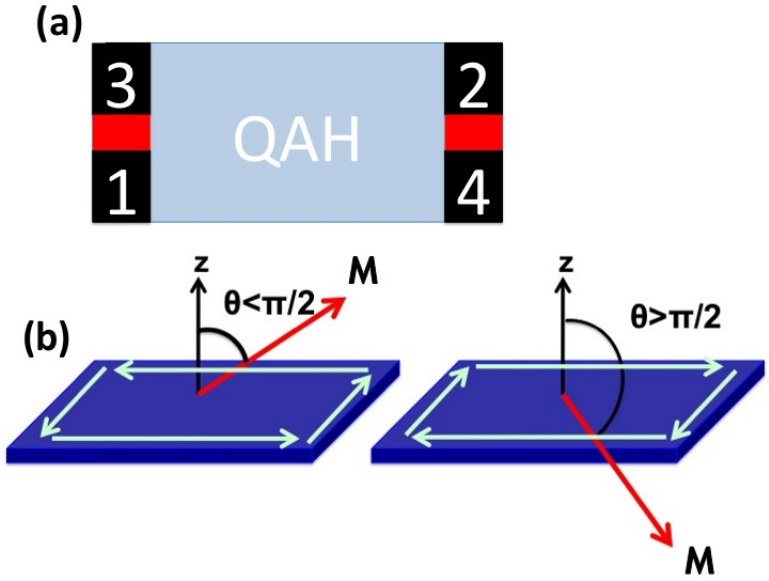

Figure 5.2. (a)The four-terminal device of QAH system for determination of the chirality. The leads are attached at the black parts. The red block between the leads is infinite potential barrier. It prevents unwanted scattering between two neighboring leads. (b)The chiral mode flips direction when the magnetization rotates from above to below the plane.

when magnetization has a large enough out-of-plane component, while for the in-plane magnetic field with $\theta = \pi/2$, a trivial gap of finite size effect opens up. There is no mode at Dirac point and thereby the conductance drops. For PBC (Fig.5.3(d)), conductance is zero at $\theta = 0$ then suddenly increases at $\theta = \pi/2$ as a consequence of bulk gap closing at this angle. As the Fermi level is shifted higher to 0.2 where at $\theta = 0$ it crosses only the edge mode, the conductance for OBC is quantized when $\theta = 0 - 0.36\pi, 0.64\pi - 1.36\pi$ and $1.64\pi - 2\pi$ as given in Fig.5.3(b). For PBC, conductance is zero before bulk gap closes. Near $\theta = \pi/2$, the conductance for both OBC and PBC increase because the Fermi energy crosses the bulk sub-bands, leading to a large contribution from bulk conductance. When the Fermi level lies inside the bulk bands, for both OBC and PBC(Fig.5.3(c) and (f)), the conductance is higher than e^2/h at $\theta = 0$ and increases at $\theta = \pi/2$ as bulk bands become closer in energy.

The conductance in disordered QAH systems is examined and shown in Fig.5.4. We find the qualitative feature of the conductance remains the same. The chiral mode is robust against disorder and the quantized conductance still exists even

for the strong disorder strength $W = 0.4$, which is almost close to the bulk gap edge($\approx$0.46)(Fig.(a)). At a higher Fermi energy, the bulk states are mixed with the edge mode by disorder; thus, the transmission starts to deviate away from unity even at a weaker disorder strength. The conductance peak is broadened as disorder gets stronger, irrespective of the Fermi energy because the bulk gap becomes smaller as θ gets closer to $\pi/2$.

5.3 conclusion

The anisotropic magneto-conductance of a ferromagnetic TI thin film is numerically studied in this chapter. When the out-of-plane component of the magnetization is strong enough, a magnetic gap is developed. The two-terminal conductance is e^2/h given by the ballistic transmission of the edge mode when the Fermi level is inside the gap. In the presence of disorder, the chiral edge mode of the QAH state, as well as the quantized conductance, is still robust up to a disorder strength close to half of the bulk band gap. When the magnetization is parallel to the plane, the gap is closed and the conductance is no longer quantized. The transport is dominated by bulk states and affected by disorder. This anisotropy is a result of the QAH-to-gapless state transition as shown by the dispersion.

Another way to directly calculate the Hall conductance is by Kubo formula in tight-binding representation. For a disordered system, the translational symmetry is broken, the twisted boundary condition is implemented [131]. More details on this calculation can be found in Appendix D.

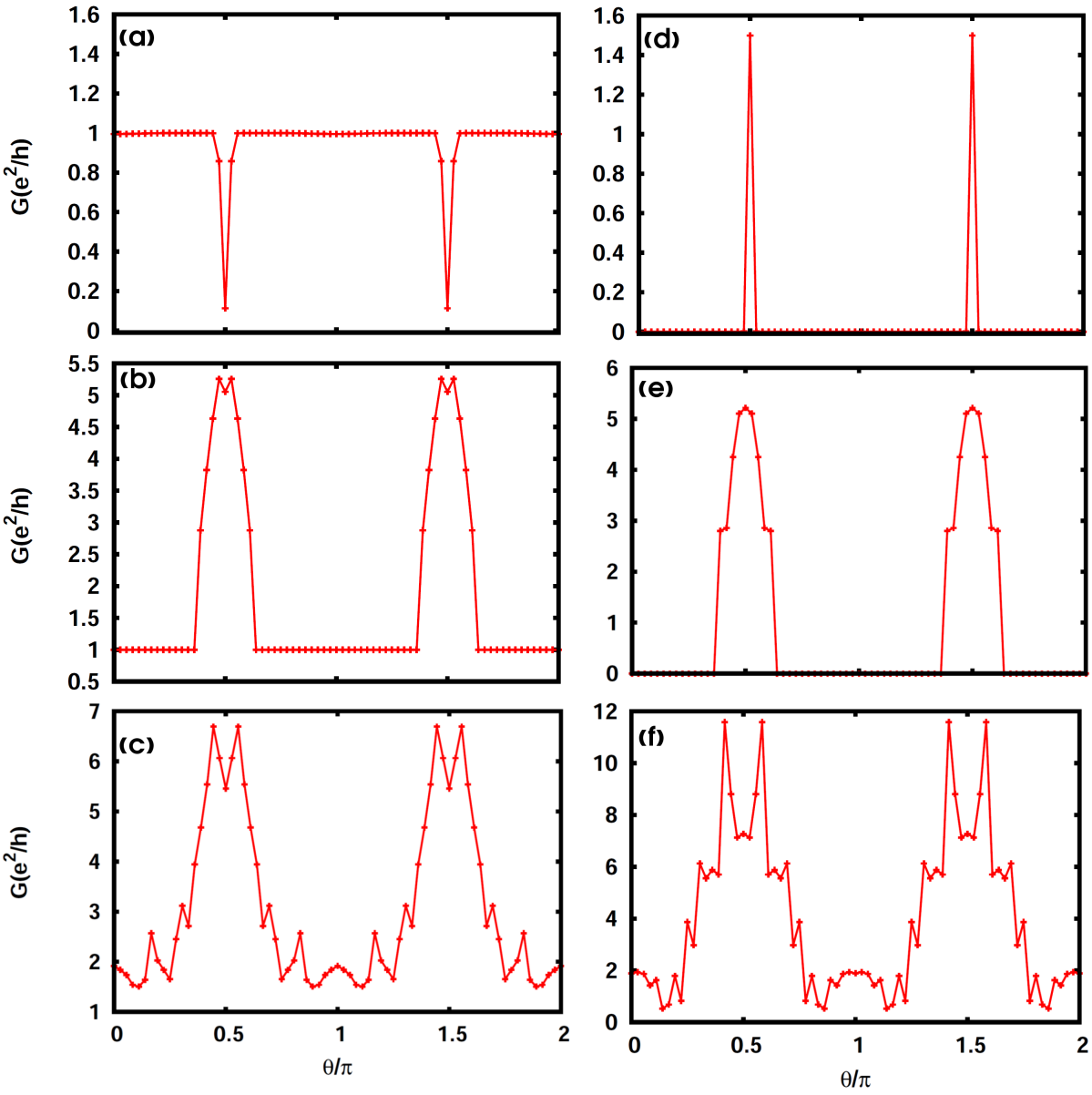

Figure 5.3. Two-terminal conductance in clean limit. (a)-(c) are for OBC. (d)-(f) are for PBC. The Fermi energy from the top to bottom row is $0, 0.2, 0.3$. The number of the longitudinal/transverse sites is 100/60.

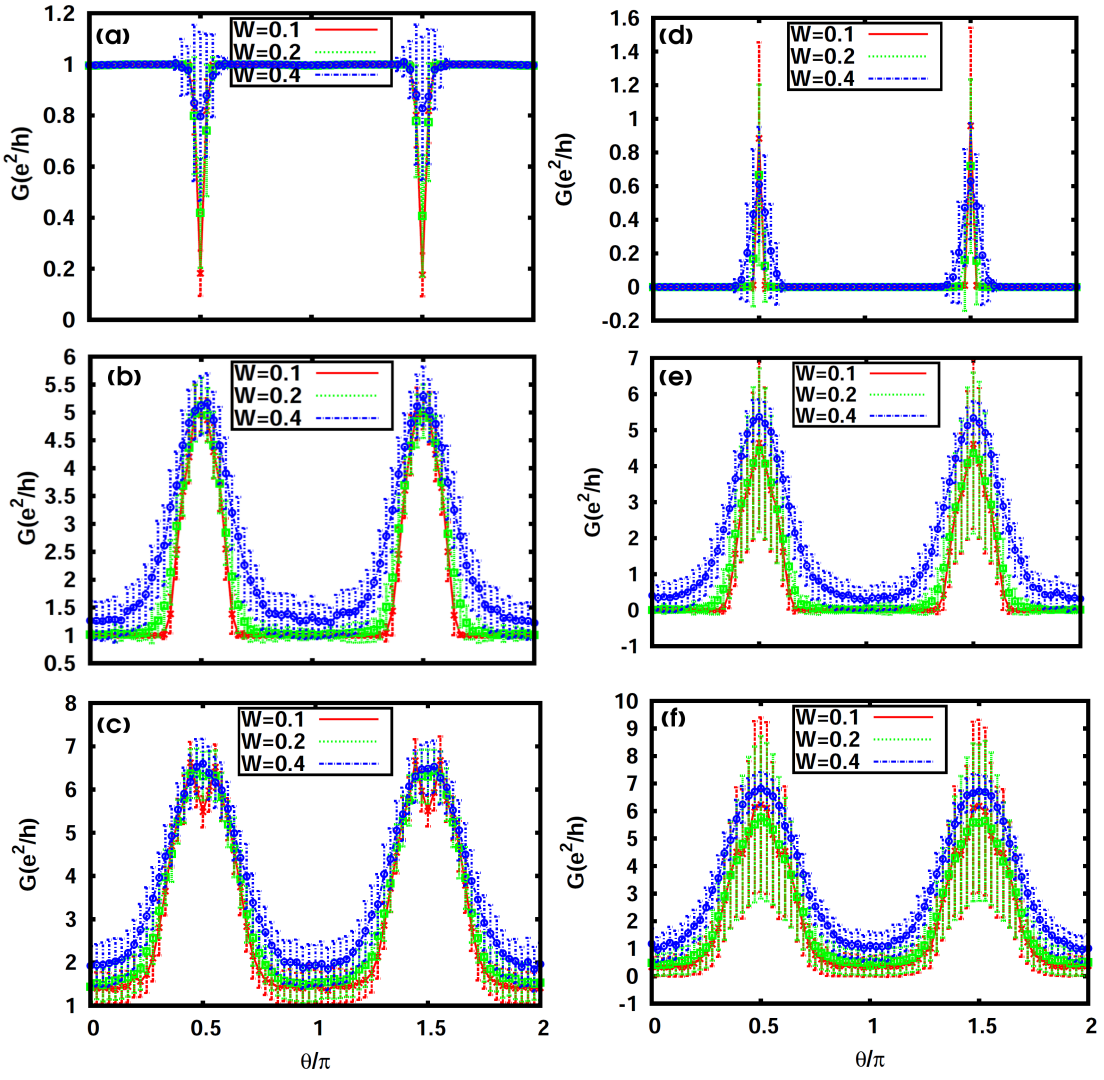

Figure 5.4. Two-terminal conductance in the presence of disorder. (a)-(c)are for OBC. (d)-(f) are for PBC. The Fermi energy from the top to bottom row is $0, 0.2, 0.3$. The number of the longitudinal/transverse sites is 100/60. The number of disorder configuration is 100.

Chapter 6
Summary and outlook

This dissertation is devoted to the study of transport behaviors in topological phases. In particular, we studied how the QH states and the QAH states behave when exchange coupling and Zeeman coupling coexist and are controlled by a rotating magnetic field and we also propose transport signatures of topological surface states of TI nanostructures. We summarize some of the principle results, as well as discussing possible new directions, in this chapter.

Transport signatures of topological surface states in TI nanostructures are studied. The magnetoconductance of TI nanowire is shown to have ϕ_0-periodicity when the non-topological surface states are localized by disorder. When a magnetic flux in the value of a half-integer of ϕ_0 is inserted along the nanowire, the surface electron gains an additional phase that cancels the Berry phase π from the curved surface of a TI nanostructure. A pair of topological modes appears at these values of magnetic flux. We have shown that topological surface states are much more robust against disorder than the nontopological states by comparing their localization lengths. The numerical results are supported by experimental measurements of magnetoconductance in BiTe nanotubes. The conductance oscillation is attributed to the contribution from outer surface states. We have argued that the inner radius fluctuates greatly along the nanotube direction leading to the disappearance of conductance oscillation related to the inner surface. The calculation in the clean limit has shown that the inner surface states have a longer penetration length than the outer surface states. Thus, the inner surface states are expected to be destroyed by magnetic flux more easily. One of the open problems is to numerically study the robustness of the inner surface state of a TI nanotube. It will provide a better understanding of the mechanism of the oscillation related to the inner

surface states. Another nontrivial effect of disorder is to produce the so-called topological Anderson insulator, in which an ordinary metal (with a positive gap) is driven into a topological insulator by disorder [108, 132, 133]. That physics is not relevant here because our system has an inverted band gap even in the absence of disorder. However, it would be worth exploring if our method for producing highly disordered systems can suggest ways of experimentally realizing topological Anderson insulators starting from materials with positive but small band gaps.

The QAH effect in Mn-doped HgTe quantum wells is investigated when rotation magnetic field, as well as the corresponding magnetization are present. Since the in-plane g-factors in HgMnTe quantum wells have not been determined experimentally to the best of our knowledge, we studied the normal-QAH phase transition with and without the in-plane Zeeman coupling. With Zeeman coupling, we predicted a reentrant QAH effect when both in-plane and out-of-pane magnetization are present in the system. On the contrary, if the in-pane Zeeman effect is negligible, there is no reentrant QAH effect. Instead, there is a critical angle of magnetic field below which the QAH effect can be observed. Moreover, with symmetry analysis, we reported that breaking the reflection symmetry is essential for the QAH effect. By introducing shear strain into the system, we find that the QAH effect can even be realized with purely in-plane magnetic fields. Since no out-of-plane magnetic field is involved, the QH effect can be excluded.

We also studied the anisotropic magnetoresistance in magnetic TI thin films When the magnetization is out-of-plane, the system is in the QAH state. When the magnetization is rotated into the in-plane direction, the gap closes and the transport is dominated by bulk states. In the QAH state, in which the helical edge state dominates the transport, the conductance is intact in the presence of disorder. One of the future studies is to generalize the two-terminal calculations to multi-terminal devices to obtain the Hall and longitudinal resistances.

Appendix A
Effective Hamiltonian of the TI surface states

A.1 Derivation of the Effective Hamiltonian of topological surface states

A 3D massive Dirac Hamiltonian is [134]

$$H = \begin{pmatrix} -M & v_f\vec{\sigma}\cdot\vec{p} \\ v_f\vec{\sigma}\cdot\vec{p} & M \end{pmatrix} \tag{A.1}$$

First, we consider a semi-infinite system extending from $-\infty$ to $x = 0$. We are interested in the surface state solution, which is a bound state at the interface $x = 0$ and decays for $x \to -\infty$. We separate the Hamiltonian into two parts

$$H = h_{1D} + \Delta H \tag{A.2}$$

$$h_{1D}(k_y, k_z = 0) = -M\tau_z\sigma_o + v_f p_x \tau_x \sigma_x \tag{A.3}$$

$$\Delta H(k_y, k_z) = \hbar v_f (k_y \tau_x \sigma_y + k_z \tau_x \sigma_z). \tag{A.4}$$

and consider the Hamiltonian h_1D at $k_y = k_z = 0$ first. The eigen-equation is $(-M\tau_z\sigma_o + v_f p_x \tau_x \sigma_x)\Psi = 0$ and here we are interested in the solution with zero energy. With the trial wave function for h_{1D} is (without normalization yet)

$$\Psi = e^{\alpha x}\xi, \tag{A.5}$$

the eigen-equation can be simplified as $M(i\tau_y\sigma_x)\xi = i\hbar v_f \alpha \xi$, which suggests that ξ is the eigenspinor of $\tau_y\sigma_x$ with eigenvalue $s = \pm 1$. α can be solved

$$\alpha = s\frac{M}{\hbar v_f} \quad s = +1 \text{ for } x < 0 \quad . \tag{A.6}$$

Thus, the degenerate eigenstates with $s = 1$ for the zero-energy solution are

$$\Psi_1 = \frac{\mathcal{N}}{\sqrt{2}} e^{\alpha x} \begin{pmatrix} 1 \\ 0 \\ 0 \\ i \end{pmatrix}; \Psi_2 = \frac{\mathcal{N}}{\sqrt{2}} e^{\alpha x} \begin{pmatrix} 0 \\ 1 \\ i \\ 0 \end{pmatrix}, \tag{A.7}$$

$\mathcal{N}$ is the normalization factor.

The eigenstates for h_{1D} are used as basis and ΔH is treated as perturbation to the one-dimensional Hamiltonian. Then we obtain an effective Hamiltonian of the helical surface states by projecting ΔH to the basis Ψ_1, Ψ_2 [135]

$$\begin{aligned} H_{eff} &= \begin{pmatrix} \langle\Psi_1| \\ \langle\Psi_2| \end{pmatrix} \Delta H \begin{pmatrix} |\Psi_1\rangle & |\Psi_2\rangle \end{pmatrix} & \text{(A.8)} \\ &= (\vec{p} \times \vec{\sigma})_x \, . & \text{(A.9)} \end{aligned}$$

The above effective Hamiltonian can be generalized to a curved surface with the normal vector $\mathbf{n}$. We can separate the Hamiltonian into

$$\begin{aligned} h_{1D} &= -M\tau_z\sigma_o + v_f p_\perp \tau_x (\vec{\sigma} \cdot \mathbf{n}) & \text{(A.10)} \\ \Delta H &= v_f \tau_x (\vec{\sigma} \cdot \vec{p}_\parallel), & \text{(A.11)} \end{aligned}$$

where $\vec{p}_\parallel$ is the momentum operator tangent to the surface.

Following the same procedure, we can also solve the solution of surface states for a curved space by assuming the curvature of space is quite small. Then we project the Hamiltonian ΔH into the subspace spanned by eigen states of surface states at $p_\parallel = 0$ and obtain the effective Hamiltonian of the surface state

$$H_{eff} = \frac{iv_f}{2} \left[\vec{\sigma} \cdot \vec{p}_\parallel, \vec{\sigma} \cdot \mathbf{n}\right]$$

$$
\begin{aligned}
&= \frac{iv_f}{2}\left\{(\vec{p}_\parallel\cdot\mathbf{n}) + i\vec{\sigma}\cdot(\vec{p}_\parallel\times\mathbf{n}) - (\mathbf{n}\cdot\vec{p}_\parallel) - i\vec{\sigma}\cdot(\mathbf{n}\times\vec{p}_\parallel)\right\} \\
&= \frac{\hbar v_f}{2}\nabla_\parallel\cdot\mathbf{n} + \frac{-i\hbar v_f}{2}\mathbf{n}\cdot(\nabla_\parallel\times\vec{\sigma}) + \frac{-i\hbar v_f}{2}(\nabla_\parallel\times\vec{\sigma})\cdot\mathbf{n} \qquad \text{(A.12)}
\end{aligned}
$$

From the first to the second line, the identity $(\vec{\sigma}\cdot\vec{A})(\vec{\sigma}\cdot\vec{B}) = \vec{A}\cdot\vec{B}+i\vec{\sigma}\cdot(\vec{A}\times\vec{B})$ is used. Here one should note that $\vec{p}_\parallel$ also differentiates on $\mathbf{n}$, and $\nabla_\parallel\cdot\mathbf{n} = (\nabla_\parallel\cdot\mathbf{n}) + \mathbf{n}\cdot\nabla_\parallel$. From the second to the third line, the identity $\vec{A}\cdot(\vec{B}\times\vec{C}) = \vec{B}\cdot(\vec{C}\times\vec{A}) = \vec{C}\cdot(\vec{A}\times\vec{B})$ is used.

Now we can write down the effective Hamiltonian for the surface states on a cylindrical surface with $\mathbf{n} = (\cos\phi, \sin\phi, 0)$. $\nabla_\parallel = \hat{\phi}\frac{1}{R}\frac{\partial}{\partial\phi} + \hat{z}\frac{\partial}{\partial z} = (-\sin\phi, \cos\phi, 0)\frac{1}{R}\frac{\partial}{\partial\phi} + \hat{z}\frac{\partial}{\partial z}$. Here, $-i\frac{\partial}{\partial z}$ can be replaced with wave vector k because of translational symmetry along the z direction.

$$
\begin{aligned}
\nabla_\parallel\cdot\mathbf{n} &= (-\sin\phi, \cos\phi, 0)\frac{1}{R}\frac{\partial}{\partial\phi}\cdot(\cos\phi, \sin\phi, 0) = \frac{1}{R} \qquad \text{(A.13)} \\
\nabla_\parallel\times\vec{\sigma} &= (\sigma_z\cos\phi, \sigma_z\sin\phi, -\sigma_y\sin\phi - \sigma_x\cos\phi)\frac{1}{R}\frac{\partial}{\partial\phi} + ik(-\sigma_y, \sigma_x, 0) \qquad \text{(A.14)}
\end{aligned}
$$

Substitute Eq.(A.13) and (A.14) into Eq.(A.12), the effective Hamiltonian for the carriers moving on the cylindrical surface is

$$
H^{\mathbf{n}}_{eff} = \frac{\hbar v_f}{2R} + \hbar v_f\begin{pmatrix} \frac{-i}{R}\frac{\partial}{\partial\phi} & ike^{-i\phi} \\ -ike^{i\phi} & \frac{i}{R}\frac{\partial}{\partial\phi}\end{pmatrix}. \qquad \text{(A.15)}
$$

A.2 Eigen-solution of the effective Hamiltonian

When an flux $\eta\phi_o$ (η is any number)is inserted into the nanowire, the flux is included by Pierels substitution $\vec{p}\to\vec{p}-e\vec{A}$ [123], where $\vec{A} = \frac{\eta\phi_o}{2\pi R}\hat{\phi}$. Thus, Eq.A.15 becomes

$$
H^{\mathbf{n}}_{eff} = \frac{\hbar v_f}{2R} + \hbar v_f\begin{pmatrix} \frac{-1}{R}(i\frac{\partial}{\partial\phi} + \eta) & ike^{-i\phi} \\ -ike^{i\phi} & \frac{1}{R}(i\frac{\partial}{\partial\phi} + \eta)\end{pmatrix} \qquad \text{(A.16)}
$$

The eigen function is

$$\chi = \begin{pmatrix} f_k \\ g_k e^{i\phi} \end{pmatrix} e^{i\phi l}, \tag{A.17}$$

where l is an integer $= 0, \pm 1, \pm 2...$ and is the quantum number for the azimuthal symmetry of the $H^{\mathbf{n}}_{eff}$. The eigen-equation becomes

$$H^{\mathbf{n}}_{eff}\chi \implies \hbar v_f \begin{pmatrix} \frac{l+1/2-\eta}{R} & ik \\ -ik & \frac{-l-1/2+\eta}{R} \end{pmatrix} \begin{pmatrix} f_k \\ g_k \end{pmatrix} = E \begin{pmatrix} f_k \\ g_k \end{pmatrix}. \tag{A.18}$$

Therefore, the eigenenergy is

$$E_{kl} = \pm\hbar v_f \sqrt{k^2 + (\frac{l+1/2-\eta}{R})^2} \tag{A.19}$$

A.3 Time-reversal invariance of the effective Hamiltonian

The time reversal operator is $T = i\sigma_y K$, where K is the complex conjugate operator. From E.q.(A.18), we can define $(f_k\ g_k)^T$ as the eigenstate of the effective Hamiltonian $\tilde{H}^{\mathbf{n}}_{eff}(k,l) = \hbar v_f(\frac{l+1/2-\eta}{R}\sigma_z - k\sigma_y)$. The time reversal operation of $\tilde{H}^{\mathbf{n}}_{eff}(k,l)$ gives $\tilde{H}^{\mathbf{n'}}_{eff}(k,l) = T^\dagger \tilde{H}^{\mathbf{n}}_{eff}(k,l)T = -\hbar v_f(\frac{l+1/2-\eta}{R}\sigma_z - k\sigma_y)$. The full Hamiltonian is given by the sum of $\tilde{H}^{\mathbf{n}}_{eff}(k,l)$ with all l, i.e. $\tilde{H}^{\mathbf{n}}_{eff}(k) = \sum_l \tilde{H}^{\mathbf{n}}_{eff}(k,l)$. If the Hamiltonian is time-reversal symmetric, then $\tilde{H}^{\mathbf{n'}}_{eff}(k) = \tilde{H}^{\mathbf{n}}_{eff}(-k)$. The dummy index l in $\tilde{H}^{\mathbf{n}}_{eff}(-k,l)$ can be changed to l' without the loss of generality. Thus, time-reversal symmetry gives $l' = -l - 1 + 2\eta$. However, this condition is only satisfied only when η equals to zero or half-integers because both l and l' are integers.

Appendix B
Landau level calculation

In this appendix, we show the Landau level calculation in the presence of in-plane magnetization for the BHZ Hamiltonian under a magnetic field [136]. The full Hamiltonian is $H_{BHZ} + H_m$, where $H_m = H_{mx} + H_{mz}$ and $H_{mx(z)} = \mathbf{g}_{1x(z)}\vec{\sigma}_{x(z)}\tau_0 + \mathbf{g}_{2x(z)}\vec{\sigma}_{x(z)}\tau_z$. H_{mx} is the in-plane magnetization and is regarded as the perturbation to Landau levels. The unperturbed Hamiltonian $H_{BHZ} + H_{mz}$ with the standard Peierls substitution [91, 123] is

$$H_o = H_{BHZ} + H_{mz} = \begin{pmatrix} H_{o\uparrow} & 0 \\ 0 & H_{o\downarrow} \end{pmatrix}, \tag{B.1}$$

where the Hamiltonian for each spin-component is a 2 by 2 matrix.

$$\begin{aligned} H_{o\uparrow} &= \begin{pmatrix} C + M - \frac{2(B+D)}{l_B^2}(a_+a_- + \frac{1}{2}) + g_{ez} & \frac{\sqrt{2}A}{l_B}a_+ \\ \frac{\sqrt{2}A}{l_B}a_- & C + M - \frac{(B-D)}{l_B^2}(a_+a_- + \frac{1}{2}) + g_{hz} \end{pmatrix} \\ H_{o\downarrow} &= \begin{pmatrix} C + M - \frac{(B+D)}{l_B^2}(a_+a_- + \frac{1}{2}) - g_{ez} & -\frac{\sqrt{2}A}{l_B}a_- \\ -\frac{\sqrt{2}A}{l_B^2}a_+ & C + M - \frac{(B-D)}{l_B^2}(a_+a_- + \frac{1}{2}) - g_{hz} \end{pmatrix}, \end{aligned}$$

where $l_B = \sqrt{\frac{\hbar}{e\mathcal{B}_z}}$ is the magnetic length and $a_\pm = \frac{l_B}{\sqrt{2}\hbar}(\mp ip_y + \hbar k_x + e\mathcal{B}_z y)$. The Landau gauge for the vector potential $\vec{A} = (-\mathcal{B}_z y, 0, 0)$ has been used.

H_o is block-diagonal, while H_{mx} is off block diagonal. First, we calculated the

eigenenergies and eigenstates for H_o. The eigenstates are written as

$$|n,l\rangle = \begin{pmatrix} f_{nl1}|n\rangle \\ f_{n-1l2}|n-1\rangle \\ f_{n-1l3}|n-1\rangle \\ f_{nl4}|n\rangle \end{pmatrix}, \tag{B.2}$$

where f_{nlj} $(j = 1, 2, 3, 4)$ are the coefficients of each eigenlevel of the Harmonic oscillator. n denotes the eigenlevel of the Harmonic oscillator, $l = 1, 2, 3, 4$, denotes the eigenstates of the effective 4×4 Hamiltonian, and j denotes the components of eigenvectors.

For convenience, we define

$$g_s = \frac{g_{hz} + g_{ez}}{2} \tag{B.3}$$

$$g_a = \frac{g_{hz} - g_{ez}}{2}. \tag{B.4}$$

In this basis, the eigenvalues for the zero modes are

$$E_{\uparrow,0} = C + M - \frac{(B+D)}{l_B^2} + g_{ez} \tag{B.5}$$

$$E_{\downarrow,0} = C - M + \frac{(B-D)}{l_B^2} - g_{hz} \tag{B.6}$$

$$\tag{B.7}$$

The eigenvalues for the non-zero modes are

$$E_{\uparrow,n\pm} = C - \frac{(B+2nD)}{l_B^2} + g_s \pm \sqrt{(M - g_a - \frac{(2nB+D)}{l_B^2})^2 + A^2\frac{\sqrt{2n}}{l_B}} \tag{B.8}$$

$$E_{\downarrow,n\pm} = C + \frac{(B-2nD)}{l_B^2} - g_s \pm \sqrt{(M + g_a - \frac{(2nB-D)}{l_B^2})^2 + A^2\frac{\sqrt{2n}}{l_B}} \tag{B.9}$$

And the eigenvectors for zero-modes are

$$|\uparrow,0\rangle = \begin{pmatrix} |0\rangle \\ 0 \\ 0 \\ 0 \end{pmatrix}; |\downarrow,0\rangle = \begin{pmatrix} 0 \\ 0 \\ 0 \\ |0\rangle \end{pmatrix}. \tag{B.10}$$

The eigenvectors for non-zero modes are

$$|\uparrow,n\pm\rangle = \frac{-l_B}{\sqrt{2n}A} \begin{pmatrix} -M + g_a + \frac{e}{\hbar}(D+2nB) \pm \sqrt{(M - g_a - \frac{e(2nB+D)}{\hbar})^2 + 2A^2\frac{\sqrt{2n}}{l_B}})|n\rangle \\ |n-1\rangle \\ 0 \\ 0 \end{pmatrix}$$

$$|\downarrow,n\pm\rangle = \frac{l_B}{\sqrt{2n}A} \begin{pmatrix} 0 \\ 0 \\ -M - g_a - \frac{e}{\hbar}(D-2nB) \pm \sqrt{(M + g_a + \frac{e(D-2nB)}{\hbar})^2 + 2A^2\frac{\sqrt{2n}}{l_B}})|n-1\rangle \\ |n\rangle \end{pmatrix}$$

The positive sign is for the hole eigenstates, while the negative sign is for the electron states. In this basis, H_0 is diagonal. Then we project H_{mx} onto this basis and the total Hamiltonian is diagonalized up to 20 basis of Landau levels numerically.

Appendix C
Effective Hamiltonian for HgMnTe quantum well

In this appendix, we discuss the form of the effective four band model of HgMnTe quantum wells with shear strains based on the symmetry argument, as well as the microscopic derivation based on $k \cdot p$ theory.

The effective Hamiltonian of HgMnTe quantum wells with shear strains is constructed on the basis $|E1+\rangle$, $|H1+\rangle$, $|E1-\rangle$ and $|H1-\rangle$, including three terms H_{BHZ}, H_m and H_{str}. The BHZ Hamiltonian H_{BHZ} has been discussed in the early literature [7, 34]. The most important feature of the BHZ Hamiltonian is the linear coupling between $|E1\pm\rangle$ and $|H1\pm\rangle$ due to opposite parities between these two sub-bands.

The Hamiltonian H_m is described by two vectors $\boldsymbol{g}_1 = \frac{1}{2}(\boldsymbol{g}_e + \boldsymbol{g}_h)$ and $\boldsymbol{g}_2 = \frac{1}{2}(\boldsymbol{g}_e - \boldsymbol{g}_h)$, which can be related to the spin splitting of the electron and heavy-hole sub-bands. As described in the main text, H_m has two origins: one is due to the direct Zeeman coupling to the external magnetic field, while the other orginates from the exchange coupling of magnetization. The direction of the vectors $\boldsymbol{g}_{1,2}$ or $\boldsymbol{g}_{e,h}$ are along the direction of the external magnetic fields, as well as the magnetization of the Mn magnetic moments. However, the dependence of $\boldsymbol{g}_{1,2}$ or $\boldsymbol{g}_{e,h}$ on the external magnetic field is quite complicted. Due to the quantum well configuration, there is also anisotropy between the spin splitting along the z-direction and that along the in-plane direction. For the z-direction, the form of spin splitting has already been obtained [126], given by

$$g_{e(h)z} = \frac{\mu_B}{2}\tilde{g}_{e(h)z}B_z + \chi_{e(h)z}S_z \tag{C.1}$$

with the effective g factor $\tilde{g}_{e(h)z}$ and the exchange coupling strength $\chi_{e(h)}$ for the electron (heavy-hole) sub-bands, respectively. S_z denotes the magnetization of Mn atoms $S_z = -S_0 B_{5/2}\left(\frac{5g_{Mn}\mu_B B_z}{2k_B(T+T_0)}\right)$ where $S_0 = 5/2$, the effective g factor for Mn g_{Mn}, the Bhor magneton μ_B, the characteristic temperature of the anti-ferromagnetic coupling T_0. $B_{5/2}(x)$ is the Brillioun function, given by $B_{5/2}(x) = \frac{6}{5}coth(\frac{6}{5}x) - \frac{1}{5}coth(\frac{1}{5}x)$. For the in-plane magnetic fields, the dependence of spin splitting on magnetic fiels is a little complicated. For the electron sub-band $|E1\pm\rangle$, the spin splitting is given by

$$g_{ex} + ig_{ey} = \frac{\mu_B}{2}\tilde{g}_{e\|}B_+ + \chi_{e\|}S_+, \tag{C.2}$$

with the in-plane g factor $\tilde{g}_{e\|}$ and the in-plane exchange coupling strength $\chi_{e\|}$. Here $B_\pm = B_x \pm iB_y$ and $S_\pm = S_x \pm iS_y$ with $S_{x(y)} = -S_0 B_{5/2}\left(\frac{5g_{Mn}\mu_B B_{x(y)}}{2k_B(T+T_0)}\right)$. In contrast, the spin splitting for the heavy-hole sub-bands is given by

$$g_{hx} + ig_{hy} = \frac{\mu_B}{2}\tilde{g}_{h\|}B_+^3 + \chi_{h\|}S_+^3. \tag{C.3}$$

The B_+^3 and S_+^3 dependence for the heavy-hole sub-bands is because the heavy-hole sub-bands carry the angular momentum $\pm\frac{3}{2}$.

For the shear strain term, the Hamiltonian (E.q.(4.9)) can be written explicitly as

$$H_{strain} = F\begin{pmatrix} 0 & 0 & 0 & k_-(\epsilon_{xz} - i\epsilon_{yz}) \\ 0 & 0 & k_-(\epsilon_{xz} - i\epsilon_{yz}) & 0 \\ 0 & k_+(\epsilon_{xz} + i\epsilon_{yz}) & 0 & 0 \\ k_+(\epsilon_{xz} + i\epsilon_{yz}) & 0 & 0 & 0 \end{pmatrix} \tag{C.4}$$

in the basis $|E1+\rangle$, $|H1+\rangle$, $|E1-\rangle$ and $|H1-\rangle$, with the shear strains ϵ_{xz} and ϵ_{yz} and the coefficient F. ϵ_{xz} and ϵ_{yz} have even parity and $\epsilon_\pm = \epsilon_{xz} \pm i\epsilon_{yz}$ carry the angular momentum ± 1. Therefore, the term $k_\pm(\epsilon_{xz} \pm i\epsilon_{yz})$ carries the angular momentum ± 2, corresponding to the change of the angular momentum between the electron sub-band $|E1+\rangle$ ($|E1-\rangle$) with the angular momentum $\frac{1}{2}$ ($-\frac{1}{2}$) and the heavy-hole sub-band $|H1-\rangle$ ($|H1+\rangle$) with the angular momentum $-\frac{3}{2}$ ($\frac{3}{2}$).

In order to confirm our discussion of the strain term, we may also consider the perturbation theory for the derivation of this term. We may start from the six

band Kane model with the strain term, with the Hamiltonian given by

$$H = H_K + H_{str}, \tag{C.5}$$

in the basis $|\Gamma^6, 1/2\rangle$, $|\Gamma^6, -1/2\rangle$, $|\Gamma^8, 3/2\rangle$, $|\Gamma^8, 1/2\rangle$, $|\Gamma^8, -1/2\rangle$ and $|\Gamma^8, -3/2\rangle$, which we denote as $|1\rangle, |2\rangle, |3\rangle, |4\rangle, |5\rangle, |6\rangle$ for short in the following. In the conventional semiconductor, the Γ^6 bands have higher energy than the Γ^8 bands while in HgTe, the bands sequence is opposite. The strain term can be described by the Bir-Pikus Hamiltonian with the substituion $k_i k_j$ in the Kane Hamiltonian of the strain tensor component ϵ_{ij}. For the present model, we obtain

$$H_{str} = \begin{pmatrix} T_\epsilon & 0 & 0 & 0 & 0 & 0 \\ 0 & T_\epsilon & 0 & 0 & 0 & 0 \\ 0 & 0 & U_\epsilon + V_\epsilon & S_\epsilon & R_\epsilon & 0 \\ 0 & 0 & S_\epsilon^\dagger & U_\epsilon - V_\epsilon & 0 & R_\epsilon \\ 0 & 0 & R_\epsilon^\dagger & 0 & U_\epsilon - V_\epsilon & -S_\epsilon \\ 0 & 0 & 0 & R_\epsilon^\dagger & -S_\epsilon^\dagger & U_\epsilon + V_\epsilon \end{pmatrix} \tag{C.6}$$

with

$$T_\epsilon = C\mathrm{tr}(\epsilon), \tag{C.7}$$

$$U_\epsilon = a\mathrm{tr}(\epsilon), \tag{C.8}$$

$$V_\epsilon = \frac{1}{2}b(\epsilon_{xx} + \epsilon_{yy} - 2\epsilon_{zz}), \tag{C.9}$$

$$S_\epsilon = -d(\epsilon_{xz} - i\epsilon_{yz}), \tag{C.10}$$

$$R_\epsilon = -\frac{\sqrt{3}}{2}b(\epsilon_{xx} - \epsilon_{yy}) + id\epsilon_{xy}. \tag{C.11}$$

Here $\mathrm{tr}(\epsilon) = \epsilon_{xx} + \epsilon_{yy} + \epsilon_{zz}$ gives the trace of the tensor ϵ. Here we are interested in the influence of ϵ_{xz} and ϵ_{yz} and keep only ϵ_{xz} andϵ_{yz} non-zero. From the above expressions, we find only S_ϵ terms remaining.

Next let's consider the projection of the Hamiltonian into the subspace of the quantum well sub-bands and derive the effective Hamiltonian for the low energy physics. We consider a quantum well structure frabricated along z direction and separate the Hamiltonian H into two parts, $H = H_{k_\parallel=0} + H^{(1)}_{k_\parallel}$ with $k_\parallel = (k_x, k_y)$. $H_{k_\parallel=0}$ describes the Hamiltonian with vanishing $k_\parallel$ and is solved with numerical

methods. The eigen wave functions of $H_{k_\parallel=0}$ is denoted as $|U_\xi(z)\rangle = \sum_\lambda f_{\xi,\lambda}(z)|\lambda\rangle$, where $|\lambda\rangle = |\Gamma^6, \pm\frac{1}{2}\rangle$ or $|\Gamma^8, \pm\frac{3}{2}(\pm\frac{1}{2})\rangle$. We use again 1 to 6 to denote λ for short. ξ denote different sub-bands and here we are interested in four sub-bands $|E_1, +\rangle$, $|H_1, +\rangle$, $|E_1, -\rangle$ and $|H_1, -\rangle$, denoted as $|A\rangle, |B\rangle, |C\rangle, |D\rangle$, with the forms given by

$$\begin{aligned} |A\rangle &= f_{A,1}(z)|1\rangle + f_{A,4}(z)|4\rangle, \qquad |B\rangle = f_{B,3}|3\rangle \\ |C\rangle &= f_{C,2}(z)|2\rangle + f_{C,5}(z)|5\rangle, \qquad |D\rangle = f_{D,6}|6\rangle. \end{aligned} \tag{C.12}$$

The symmetry property of the functions $f_{\xi,\lambda}$ is discussed in the Ref. [126]. We also consider other sub-bands, such as $|E_1, \pm\rangle$, $|LH, \pm\rangle$, $|HH_{2,3,\cdots}, \pm\rangle$, in the second order perturbation calculation.

The effective Hamiltonian in the four bands (A,B,C,D sub-bands) can be obtained from the second order perturbation, which is illustrated in Ref. [126] for the details. Here we are only interested in the terms related to the shear strains. For the first order term, the possible term is $\langle A|H_{str}|B\rangle = -(\epsilon_{xy} + i\epsilon_{yz})\langle f_{A,4}|d|f_{B,3}\rangle$, which vanishes because of the opposite party between $f_{A,4}$ and $f_{B,3}$ (see Ref. [126] for more details). Similar situation happens for $\langle C|H_{str}|D\rangle$. For the second order perturbation, the terms with the form $\langle A|H_K|LH, -\rangle\langle LH, -|H_{str}|D\rangle$ and $\langle B|H_{str}|LH, +\rangle\langle LH, -|H_K|C\rangle$ remains, yielding the Hamiltonian (C.4), with the coefficient F given by

$$F = \sum_{\alpha=LH,E_2} \frac{1}{2\sqrt{6}}(\langle f_{A,1}|P|f_{\alpha^-,5}\rangle - \langle f_{A,4}|P|f_{\alpha^-,2}\rangle)\langle f_{\alpha^-,5}|d|f_{D,6}\rangle \left(\frac{1}{E_A - E_{\alpha^-}} + \frac{1}{E_D - E_{\alpha^-}}\right).$$

Appendix D
Quantized Hall conductance and extended states

The localization theory predicted that all electronic states are localized in the absence of magnetic field in two-dimensional systems. When there is magnetic field and the electronic states form Landau levels, in contrast, there are extended states that carry Hall conductance. Great interest has been attracted to study in the evolution of extended states when the gap between Landau levels collapses [137]. In this appendix, we show the fate of extended state in the presence of disorder in IQH insulators. The generalization to the QAH insulators has been investigated and shown similar behavior as in the IQH effect [138].

Niu et al [131] generalized the Kubo formula to disordered systems and showed that the Hall conductance is still a quantized value as long as the Fermi gap does not close. Moreover, Hall conductance is insensitive to the boundary condition. The boundary condition averaged Hall conductance takes the form

$$\sigma = -\frac{e^2}{h}C \tag{D.1}$$

$$C = 4\pi \sum_{E_o<E_f} \sum_{E_n>E_f} \frac{1}{4\pi^2} \int_0^{2\pi} d\theta_x \int_0^{2\pi} d\theta_y \frac{Im\langle\psi_o|\hbar v_x|\psi_n\rangle\langle\psi_n|\hbar v_y|\psi_o\rangle}{(E_o - E_n)^2}, \tag{D.2}$$

where $v_i = \frac{1}{\hbar}\frac{\partial H}{\partial \theta_i}$ and $\theta_{x,y}$ are the phase for boundary conditions as defined in the following. In the tight-binding representation, the Hamiltonian for a square lattice

in the presence of magnetic field is

$$H = \sum_{m,n} tC^{\dagger}_{m+1,n}C_{m,n} + te^{i2\pi m\phi/\phi_o}C^{\dagger}_{m,n+1}C_{m,n} \tag{D.3}$$

ϕ is the magnetic flux per unit cell and $C^{\dagger}_{m,n}/C_{m,n}$ is the creation/annihilation operator at lattice site (m,n). The lattice site index runs from 0 to $N_{x(y)}$ for the $x(y)-$direction. To restore periodic boundary condition along x-direction, we set $\phi/\phi_o = p/q$ and $N_x = qd$, where p, q and d are integers. The phases only appear for the hopping between the opposite edges: $h_{N_x\to 0} = e^{i\theta_x}C^{\dagger}_{0,y}C_{N_x,y}$ and $h_{N_y\to 0} = e^{i\theta_y}C^{\dagger}_{x,0}C_{x,N_y}$. Therefore, the only nonzero matrix elements for v_i are the boundary terms. Eq.D.2 has the same form as in the clean limit only by replacing wave vector with phase. In the calculation, we focus on the case $\phi/\phi_o = p/q = 1/3$. We should point out that in this calculation, Kubo formula is a bulk property and there is no edge effect.

The extended states are defined as the states that carry nonzero Hall conductance [137, 139]. The calculation is for the magnetic flux per lattice for a 9×9 square lattice. The density of state and the Hall conductances are averaged over boundary conditions and disorder configurations. Fig.D.1(a) and (b) give the density of states and the Hall conductance at disorder strength 1 and 2.5, respectively. Fig.D.1(a) shows that the extended states locate at the center of each subband. The Hall conductance of each subband is $1, -2, 1$. Comparing Fig.D.1(a) and (b), as disorder strength increases, the extended states with opposite Hall conductance merge and disappear. Our results match that of Ref [137].

The fate of the extended states in the Haldane model has been studied by Onoda and Nagaosa [138]. Based on the scaling analysis, they showed that the two extended states merge and disappear at a critical disorder strength. This behavior is the same as in the integer quantum Hall effects [137].

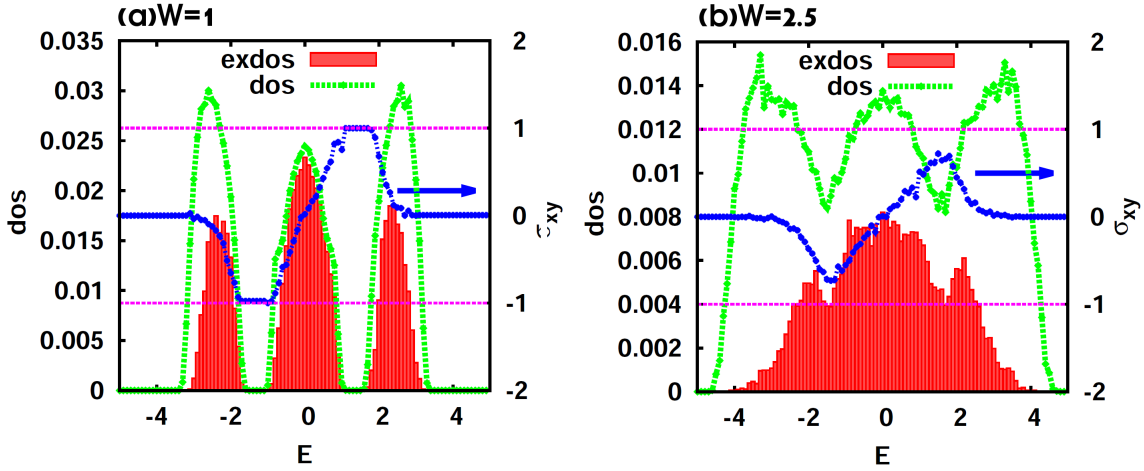

Figure D.1. Total density of states, extended density of states and Hall conductance for $W = 1$(a) and $W = 2.5$(b). $p/q = 1/3$ for systems of size 9×9. The disorder configuration is 400. The number of grid for boundary condition is 24×24.

Bibliography

[1] Hall, E. H. (1879) "On a New Action of the Magnet on Electric Currents," *American Journal of Mathematics*, **2**(3), pp. pp. 287–292.

[2] Hall, E. (1881) *Philose. Mag.*, **12**, p. 157.

[3] Nagaosa, N., J. Sinova, S. Onoda, A. H. MacDonald, and N. P. Ong (2010) "Anomalous Hall effect," *Rev. Mod. Phys.*, **82**, pp. 1539–1592.

[4] Xiao, D., M.-C. Chang, and Q. Niu (2010) "Berry phase effects on electronic properties," *Rev. Mod. Phys.*, **82**, pp. 1959–2007.

[5] Klitzing, K. v., G. Dorda, and M. Pepper (1980) "New Method for High-Accuracy Determination of the Fine-Structure Constant Based on Quantized Hall Resistance," *Phys. Rev. Lett.*, **45**(6), pp. 494–497.

[6] Stormer, H. L. (1999) "Nobel Lecture: The fractional quantum Hall effect," *Rev. Mod. Phys.*, **71**, pp. 875–889.

[7] Bernevig, B. A., T. L. Hughes, and S. C. Zhang (2006) "Quantum spin Hall effect and topological phase transition in HgTe quantum wells," *Science*, **314**, p. 1757.

[8] Jain, J. K. (2007) *Composite Fermions*, Cambridge University Press.

[9] König, M., H. Buhmann, L. W. Molenkamp, T. L. Hughes, C.-X. Liu, X. L. Qi, and S. C. Zhang (2008) "The quantum spin Hall effect: theory and experiment," *J. Phys. Soc. Jpn*, **77**, p. 031007.

[10] Liu, C.-X., X.-L. Qi, X. Dai, Z. Fang, and S.-C. Zhang (2008) "Quantum Anomalous Hall Effect in $Hg_{1-y}Mn_yTe$ Quantum Wells," *Phys. Rev. Lett.*, **101**, p. 146802.

[11] Girvin, S. M. (2009), "The Quantum Hall Effect: Novel Excitations and Broken Symmetries," e-print arxiv:9907002.

[12] Thouless, D. J., M. Kohmoto, M. P. Nightingale, and M. den Nijs (1982) "Quantized Hall conductance in a two-dimensional periodic potential," *Phys. Rev. Lett.*, **49**, p. 405.

[13] Tsui, D. C., H. L. Stormer, and A. C. Gossard (1982) "Two-Dimensional Magnetotransport in the Extreme Quantum Limit," *Phys. Rev. Lett.*, **48**, p. 1559.

[14] Laughlin, R. B. (1983) "Anomalous Quantum Hall Effect: An Incompressible Quantum Fluid with Fractionally Charged Excitations," *Phys. Rev. Lett.*, **50**, p. 1395.

[15] Jain, J. K. (1989) "Composite-fermion approach for the fractional quantum Hall effect," *Phys. Rev. Lett.*, **63**(2), pp. 199–202.

[16] Landau, L. D. and E. M. Lifshitz (1980) *Statistical Physics*, Pergamon Press, Oxford.

[17] Kane, C. L. and E. J. Mele (2005) "Quantum spin Hall effect in graphene," *Phys. Rev. Lett.*, **95**, p. 226801.

[18] König, M., S. Wiedmann, C. Brüne, A. Roth, H. Buhmann, L. Molenkamp, X.-L. Qi, and S.-C. Zhang (2007) "Quantum spin Hall insulator state in HgTe quantum wells," *Science*, **318**, p. 766.

[19] Knez, I., R.-R. Du, and G. Sullivan (2011) "Evidence for Helical Edge Modes in Inverted InAs/GaSb Quantum Wells," *Phys. Rev. Lett.*, **107**, p. 136603.

[20] Hsieh, D., D. Qian, L. Wray, Y. Xia, Y. S. Hor, R. J. Cava, and M. Z. Hasan (2008) "A topological Dirac insulator in a quantum spin Hall phase," *Nature*, **452**, p. 970.

[21] Chen, Y. L., J. G. Analytis, J. H. Chu, Z. K. Liu, S.-K. Mo, X. L. Qi, H. J. Zhang, D. H. Lu, X. Dai, Z. Fang, S. C. Zhang, I. R. Fisher, Z. Hussain, and Z.-X. Shen (2009) "Large Gap Topological Insulator Bi2Te3 with a Single Dirac Cone on the Surface," *Science*, **325**, p. 178.

[22] Cheng, P., C. Song, T. Zhang, Y. Zhang, Y. Wang, J.-F. Jia, J. Wang, Y. Wang, B.-F. Zhu, X. Chen, X. Ma, K. He, L. Wang, X. Dai, Z. Fang, X. Xie, X.-L. Qi, C.-X. Liu, S.-C. Zhang, and Q.-K. Xue (2010) "Landau Quantization of Topological Surface States in Bi_2Se_3," *Phys. Rev. Lett.*, **105**(7), p. 076801.

[23] Peng, H., K. Lai, D. Kong, S. Meister, Y. Chen, X. L. Qi, S. C. Zhang, Z. X. Shen, and Y. Cui (2010) "Aharonov-Bohm interference in topological insulator nanoribbons," *Nature Mater.*, **9**, p. 225.

[24] Brüne, C., C. X. Liu, E. G. Novik, E. M. Hankiewicz, H. Buhmann, Y. L. Chen, X. L. Qi, Z. X. Shen, S. C. Zhang, and L. W. Molenkamp (2011) "Quantum Hall Effect from the Topological Surface States of Strained Bulk HgTe," *Phys. Rev. Lett.*, **106**, p. 126803.

[25] Hong, S. S., Y. Zhang, J. J. Cha, X.-L. Qi, and Y. Cui (2014) "One-Dimensional Helical Transport in Topological Insulator Nanowire Interferometers," *Nano Lett.*, **14**, p. 2815.

[26] Haldane, F. D. M. (1988) "Model for a quantum Hall effect without Landau levels: Condensed-matter realization of the "parity anomaly"," *Phys. Rev. Lett.*, **61**, p. 2015.

[27] Rechtsman, M. C., J. M. Zeuner, Y. Plotnik, Y. Lumer, D. Podolsky, F. Dreisow, S. Nolte, M. Segev, and A. Szameit (2013) "Photonic Floquet topological insulators," *Nature*, **496**, pp. 196–200.

[28] Jotzu, G., M. Messer, R. Desbuquois, M. Lebrat, T. Uehlinger, D. Greif, and T. Esslinger (2014) "Experimental realization of the topological Haldane model with ultracold fermions," *Nature*, **515**, pp. 237–240.

[29] X.L. Qi, Y.S. Wu, and S.C. Zhang (2006) "Topological quantization of the spin Hall effect in two-dimensional paramagnetic semiconductors," *Phys. Rev. B*, **74**, p. 085308.

[30] Liu, C.-X., X.-L. Qi, X. Dai, Z. Fang, and S.-C. Zhang (2008) "Quantum Anomalous Hall Effect in $Hg_{1-y}Mn_yTe$ Quantum Wells," *Phys. Rev. Lett.*, **101**, p. 146802.

[31] Yu, R., W. Zhang, H. J. Zhang, S. C. Zhang, X. Dai, and Z. Fang (2010) "Quantized Anomalous Hall Effect in Magnetic Topological Insulators," *Science*, **329**, pp. 61–64.

[32] Kitaev, A. (2009) "Periodic table for topological insulators and superconductors," *AIP Conf. Proc.*, **1134**, p. 22.

[33] Qi, X.-L., T. L. Hughes, S. Raghu, and S.-C. Zhang (2009) "Time-Reversal-Invariant Topological Superconductors and Superfluids in Two and Three Dimensions," *Phys. Rev. Lett.*, **102**, p. 187001.

[34] Qi, X.-L. and S.-C. Zhang (2011) "Topological insulators and superconductors," *Rev. Mod. Phys.*, **83**, pp. 1057–1110.

[35] Raghu, S., X.-L. Qi, C. Honerkamp, and S.-C. Zhang (2008) "Topological Mott Insulators," *Phys. Rev. Lett.*, **100**, p. 156401.

[36] Pesin, D. A. and L. Balents (2010) "Mott physics and band topology in materials with strong spin-orbit interaction," *Nature Phys.*, **6**, p. 376.

[37] Maciejko, J., V. Chua, and G. A. Fiete (2014) "Topological Order in a Correlated Three-Dimensional Topological Insulator," *Phys. Rev. Lett.*, **112**, p. 016404.

[38] Sun, K., Z. Gu, H. Katsura, and S. Das Sarma (2011) "Nearly Flatbands with Nontrivial Topology," *Phys. Rev. Lett.*, **106**(23), p. 236803.

[39] Levin, M. and A. Stern (2009) "Fractional Topological Insulators," *Phys. Rev. Lett.*, **103**, p. 196803.

[40] Regnault, N. and B. A. Bernevig (2011), "Fractional Chern Insulator," e-print arXiv:1105.4867.

[41] Wu, Y.-L., B. A. Bernevig, and N. Regnault (2012) "Zoology of fractional Chern insulators," *Phys. Rev. B*, **85**, p. 075116.

[42] Fu, L. (2011) "Topological Crystalline Insulators," *Phys. Rev. Lett.*, **106**, p. 106802.

[43] Hsieh, T. H., H. Lin, J. Liu, W. Duan, A. Bansil, and L. Fu (2012) "Topological Crystalline Insulators in the SnTe Material Class," *Nature Communications*, **3**, p. 982.

[44] Dziawa, P., B. J. Kowalski, K. Dybko, R. Buczko, A. Szczerbakow, M. Szot, E. ?usakowska, T. Balasubramanian, B. M. Wojek, M. H. Berntsen, O. Tjernberg, and T. Story (2012) "Topological crystalline insulator states in $Pb_{1?x}Sn_xSe$," *Nature Mater.*, **11**, pp. 1023–1027.

[45] Tanaka, Y., Z. Ren, T. Sato, K. Nakayama, S. Souma, T. Takahashi, K. Segawa, and Y. Ando (2012) "Experimental realization of a topological crystalline insulator in SnTe," *Nature Phys.*, **8**, pp. 800–803.

[46] Wang, Z., Y. Chong, J. D. Joannopoulos, and M. Soljacic (2009) "Observation of unidirectional backscattering-immune topological electromagnetic states," *Nature*, **461**, pp. 772–775.

[47] M., H., M. S., F. J., M. A., and T. M. (2013) "Imaging topological edge states in silicon photonics," *Nature Photonics*, **7**, pp. 1001–1005.

[48] Lu, L., J. D. Joannopoulos, and M. Solja?i? (2014), "Topological Photonics," e-print arXiv/1408.6730.

[49] Stanescu, T. D., V. Galitski, J. Y. Vaishnav, C. W. Clark, and S. Das Sarma (2009) "Topological insulators and metals in atomic optical lattices," *Phys. Rev. A*, **79**, p. 053639.

[50] Qi, X. L., Y. S. Wu, and S. C. Zhang (2006) "A general theorem relating the bulk topological number to edge states in two-dimensional insulators," *Phys. Rev. B*, **74**, p. 045125.

[51] Qi, X.-L., T. L. Hughes, and S.-C. Zhang (2010), "Chiral Topological Superconductor From the Quantum Hall State," e-print arXiv:1003.5448.

[52] Bernevig, B. A. and S. C. Zhang (2006) "Quantum spin Hall effect," *Phys. Rev. Lett.*, **96**, p. 106802.

[53] Roth, A., C. Brüne, H. Buhmann, L. W. Molenkamp, J. Maciejko, X.-L. Qi, and S.-C. Zhang (2009) "Nonlocal Transport in the Quantum Spin Hall State," *Science*, **325**, p. 294.

[54] Nowack, K. C., E. M. Spanton, M. Baenninger, M. KŽnig, J. R. Kirtley, B. Kalisky, C. Ames, P. Leubner, C. Brüne, H. Buhmann, L. W. Molenkamp, D. Goldhaber-Gordon, and K. A. Moler (2013) "Imaging currents in HgTe quantum wells in the quantum spin Hall regime," *Nature Mater.*, **12**, p. 787.

[55] Fu, L., C. L. Kane, and E. J. Mele (2007) "Topological insulators in three dimensions," *Phys. Rev. Lett.*, **98**, p. 106803.

[56] Hasan, M. Z. and C. L. Kane (2010) "Colloquium: Topological insulators," *Rev. Mod. Phys.*, **82**(4), pp. 3045–3067.

[57] Zhang, H., C.-X. Liu, X.-L. Qi, X. Dai, Z. Fang, and S.-C. Zhang (2009) "Topological insulators in Bi2Se3, Bi2Te3 and Sb2Te3 with a single Dirac cone on the surface," *Nature Phys.*, **5**, pp. 438–442.

[58] Xia, Y., L. Wray, D. Qian, D. Hsieh, A. Pal, H. Lin, A. Bansil, D. Grauer, Y. Hor, R. Cava, and M. Hasan (2009) "Observation of a large-gap topological-insulator class with a single Dirac cone on the surface," *Nature Phys.*, **5**, p. 398.

[59] Chang, C.-Z., J. Zhang, X. Feng, J. Shen, Z. Zhang, M. Guo, K. Li, Y. Ou, P. Wei, L.-L. Wang, et al. (2013) "Experimental Observation of the Quantum Anomalous Hall Effect in a Magnetic Topological Insulator," *Science*, **340**(6129), pp. 167–170.

[60] Liu, M., J. Zhang, C.-Z. Chang, Z. Zhang, X. Feng, K. Li, K. He, L.-l. Wang, X. Chen, X. Dai, Z. Fang, Q.-K. Xue, X. Ma, and Y. Wang (2012) "Crossover between Weak Antilocalization and Weak Localization in a Magnetically Doped Topological Insulator," *Phys. Rev. Lett.*, **108**, p. 036805.

[61] Wang, J., H. Li, C. Chang, K. He, J. Lee, H. Lu, Y. Sun, X. Ma, N. Samarth, S. Shen, Q. Xue, M. Xie, and M. Chan (2012) "Anomalous anisotropic magnetoresistance in topological insulator films," *Nano Research*, **5**(10), pp. 739–746.

[62] Yan, B. and S.-C. Zhang (2012) "Topological materials," *Reports on Progress in Physics*, **75**(9), p. 096501.

[63] Dai, X., T. L. Hughes, X.-L. Qi, Z. Fang, and S.-C. Zhang (2008) "Helical edge and surface states in HgTe quantum wells and bulk insulators," *Phys. Rev. B*, **77**, p. 125319.

[64] Fu, L. and C. L. Kane (2007) "Topological insulators with inversion symmetry," *Phys. Rev. B*, **76**, p. 045302.

[65] Virot, F. m. c., R. Hayn, M. Richter, and J. van den Brink (2011) "Metacinnabar (β-HgS): A Strong 3D Topological Insulator with Highly Anisotropic Surface States," *Phys. Rev. Lett.*, **106**(23), p. 236806.

[66] Zhang, W., R. Yu, W. Feng, Y. Yao, H. Weng, X. Dai, and Z. Fang (2011) "Topological Aspect and Quantum Magnetoresistance of $\beta - Ag2Te$," *Phys. Rev. Lett.*, **106**(15), p. 156808.

[67] Chadov, S., X. L. Qi, J. Kübler, G. H. Fecher, C. Felser, and S. C. Zhang (2010) "Tunable multifunctional topological insulators in ternary Heusler compounds," *Nature Mater.*, **9**, p. 541.

[68] Xiao, D., Y. Yao, W. Feng, J. Wen, W. Zhu, X.-Q. Chen, G. M. Stocks, and Z. Zhang (2010) "Half-Heusler Compounds as a New Class of Three-Dimensional Topological Insulators," *Phys. Rev. Lett.*, **105**, p. 096404.

[69] Moon, C.-Y. and S.-H. Wei (2006) "Band gap of Hg chalcogenides: Symmetry-reduction-induced band-gap opening of materials with inverted band structures," *Phys. Rev. B*, **74**(4), p. 045205.

[70] Feng, W., D. Xiao, J. Ding, and Y. Yao (2011) "Three-Dimensional Topological Insulators in $I - III - VI2$ and $II - IV - V2$ Chalcopyrite Semiconductors," *Phys. Rev. Lett.*, **106**(1), p. 016402.

[71] Wang, Y. J., H. Lin, T. Das, M. Z. Hasan, and A. Bansil (2011) "Topological insulators in the quaternary chalcogenide compounds and ternary famatinite compounds," *New J. Phys.*, **13**, p. 085017.

[72] Chen, S., X. G. Gong, C.-G. Duan, Z.-Q. Zhu, J.-H. Chu, A. Walsh, Y.-G. Yao, J. Ma, and S.-H. Wei (2011) "Band structure engineering of multinary chalcogenide topological insulators," *Phys. Rev. B*, **83**, p. 245202.

[73] Yan, B., L. Müchler, X.-L. Qi, S.-C. Zhang, and C. Felser (2012) "Topological insulators in filled skutterudites," *Phys. Rev. B*, **85**, p. 165125.

[74] Yan, B., C.-X. Liu, H. Zhang, C. Y. Yam, X. L. Qi, T. Frauenheim, and S. C. Zhang (2010) "Theoretical prediction of topological insulators in thallium-based III-V-VI2 ternary chalcogenides," *Europhys. Lett.*, **90**, p. 37002.

[75] Lin, H., R. S. Markiewicz, L. A. Wray, L. Fu, M. Z. Hasan, and A. Bansil (2010) "Single-Dirac-Cone Topological Surface States in the $TlBiSe_2$ Class of Topological Semiconductors," *Phys. Rev. Lett.*, **105**, p. 036404.

[76] Eremeev, S. V., Y. M. Koroteev, and E. V. Chulkov (2010) "Ternary thallium-based semimetal chalcogenides Tl-V-VI2 as a new class of three-dimensional topological insulators," *JETP Letters*, **91**, pp. 594–598.

[77] Sato, T., K. Segawa, H. Guo, K. Sugawara, S. Souma, T. Takahashi, and Y. Ando (2010) "Direct Evidence for the Dirac-Cone Topological Surface States in the Ternary Chalcogenide $TlBiSe_2$," *Phys. Rev. Lett.*, **105**, p. 136802.

[78] Kuroda, K., M. Ye, A. Kimura, S. V. Eremeev, E. E. Krasovskii, E. V. Chulkov, Y. Ueda, K. Miyamoto, T. Okuda, K. Shimada, H. Namatame, and M. Taniguchi (2010) "Experimental Realization of a Three-Dimensional Topological Insulator Phase in Ternary Chalcogenide $TlBiSe_2$," *Phys. Rev. Lett.*, **105**, p. 146801.

[79] Chen, Y. L., Z. K. Liu, J. G. Analytis, J.-H. Chu, H. J. Zhang, B. H. Yan, S.-K. Mo, R. G. Moore, D. H. Lu, I. R. Fisher, S. C. Zhang, Z. Hussain, and Z.-X. Shen (2010) "Single Dirac Cone Topological Surface State and Unusual Thermoelectric Property of Compounds from a New Topological Insulator Family," *Phys. Rev. Lett.*, **105**, p. 266401.

[80] Yan, B., H.-J. Zhang, C.-X. Liu, X.-L. Qi, T. Frauenheim, and S.-C. Zhang (2010) "Theoretical prediction of topological insulator in ternary rare earth chalcogenides," *Phys. Rev. B*, **82**, p. 161108.

[81] Jin, H., J.-H. Song, A. J. Freeman, and M. G. Kanatzidis (2011) "Candidates for topological insulators: Pb-based chalcogenide series," *Phys. Rev. B*, **83**, p. 041202.

[82] Kim, J., J. Kim, and S.-H. Jhi (2010) "Prediction of topological insulating behavior in crystalline Ge-Sb-Te," *Phys. Rev. B*, **82**, p. 201312.

[83] Xu, S.-Y., L. A. Wray, Y. Xia, R. Shankar, A. Petersen, A. Fedorov, H. Lin, A. Bansil, Y. S. Hor, D. Grauer, R. J. Cava, and M. Z. Hasan (2010), "Discovery of several large families of Topological Insulator classes with backscattering-suppressed spin-polarized single-Dirac-cone on the surface," e-print arXiv:1007.5111.

[84] Zhang, J., C.-Z. Chang, Z. Zhang, J. Wen, X. Feng, K. Li, M. Liu, K. He, L. Wang, X. Chen, Q.-K. Xue, X. Ma, and Y. Wang (2011) "Band structure engineering in $(Bi_{1-x}Sb_x)_2Te_3$ ternary topological insulators," *Nature Communications*, **2**, p. 574.

[85] Kong, D., Y. Chen, J. J. Cha, Q. Zhang, J. G. Analytis, K. Lai, Z. Liu, S. S. Hong, K. J. Koski, S.-K. Mo, Z. Hussain, I. R. Fisher, Z.-X. Shen, and Y. Cui (2011) "Ambipolar Field Effect in Topological Insulator Nanoplates of (BixSb1-x)2Te3," *Nature Nanotechnology*, **6**, pp. 705–709.

[86] Wray, L. A., S.-Y. Xu, Y. Xia, Y. S. Hor, D. Qian, A. V. Fedorov, H. Lin, A. Bansil, R. J. Cava, and M. Z. Hasan (2010) "Trajectory of the anomalous Hall effect towards the quantized state in a ferromagnetic topological insulator," *Nature Physics*, **6**, pp. 855–859.

[87] Hor, Y. S., A. J. Williams, J. G. Checkelsky, P. Roushan, J. Seo, Q. Xu, H. W. Zandbergen, A. Yazdani, N. P. Ong, and R. J. Cava (2010) "Superconductivity in $Cu_xBi_2Se_3$ and its Implications for Pairing in the Undoped Topological Insulator," *Phys. Rev. Lett.*, **104**(5), p. 057001.

[88] Hor, Y. S., J. G. Checkelsky, D. Qu, N. P. Ong, and R. J. Cava (2010), e-print arXiv:1006.0317.

[89] Zhang, J., S. Zhang, H. M. Weng, W. Zhang, L. Yang, Q. Liu, S. Feng, X. Wang, R. C. Yu, L. Z. Cao, L. Wang, W. Yang, H. Liu, W. Zhao, S. Zhang, X. Dai, Z. Fang, and C. Jin (2011) "Pressure-induced superconductivity in topological parent compound Bi2Te3," *Proc. Nat. Acad. Sci*, **108**, pp. 24–28.

[90] Liu, C.-X., T. L. Hughes, X.-L. Qi, K. Wang, and S.-C. Zhang (2008) "Quantum spin Hall effect in inverted type-II semiconductors," *Phys. Rev. Lett.*, **100**, p. 236601.

[91] Novik, E. G., A. Pfeuffer-Jeschke, T. Jungwirth, V. Latussek, C. R. Becker, G. Landwehr, H. Buhmann, and L. W. Molenkamp

(2005) "Band structure of semimagnetic $Hg_{1-y}Mn_yTe$ quantum wells," *Phys. Rev. B*, **72**, p. 035321.

[92] Furdyna, J. K. (1988) "Diluted magnetic semiconductors," *Journal of Applied Physics*, **64**(4), pp. R29–R64.

[93] Checkelsky, J. G., R. Yoshimi, A. Tsukazaki, K. S. Takahashi, Y. Kozuka, J. Falson, M. Kawasaki, and Y. Tokura (2014) "Trajectory of the anomalous Hall effect towards the quantized state in a ferromagnetic topological insulator," *Nature Physics*, **10**, pp. 731–736.

[94] Chang, C.-Z., W. Zhao, D. Y. Kim, H. Zhang, B. A. Assaf, D. Heiman, S.-C. Zhang, C. Liu, M. H. W. Chan, and J. S. Moodera (2015) "High-precision realization of robust quantum anomalous Hall state in a hard ferromagnetic topological insulator," *Nature Mater.*, **14**, pp. 473–477.

[95] Bestwick, A. J., E. J. Fox, X. Kou, L. Pan, K. L. Wang, and D. Goldhaber-Gordon (2015) "Precise Quantization of the Anomalous Hall Effect near Zero Magnetic Field," *Phys. Rev. Lett.*, **114**, p. 187201.

[96] Kou, X., L. Pan, J. Wang, Y. Fan, E. S. Choi, W.-L. Lee, T. Nie, K. Murata, Q. Shao, S.-C. Zhang, and K. L. Wang (2015), "Mapping the global phase diagram of quantum anomalous Hall effect," e-print arXiv/1503.04150.

[97] Roushan, P., J. Seo, C. V. Parker, Y. S. Hor, D. Hsieh, D. Qian, A. Richardella, M. Z. Hasan, R. J. Cava, and A. Yazdani (2009) "Topological surface states protected from backscattering by chiral spin texture," *Nature*, **460**, p. 1106.

[98] Zhang, T., P. Cheng, X. Chen, J.-F. Jia, X. Ma, K. He, L. Wang, H. Zhang, X. Dai, Z. Fang, X. Xie, and Q.-K. Xue (2009) "Experimental Demonstration of Topological Surface States Protected by Time-Reversal Symmetry," *Phys. Rev. Lett.*, **103**, p. 266803.

[99] Alpichshev, Z., J. G. Analytis, J. H. Chu, I. R. Fisher, and A. Kapitulnik (2010), e-print arXiv:1003.2233.

[100] Analytis, J. G., J. H. Chu, Y. L. Chen, F. Corredor, R. D. McDonald, Z. X. Shen, and I. R. Fisher (2010) "Bulk Fermi surface coexistence with Dirac surface state in Bi2Se3 : A comparison of photoemission and Shubnikov-de Haas measurements," *Phys. Rev. B*, **81**, p. 205407.

[101] Datta, S. (1997) *Electronic transport in mesoscopic systems*, Cambridge University Press, Cambridge UK; New York.

[102] Lewenkopf, C. H. and E. R. Mucciolo (2013) "The recursive Green's function method for graphene," *Journal of Computational Electronics*, **12**(2), pp. 203–231.

[103] Kane, C. L. and E. J. Mele (2005) "Z_2 topological order and the quantum spin Hall effect," *Phys. Rev. Lett.*, **95**, p. 146802.

[104] Xiu, F., L. He, Y. Wang, L. Cheng, L.-T. Chang, M. Lang, G. Huang, X. Kou, Y. Zhou, X. Jiang, Z. Chen, J. Zou, A. Shailos, and K. L. Wang (2011) "Manipulating surface states in topological insulator nanoribbons," *Nature Nanotechnology*, **6**, p. 216ÍC221.

[105] Zhang, D., J. Wang, A. M. DaSilva, J. S. Lee, H. R. Gutierrez, M. H. W. Chan, J. Jain, and N. Samarth (2011) "Superconducting proximity effect and possible evidence for Pearl vortices in a candidate topological insulator," *Phys. Rev. B*, **84**, p. 165120.

[106] Tian, M., W. Ning, Z. Qu, H. Du, J. Wang, and Y. Zhang (2013) "Dual evidence of surface Dirac states in thin cylindrical topological insulator Bi_2Te_3 nanowires," *Scientific Reports*, **3**, p. 1212.

[107] Rosenberg, G. and M. Franz (2010) "Witten effect in a crystalline topological insulator," *Phys. Rev. B*, **82**(3), p. 035105.

[108] Guo, H.-M., G. Rosenberg, G. Refael, and M. Franz (2010) "Topological Anderson Insulator in Three Dimensions," *Phys. Rev. Lett.*, **105**, p. 216601.

[109] Zhang, Y. and A. Vishwanath (2010) "Anomalous Aharonov-Bohm Conductance Oscillations from Topological Insulator Surface States," *Phys. Rev. Lett.*, **105**, p. 206601.

[110] Washburn, S., C. P. Umbach, R. B. Laibowitz, and R. A. Webb (1985) "Temperature dependence of the normal-metal Aharonov-Bohm effect," *Phys. Rev. B*, **32**, pp. 4789–4792.

[111] Aharonov, Y. and D. Bohm (1959) "Significance of Electromagnetic Potentials in the Quantum Theory," *Phys. Rev.*, **115**, pp. 485–491.

[112] Altshuler, B. L., A. G. Aronov, and B. Z. Spivak (1981) "The Aharonov-Bohm effect in disordered conductors," *JETP Lett.*, **33**, pp. 94–97.

[113] Bardarson, J. H., P. W. Brouwer, and J. E. Moore (2010) "Aharonov-Bohm Oscillations in Disordered Topological Insulator Nanowires," *Phys. Rev. Lett.*, **105**(15), p. 156803.

[114] Zhang, H.-J., X. Zhang, and S.-C. Zhang (2011), "Quantum Anomalous Hall Effect in Magnetic Topological Insulator GdBiTe3," e-print arXiv:1108.4857.

[115] Wu, C. (2008) "Orbital Analogue of the Quantum Anomalous Hall Effect in p-Band Systems," *Phys. Rev. Lett.*, **101**, p. 186807.

[116] Qiao, Z., S. A. Yang, W. Feng, W.-K. Tse, J. Ding, Y. Yao, J. Wang, and Q. Niu (2010) "Quantum anomalous Hall effect in graphene from Rashba and exchange effects," *Phys. Rev. B*, **82**, p. 161414.

[117] Hsu, H.-C., X. Liu, and C.-X. Liu (2013) "Reentrant quantum anomalous Hall effect with in-plane magnetic fields in HgMnTe quantum wells," *Phys. Rev. B*, **88**, p. 085315.

[118] Liu, X., H.-C. Hsu, and C.-X. Liu (2013) "In-Plane Magnetization-Induced Quantum Anomalous Hall Effect," *Phys. Rev. Lett.*, **111**, p. 086802.

[119] Beugeling, W., C. X. Liu, E. G. Novik, L. W. Molenkamp, and C. Morais Smith (2012) "Reentrant topological phases in Mn-doped HgTe quantum wells," *Phys. Rev. B*, **85**, p. 195304.

[120] Buttner, B., C. Liu, G. , Tkachov, E. Novik, C. Bruene, H. Buhmann, E. Hankiewicz, P. Recher, B. Trauzettel, S. Zhang, and L. Molenkamp (2011) "Single valley Dirac fermions in zero-gap HgTe quantum wells," *Nature Phys.*, **7**, pp. 418–422.

[121] Gui, Y., C. Becker, J. Liu, V. Daumer, V. Hock, H. Buhmann, and L. Molenkamp (2004) "Interplay of Rashba, Zeeman and Landau splitting in a magnetic two-dimensional electron gas," *Europhys. Lett.*, **65**(3), p. 393.

[122] Zverev, L., V. Kruzhaev, . E. R. G.M. Min'kov, N. Gavaleshko, and V. Frasunyak (1984) "Energy spectrum of the semimagnetic zero-gap semiconductor Hg1-xMnxTe in a magnetic field," *JETP*, **59**, p. 626.

[123] Peierles, R. (1933) "On the Theory of Diamagnetism of Conduction Electrons," *Z. Phys.*, **80**, p. 763.

[124] Fang, C., M. J. Gilbert, and B. A. Bernevig (2012) "Bulk topological invariants in noninteracting point group symmetric insulators," *Phys. Rev. B*, **86**, p. 115112.

[125] Dresselhaus, M. S., G. Dresselhaus, and A. Jorio (2008) *Group Theory: Application to the Physics of Condensed Matter*, Springer, Cambridge, MA.

[126] Beugeling, W., C. X. Liu, E. G. Novik, L. W. Molenkamp, and C. Morais Smith (2012) "Reentrant topological phases in Mn-doped HgTe quantum wells," *Phys. Rev. B*, **85**, p. 195304.

[127] Novik, E. G., A. Pfeuffer-Jeschke, T. Jungwirth, V. Latussek, C. R. Becker, G. Landwehr, H. Buhmann, and L. W. Molenkamp (2005) "Band structure of semimagnetic $Hg_{1-y}Mn_yTe$ quantum wells," *Phys. Rev. B*, **72**, p. 035321.

[128] Li, M., C. R. Becker, R. Gall, W. Faschinger, and G. Landwehr (1997) "X-ray reciprocal space mapping of a (112) oriented HgTe/Hg0.1Cd0.9Te superlattice," *Applied Physics Letters*, **71**(13), pp. 1822–1824.

[129] Hatch, S., R. Sewell, J. Dell, L. Faraone, C. Becker, and B. Usher (2006) "Investigation of HgTe-HgCdTe superlattices by high-resolution X-ray diffraction," *Journal of Electronic Materials*, **35**(6), pp. 1481–1486.

[130] Li, M., R. Gall, C. R. Becker, T. Gerhard, W. Faschinger, and G. Landwehr (1997) "Strains in HgTe/Hg0.1Cd0.9Te superlattices grown on (211)B Cd0.96Zn0.04Te substrates," *Journal of Applied Physics*, **82**(10), pp. 4860–4864.

[131] Niu, Q., D. J. Thouless, and Y.-S. Wu (1985) "Quantized Hall conductance as a topological invariant," *Phys. Rev. B*, **31**, p. 3372.

[132] Li, J., R.-L. Chu, J. K. Jain, and S.-Q. Shen (2009) "Topological Anderson Insulator," *Phys. Rev. Lett.*, **102**, p. 136806.

[133] Groth, C. W., M. Wimmer, A. R. Akhmerov, J. Tworzydło, and C. W. J. Beenakker (2009) "Theory of the Topological Anderson Insulator," *Phys. Rev. Lett.*, **103**, p. 196805.

[134] Ostrovsky, P. M., I. V. Gornyi, and A. D. Mirlin (2010) "Interaction-Induced Criticality in $\mathbb{Z}_2$ Topological Insulators," *Phys. Rev. Lett.*, **105**, p. 036803.

[135] Shen, S.-Q. (2012) *Topological Insulators*, Springer.

[136] Winkler, R. (2003) *Spin-Orbit Coupling Effects in Two-Dimensional Electron and Hole Systems*, Springer.

[137] Yang, K. and R. N. Bhatt (1996) "Floating of Extended States and Localization Transition in a Weak Magnetic Field," *Phys. Rev. Lett.*, **76**, pp. 1316–1319.

[138] Onoda, M. and N. Nagaosa (2003) "Quantized Anomalous Hall Effect in Two-Dimensional Ferromagnets: Quantum Hall Effect in Metals," *Phys. Rev. Lett.*, **90**(20), p. 206601.

[139] Huo, Y. and R. N. Bhatt (1992) "Current carrying states in the lowest Landau level," *Phys. Rev. Lett.*, **68**, pp. 1375–1378.

Vita

Hsiu-Chuan Hsu

Education

- **The Pennsylvania State University**, University Park, Pennsylvania, USA
  Ph.D. in Physics, Expected December 2015
  Thesis topic : ' Theoretical Study on Transport Properties of Topological States of Matter'
  Advisor : Professor Chao-Xing Liu

- **National Taiwan University**, Taipei, Taiwan
  M.S. in Physics, August 2008
  Thesis Topic : 'Effects of Disorder on Spin Hall Conductivity in Two-Dimensional Electron Systems'
  Advisor : Professor Guang-Yu Guo

- **National Tsing-Hua University**, Hsinchu, Taiwan
  B.S. in Physics, June 2006

Publications

- X. Liu, Hsiu-Chuan Hsu and C. X. Liu, Phys. Rev. Lett. 111, 086802 (2013).
- Hsiu-Chuan Hsu, X. Liu, and C.-X. Liu, Phys. Rev. B 88, 085315 (2013).
- T.-W. Chen, Hsiu-Chuan Hsu and G. Y. Guo, Phys. Rev. B 80, 165302 (2009).

Award

- Travel award, Forum of Graduate Student Association, American Physics Society, January 2014